

Artificial intelligence-based solution for bioluminescence tomography reconstruction for glioblastoma multiforme

Citation for published version (APA):

Rezaeifar, B. (2024). *Artificial intelligence-based solution for bioluminescence tomography reconstruction for glioblastoma multiforme*. [Doctoral Thesis, Maastricht University, Hasselt University]. Maastricht University. <https://doi.org/10.26481/dis.20240123br>

Document status and date:

Published: 01/01/2024

DOI:

[10.26481/dis.20240123br](https://doi.org/10.26481/dis.20240123br)

Document Version:

Publisher's PDF, also known as Version of record

Please check the document version of this publication:

- A submitted manuscript is the version of the article upon submission and before peer-review. There can be important differences between the submitted version and the official published version of record. People interested in the research are advised to contact the author for the final version of the publication, or visit the DOI to the publisher's website.
- The final author version and the galley proof are versions of the publication after peer review.
- The final published version features the final layout of the paper including the volume, issue and page numbers.

[Link to publication](#)

General rights

Copyright and moral rights for the publications made accessible in the public portal are retained by the authors and/or other copyright owners and it is a condition of accessing publications that users recognise and abide by the legal requirements associated with these rights.

- Users may download and print one copy of any publication from the public portal for the purpose of private study or research.
- You may not further distribute the material or use it for any profit-making activity or commercial gain
- You may freely distribute the URL identifying the publication in the public portal.

If the publication is distributed under the terms of Article 25fa of the Dutch Copyright Act, indicated by the "Taverne" license above, please follow below link for the End User Agreement:

www.umlib.nl/taverne-license

Take down policy

If you believe that this document breaches copyright please contact us at:

repository@maastrichtuniversity.nl

providing details and we will investigate your claim.

**Artificial Intelligence-Based Solution for
Bioluminescence Tomography Reconstruction for
Glioblastoma Multiforme**

Behzad Rezaeifar



UHASSELT

KNOWLEDGE IN ACTION



Maastricht University

Doctoral dissertation submitted to obtain the degrees of
- Doctor of Engineering Technology | UHasselt
- Doctor | Maastricht University

Behzad Rezaeifar

DOCTORAL DISSERTATION

Artificial Intelligence-Based
Solution for Bioluminescence
Tomography Reconstruction for
Glioblastoma Multiforme

Promoters:

Prof. Dr Brigitte Reniers | UHasselt
Prof. Dr ir. Frank Verhaegen | Maastricht University
Dr Ludwig Dubois | Maastricht University

D/2023/2451/85

Artificial Intelligence-Based Solution for Bioluminescence Tomography Reconstruction for Glioblastoma Multiforme

DISSERTATION

to obtain the degree of Doctor at Maastricht University,
on the authority of the Rector Magnificus, Prof. dr. Pamela Habibović
and the degree of Doctor of Engineering Technology at Hasselt University
on the authority of the Rector Magnificus, Prof. dr. Bernard Vanheusden,
in accordance with the decision of the Board of Deans,
to be defended in public on Tuesday 23 January 2024, at 13:00 hours

by

Behzad Rezaeifar

Promotors:

Prof.dr.ir F.J.W. Verhaegen, Maastricht University

Dr. L.J. Dubois, Maastricht University

Prof. dr. B. Reniers, Hasselt University

Assessment Committee:

Prof.dr. M.A.G.G. Vooijs (Chair), Maastricht University

Prof. dr. G.J. Bex, Hasselt University

Prof.dr.ir. W. Steenbergen, Twente University

Prof.dr. R.A. Weersink, University of Toronto

Table of Contents

	Page
Chapter 1 Introduction	1
Chapter 2 Use of a Luciferase-Expressing Orthotopic Rat Brain Tumor Model to Optimize a Targeted Irradiation Strategy for Efficacy Testing with Temozolomide	11
Chapter 3 A Deep Learning and Monte Carlo based Framework for Bioluminescence Imaging Center of Mass-Guided Glioblastoma Targeting	29
Chapter 4 A Deep-Learning Assisted Bioluminescence Tomography Method to Enable Radiation Targeting in Rat Glioblastoma	57
Chapter 5 Evaluating Deep-Learning Assisted Bioluminescence Tomography: A Monte Carlo Study	97
Chapter 6 Improving AI-Assisted Tumor Segmentation in Pre-clinical Glioblastoma Rat Models Using Complementary Information from Contrast-Enhanced CT and Bioluminescence Imaging	117
Chapter 7 Design and Manufacturing of Tissue-Mimicking Optical Phantoms for Bioluminescence Imaging of the glioblastoma Rat Models: A Pilot Study	135
Chapter 8 Discussion and Future Perspectives	151
Appendices Summary	164
Samenvatting	170
A Reflection on Scientific and Social Impacts	172
Curriculum Vitae & List of publications	173
Acknowledgments	175

Table of Abbreviations

AHD	Average Hausdorff Distance
AI	Artificial Intelligence
bGTV	BLI-based GTV
BLI	Bioluminescence Imaging
BLT	Bioluminescence Tomography
bPTV	BLI-based PTV
BSF	Bioluminescence Skin Fluence
CBCT	Cone-Beam Computed Tomography
CE-CT	Contrast-Enhanced Computed Tomography
cGTV	CT-based GTV
CNN	Convolutional Neural Network
CoM	Center of Mass
CT	Computed Tomography
DL	Deep Learning
DSC	Dice Similarity Coefficient
DVH	Dose-Volume Histogram
DVM	Dose Volume Metrics
FN	False Negative
FP	False Positive
GAN	Generative Adversarial Network
GATE	Geant4 Application for Tomographic Emission
GBM	Glioblastoma Multiforme
GPU	Graphics Processing Unit
GTV	Gross Tumor Volume
H&E	hematoxylin and eosin
HU	Hounsfield Units
IoU	Intersect over Union
IR	Infrared
MCS	Monte Carlo Simulation
MLP	Multi-Layered Perceptron
MRI	Magnetic Resonance Imaging
MSE	Mean Squared Error

OAR	Organs at Risk
OOD	Out Of Distribution
PET	Positron Emission Tomography
PTV	Planning Target Volume
RT	Radiotherapy
RTE	Radiative Transport Equation
SD	Standard Deviation
SOC	Standard of Care
TMZ	Temozolomide
TP	True Positive
UV	Ultraviolet

Chapter 1

Introduction

Clinical Radiotherapy

Despite the recent advances in public healthcare, cancer remains one of the main factors in morbidity and mortality^[1]. Cancer treatment varies based on not only the type of cancer but also its stage at the time of diagnosis^[2]. Nevertheless, the major treatment modalities are surgery, radiation, and systematic therapies^[3]. Radiation therapy, commonly referred to as radiotherapy, encompasses a range of cancer treatments utilizing ionizing radiation with the aim of inducing an anti-tumor response. Nearly half of cancer patients receive radiotherapy treatment at least once in the course of their treatment^[4]. This form of therapy can be further categorized into internal radiation therapy, i.e. brachytherapy, where a radiation source is positioned within the body in close proximity to malignant cells, and external beam radiotherapy, which employs an external apparatus to generate and administer the radiation beam to the patient^[5]. Throughout the course of this thesis, the term “radiotherapy” exclusively pertains to external beam radiotherapy. The general clinical workflow for patients receiving radiotherapy includes various steps depicted in Figure 1.1a. Following a diagnosis, it is usually required to obtain a computer tomography (CT) scan to acquire anatomical information about the tumor and organs at risk. Thereafter, a medical specialist carefully investigates the obtained images to distinguish healthy tissue from malignant tumors and provide a detailed treatment plan. The main goal of the treatment plan is to target and eliminate all the tumor cells while preserving maximal healthy tissue. Once the optimized treatment plan is ready, the patient will be called back to receive the prescribed radiation dose, often in the form of several treatment fractions, adding up to the total therapy dose.

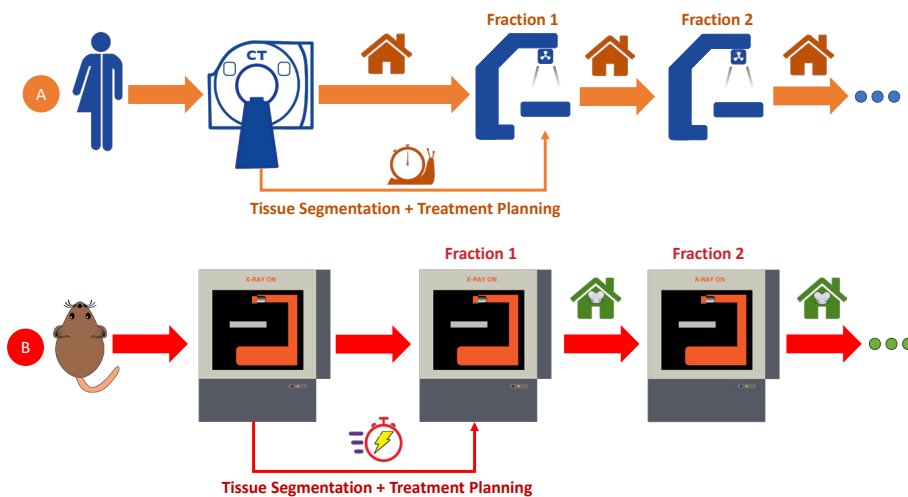


Figure 1.1 – Radiotherapy workflow in (A) clinical and (B) pre-clinical practice

Pre-clinical Radiotherapy

Most of the progress achieved in clinical radiotherapy originates from technological breakthroughs within the last century, often lacking substantial supporting evidence from comprehensive pre-clinical investigations involving animal models^[6]. Consequently, a range of radiobiological and physics studies becomes essential, serving not only to authenticate prevailing patterns in clinical radiotherapy but also to propel our comprehension of diverse hypotheses within the realm of cancer radiotherapy. As a result, the domain of pre-clinical radiotherapy plays a significant and increasing role in assessing emerging trends like FLASH radiotherapy^[7] and the augmentation of fundamental insights, particularly aimed at enhancing the effectiveness of cancer treatment outcomes.

Historically, radiobiological experiments were performed using clinical radiotherapy setups, resulting in imprecise radiation administration that bore no resemblance to the actual clinical scenario^{[6], [8]}. The gap between the clinical workflow and the required pre-clinical experimental setup was eventually addressed in 2007 by developing small-animal precision radiotherapy platforms. The emergence of small-animal imaging and irradiation platforms empowered many cancer biology and physics studies in the past two decades^[9]. Nowadays, the conventional pre-clinical workflow closely mirrors the clinical counterpart, as illustrated in Figure 1.1b. Presently, two commercially accessible platforms for small-animal irradiation platforms exist: SARRP (Xstrahl Life Sciences, Suwanee, GA, USA) and SMART+ (Precision X-ray Inc., Madison, CT, USA). The key distinction between these systems lies in the SMART+ platform's rotating gantry, which differs from the rotating bed in the SARRP system. Therefore, the imaging beam passes through the anterior-posterior (head-tail) direction in SARRP, while the SMART+ system's imaging beam is directed in the dorsal-ventral orientation, passing through less tissue. CT scan is commonly regarded as the preferred imaging method for most pre-clinical investigations into cancer due to its ability to provide both anatomical structures and the electron density data necessary for calculating the radiation dose during the planning of radiation treatments^[10]. However, given the diminutive size of the subjects being imaged, namely small rodents, a heightened level of spatial resolution is imperative. Consequently, the imaging modalities employed in these systems can perform micro Cone-Beam CT (CBCT) scans with voxel sizes smaller than 0.001 mm^3 . This refinement often entails an increased X-ray irradiation dose administered to the animals during imaging, a factor of significance, particularly in longitudinal studies^{[11], [12]}. Workman et al. underscored the importance of managing imaging doses, suggesting that the cumulative dose should remain below 1 Gy to avoid overdosing healthy tissue with X-ray radiation and avert potential therapeutic impact on the tumor^[13].

Bioluminescence Imaging

Figure 1.2 provides an overview of the available imaging modalities for guiding small animal radiotherapy through imaging. Among different functional imaging modalities, optical imaging emerges as a notable choice due to its capacity to provide high-resolution visualizations while maintaining economical operational considerations. Operating within the optical spectrum, including not only the visible light range but also the ultraviolet (UV) and infrared (IR) spectrum, this approach enables the acquisition of tissue imagery without any X-ray imaging radiation impact on the subject. Notably, Bioluminescence Imaging (BLI), a 2D planar optical imaging modality, capitalizes on luminescent emissions originating from genetically modified tumor cells. Figure 1.3 summarizes the workflow required for acquiring a BLI.

In BLI, tumor cells are genetically modified to express luciferase, an enzyme cloned from firefly. Once the genetically modified tumor cells are implanted into the rodent, they can be activated by a specific substrate called luciferin. Consequently, only the implanted genetically modified tumor cells will emit light shortly after luciferin injection. Hence, BLI constitutes a cheap alternative form of functional imaging characterized by its absence of background noise since the only light source within a totally dark, light-tight imaging cabinet is the genetically modified tumor cells. However, a combination of the genetic modifications performed on the tumor and the injection of firefly-originated luciferin substrate prevent any clinical application for BLI. Nevertheless, BLI started gaining the attention of researchers in pre-clinical cancer research, with the first successful firefly luciferase cloning in 1985^{[14], [15]}, increased to more than

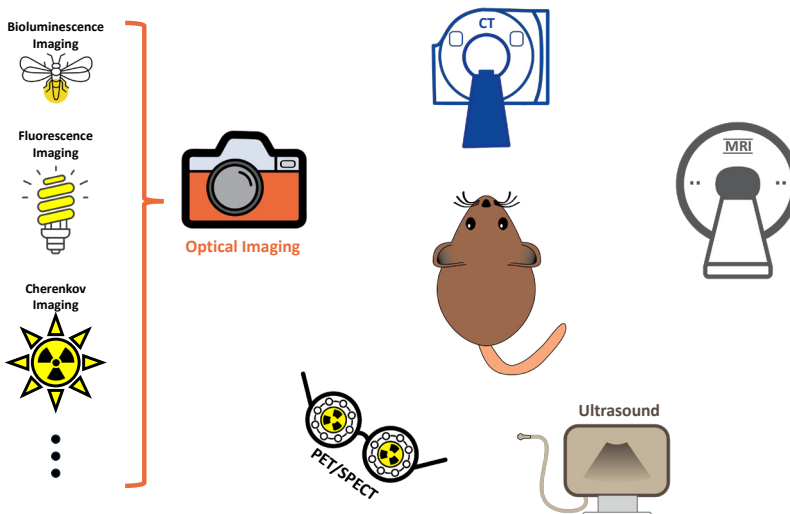


Figure 1.2 – Overview of the small-animal image-guidance modalities in pre-clinical cancer research

120 BLI-related papers per year published from 2016-2018 underlining different BLI applications in cancer research^[16].

Due to the lack of background noise, BLI can facilitate tumor growth monitoring in-vivo without any radiation burden on the animal. However, the 2D information obtained from BLI does not include accurate spatial information about tumor location. As shown in Figure 1.3, 2D BLI includes a diffused signal without any volumetric information about the tumor, such as shape, depth, and 3D location. Thus, BLI cannot enable accurate tumor radiation targeting in 3D with comprehensive radiation delivery systems available. As a result, the practical utility of BLI in pre-clinical cancer investigations can be fully exploited by reconstructing 3D Bioluminescence Tomography (BLT), an imaging modality that leverages data acquired from 2D BLI at varying angles to reconstruct the spatial distribution of the light source, herein referred to interchangeably as the tumor or radiation target.

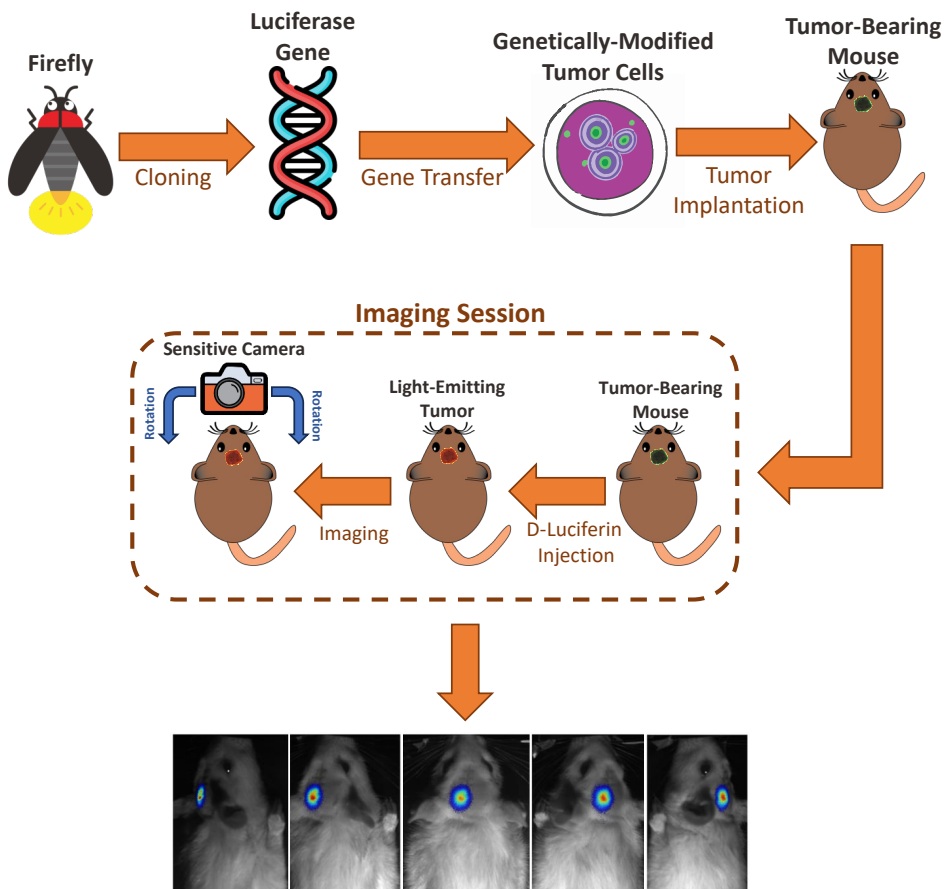


Figure 1.3 – General Workflow in Bioluminescence Imaging (BLI)

Bioluminescence Tomography

In order to reconstruct the 3D BLT from BLI projections from different angles, an accurate model of light propagation is essential to estimate the Bioluminescence images from any arbitrary source. The Radiative Transport Equation (RTE) and its approximations are the most popular forward models used in the literature^{[17]-[20]}. Upon establishing the forward model governing light propagation, an iterative optimization problem can be constructed, thereby solving the inverse problem, i.e., the BLT reconstruction problem. In other words, as illustrated in Figure 1.4, in each iteration, an estimation of the light source is made, and the resulting BLI projections are computed based on the forward model. The final solution is a specific light source that minimizes the error between the measured and calculated BLI.

However, the aforementioned solution to the BLT reconstruction problem is highly ill-posed. Hence, there is no unique answer for the reconstruction problem, and often, prior information together with a regularization term is required to reduce the ill-posedness and assist the solution. Artificial Intelligence (AI), on the other hand, proved to be a useful tool in solving

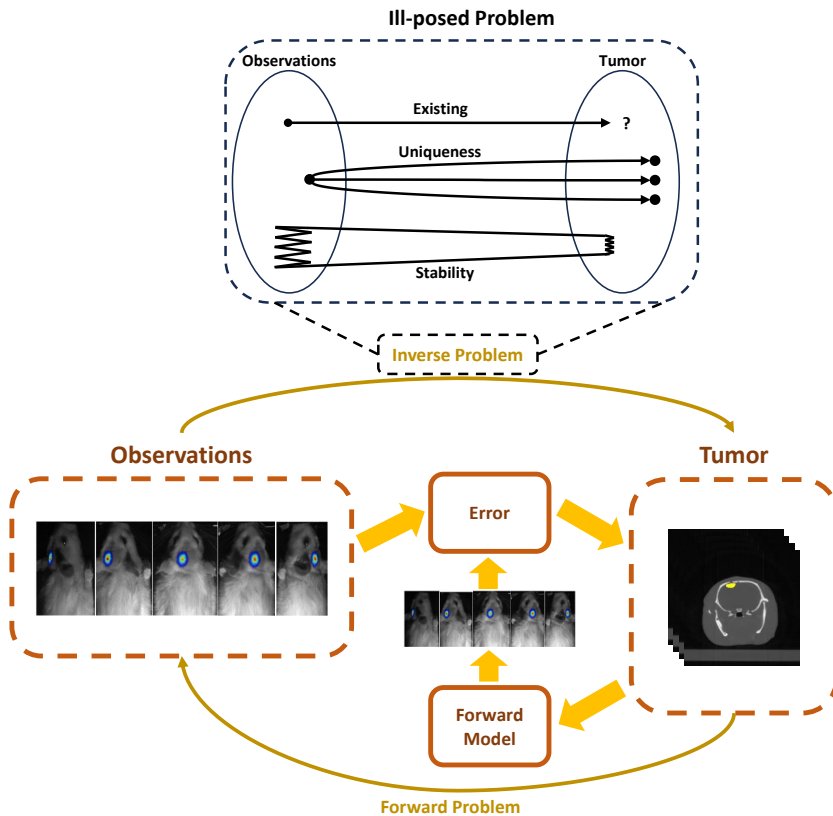


Figure 1.4 – Conventional solution for the BLT reconstruction problem

ill-posed problems in other applications. Therefore, this thesis introduces an AI-based approach toward the 3D BLT reconstruction problem and distances from the more conventional model-driven methods.

The methods proposed in this thesis employ the Bioluminescence Skin Fluence (BSF) as the primary input for the AI models. This choice is rooted in the convenience of obtaining BSF directly from the 2D BLI images through a process of back-projection onto the surface of the CT scan. Alternatively, BSF can also be effectively simulated within the Monte Carlo Simulation (MCS) environment, obviating the need for computationally expensive photon transport calculations in the open space between the animal's surface and the camera detector. This strategic utilization of BSF establishes an intermediary state between the MCS simulations and empirical BLI measurements, thereby facilitating the creation of a realistic MCS training database.

Bioluminescence-Based Treatment Planning

Once the 3D BLT is obtained, it can be utilized to target the tumor with radiation and monitor its response to radiotherapy. Employing BLT for tracking tumor evolution and guiding targeting strategies not only serves to mitigate the cumulative X-ray imaging exposure inflicted upon the small animal, a particularly relevant consideration in longitudinal investigations. In addition, it facilitates replacing other ionizing functional imaging modalities and thus alleviates the demands associated with radiation protection measures. Figure 1.5 represents a BLI-based radiotherapy workflow. For BLI-based treatment planning to work, it is often required to obtain the 3D spatial information by obtaining a CT scan. However, since only an approximation of the animal's outer boundary is needed at this stage, a much lower-resolution low-dose CT scan can be enough.

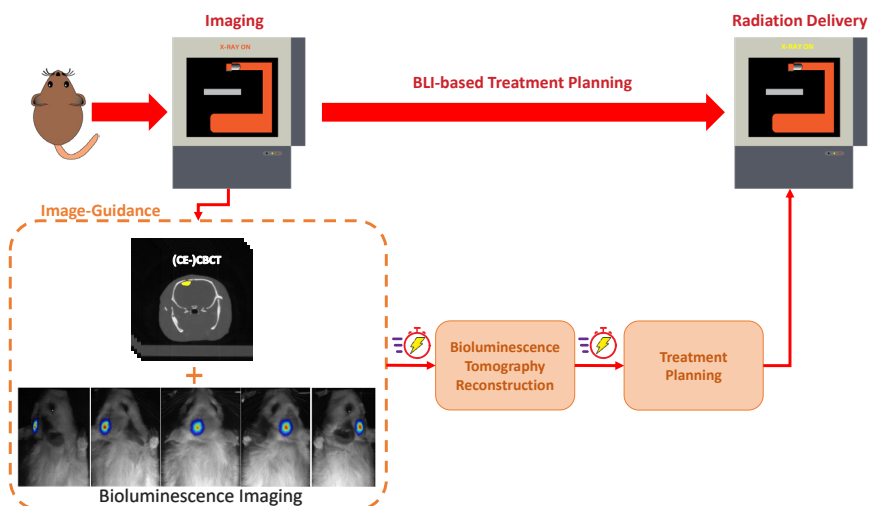


Figure 1.5 – BLI-based radiotherapy workflow.

Alternatively, a high-resolution high-dose CT can be obtained before the tumor implantation and used for registration reference to a very low-resolution CT, such as scout CT scans, acquired at each radiation delivery session. Consequently, the X-ray imaging radiation burden on the animals is reduced greatly by adapting the BLI-based treatment planning.

Objectives and Outline of the Thesis

The principal objective of this thesis involves an in-depth exploration aimed at refining the quality of BLT reconstruction, with a parallel emphasis on its application in advancing pre-clinical radiotherapeutic interventions. While the primary focus is on glioblastoma multiforme (GBM) as the main malignancy type in this thesis, the developed methodologies can be adapted to various other applications with minimal modifications. To accomplish this overarching goal, the thesis first introduces the current state-of-the-art BLI application in GBM pre-clinical research in Chapter 2. This section portrays a representative illustration of 2D BLI integration within the conventional pre-clinical GBM workflow, which is primarily limited to the surveillance of tumor progression. Subsequent chapters, spanning from Chapter 3 to Chapter 6, focus on the development of various novel AI-based approaches geared towards enhancing the efficacy of BLI-based treatment planning for GBM. Consequently, Chapter 7 addresses the manufacturing methods for obtaining tissue-mimicking optical phantoms to not only standardize and calibrate the measurement workflow but also to spare animals as much as possible. Finally, the last chapter includes a thorough discussion about this subject, including the limitations of the proposed methods and ways to improve it further.

References

- [1] J. Ferlay et al., "Cancer statistics for the year 2020: An overview," *Int. J. Cancer*, Apr. 2021, doi: 10.1002/ijc.33588.
- [2] B. Oronsky, T. R. Reid, A. Oronsky, N. Sandhu, and S. J. Knox, "A Review of Newly Diagnosed Glioblastoma," *Front. Oncol.*, vol. 10, p. 574012, Feb. 2021, doi: 10.3389/fonc.2020.574012.
- [3] E. Bidram et al., "A concise review on cancer treatment methods and delivery systems," *J. Drug Deliv. Sci. Technol.*, vol. 54, p. 101350, Dec. 2019, doi: 10.1016/j.jddst.2019.101350.
- [4] G. Chaput and L. Regnier, "Radiotherapy," *Can. Fam. Physician*, vol. 67, no. 10, pp. 753–757, Oct. 2021, doi: 10.46747/cfp.6710753.
- [5] X. Wang, M. Chen, R. Wei, and Z. Wang, "External Radiation versus Internal Radiation for Patients with Advanced Unresectable HCC -A SEER Based Study," *J. Cancer*, vol. 10, no. 5, pp. 1171–1180, Jan. 2019, doi: 10.7150/jca.28983.
- [6] F. Verhaegen, P. Granton, and E. Tryggestad, "Small animal radiotherapy research platforms," *Phys. Med. Biol.*, vol. 56, no. 12, pp. R55-83, Jun. 2011, doi: 10.1088/0031-9155/56/12/R01.
- [7] A. Borghini, C. Vecoli, L. Labate, D. Panetta, M. G. Andreassi, and L. A. Gizzi, "FLASH ultra-high dose rates in radiotherapy: preclinical and radiobiological evidence," *Int. J. Radiat. Biol.*, vol. 98, no. 2, pp. 127–135, 2022, doi: 10.1080/09553002.2022.2009143.
- [8] M. Ghita, K. H. Brown, O. J. Kelada, E. E. Graves, and K. T. Butterworth, "Integrating Small Animal Irradiators with Functional Imaging for Advanced Preclinical Radiotherapy Research," *Cancers*, vol. 11, no. 2, Art. no. 2, Feb. 2019, doi: 10.3390/cancers11020170.
- [9] K. H. Brown et al., "A scoping review of small animal image-guided radiotherapy research: Advances, impact and future opportunities in translational radiobiology," *Clin. Transl. Radiat. Oncol.*, vol. 34, pp. 112–119, May 2022, doi: 10.1016/j.ctro.2022.04.004.
- [10] F. Verhaegen, S. van Hoof, P. V. Granton, and D. Trani, "A review of treatment planning for precision image-guided photon beam pre-clinical animal radiation studies," *Z. Med. Phys.*, vol. 24, no. 4, pp. 323–334, Dec. 2014, doi: 10.1016/j.zemedi.2014.02.004.
- [11] F. Verhaegen et al., "ESTRO ACROP: Technology for precision small animal radiotherapy research: Optimal use and challenges," *Radiother. Oncol.*, vol. 126, no. 3, pp. 471–478, Mar. 2018, doi: 10.1016/j.radonc.2017.11.016.
- [12] A. Vaniqui, L. E. J. R. Schyns, I. P. Almeida, B. van der Heyden, S. J. van Hoof, and F. Verhaegen, "The impact of dual energy CT imaging on dose calculations for pre-clinical studies," *Radiat. Oncol.*, vol. 12, no. 1, p. 181, Nov. 2017, doi: 10.1186/s13014-017-0922-9.
- [13] P. Workman et al., "Guidelines for the welfare and use of animals in cancer research," *Br. J. Cancer*, vol. 102, no. 11, Art. no. 11, May 2010, doi: 10.1038/sj.bjc.6605642.
- [14] J. R. de Wet, K. V. Wood, D. R. Helinski, and M. DeLuca, "Cloning of firefly luciferase cDNA and the expression of active luciferase in *Escherichia coli*," *Proc. Natl. Acad. Sci. U. S. A.*, vol. 82, no. 23, pp. 7870–7873, Dec. 1985, doi: 10.1073/pnas.82.23.7870.
- [15] R. T. Sadikot and T. S. Blackwell, "Bioluminescence Imaging," *Proc.*

Chapter 1

- Am. Thorac. Soc., vol. 2, no. 6, pp. 537–540, Dec. 2005, doi: 10.1513/pats.200507-067DS.
- [16] N. Alsawaftah, A. Farooq, S. Dhou, and A. F. Majdalawieh, "Bioluminescence Imaging Applications in Cancer: A Comprehensive Review," *IEEE Rev. Biomed. Eng.*, vol. 14, pp. 307–326, 2021, doi: 10.1109/RBME.2020.2995124.
- [17] J. Feng, K. Jia, Z. Li, B. Pogue, M. Yang, and Y. Wang, "Bayesian sparse-based reconstruction in bioluminescence tomography improves localization accuracy and reduces computational time.," *J. Biophotonics*, 2018, doi: 10.1002/jbio.201700214.
- [18] H. Dehghani, J. A. Guggenheim, S. L. Taylor, X. Xu, and K. K.-H. Wang, "Quantitative bioluminescence tomography using spectral derivative data," *Biomed. Opt. Express*, vol. 9, no. 9, pp. 4163–4174, Aug. 2018, doi: 10.1364/BOE.9.004163.
- [19] Z. Deng et al., "In vivo Bioluminescence Tomography Center of Mass-Guided Conformal Irradiation," *Int. J. Radiat. Oncol. Biol. Phys.*, vol. 106, no. 3, pp. 612–620, Mar. 2020, doi: 10.1016/j.ijrobp.2019.11.003.
- [20] A. Bentley, J. Rowe, and H. Dehghani, "Simultaneous diffuse optical and bioluminescence tomography to account for signal attenuation to improve source localization," *Biomed. Opt. Express*, 2020, doi: 10.1364/BOE.401671.

Chapter 2

Use of a Luciferase-Expressing Orthotopic Rat Brain Tumor Model to Optimize a Targeted Irradiation Strategy for Efficacy Testing with Temozolomide

Authors

Alexandra M. Mowday, Natasja G. Lieuwes, Rianne Biemans, Damiënne Marcus, **Behzad Rezaeifar**, Brigitte Reniers, Frank Verhaegen, Jan Theys and Ludwig J. Dubois

Adopted From

Cancers (Basel). 2020 Jun 15;12(6):1585. doi: 10.3390/cancers12061585

Abstract

Glioblastoma multiforme (GBM) is a common and aggressive malignant brain cancer with a mean survival time of approximately 15 months after initial diagnosis. Currently, the standard-of-care (SOC) treatment for this disease consists of radiotherapy (RT) with concomitant and adjuvant temozolomide (TMZ). We sought to develop an orthotopic pre-clinical model of GBM and to optimize a protocol for non-invasive monitoring of tumor growth, allowing for determination of the efficacy of SOC therapy using a targeted RT strategy combined with TMZ. A strong correlation ($r = 0.80$) was observed between contrast-enhanced (CE)-CT-based volume quantification and bioluminescent (BLI)-integrated image intensity when monitoring tumor growth, allowing for BLI imaging as a substitute for CE-CT. An optimized parallel-opposed single-angle RT beam plan delivered on average 96% of the expected RT dose (20, 30 or 60 Gy) to the tumor. Normal tissue on the ipsilateral and contralateral sides of the brain were spared 84% and 99% of the expected dose, respectively. An increase in median survival time was demonstrated for all SOC regimens compared to untreated controls (average 5.2 days, $p < 0.05$), but treatment was not curative, suggesting the need for novel treatment options to increase therapeutic efficacy.

1. Introduction

Glioblastoma multiforme (GBM) is an aggressive and frequently occurring primary malignant brain cancer with a mean survival time of less than 15 months after initial diagnosis, regardless of treatment [1]. Despite recent advancement in the understanding of the molecular pathogenesis behind the disease and improvement in diagnostic ability, little has changed in terms of prognosis. GBM remains a lethal disease, and most patients (>70%) will die within two years^[1,2]. Standard-of-care therapy for newly diagnosed GBM consists of surgical resection, if feasible, and/or regional radiotherapy (RT) with concomitant or adjuvant temozolomide (TMZ), which provides an improvement in median survival of only 2.5 months^[1]. Bevacizumab is approved for patients with recurrent GBM, but only prolongs progression-free survival with no impact on overall survival^[3].

Until recently, large-field single-beam irradiation was commonplace in pre-clinical animal studies^[4,5]. Radiation dose was crudely estimated and efficacy studies were often hampered by high doses of radiation to healthy tissue. Therefore, tumors were often implanted subcutaneously to enable relatively easy targeting with a single beam and some shielding. Yet subcutaneous glioma models lack the appropriate central nervous system microenvironment and are poorly predictive of therapeutic outcome, particularly for anti-angiogenic drugs or metabolic inhibitors^[6]. Orthotopically implanted gliomas in syngeneic, immunocompetent animals are thought to provide the most accurate representation of the biological features of cancer growth and metastasis in humans^[7]. Modern techniques now permit closer replication of clinical practice when irradiating orthotopic models, and recently developed treatment planning systems allow for better protection of healthy tissue from the radiation dose^[4,5,8,9].

The histopathological characteristics of human GBM include areas of intratumoral hypoxia and necrosis^[10], in addition to a diffuse growth infiltrate into the neuropil^[11]. Yet, frequently used pre-clinical GBM models (e.g., C6, 9L, and U87) are generally immunogenic to the host, contain minimal hypoxia, and tumor growth is sharply delineated with little infiltration into normal brain tissue^[12-14]. In experimental neurooncology, there is thus a strong need for clinically relevant pre-clinical models that are reproducible and physiologically applicable to the human condition. The F98 rat glioma cell line was originally obtained following administration of ethylnitrosourea to pregnant rats, whose progeny developed brain tumors^[15]. Similar to the features of human GBM, these gliomas have an infiltrative pattern of growth, are weakly immunogenic, express relevant cellular markers and have areas of tumor hypoxia with a necrotic core^[12,16-18], making them a strong candidate for use as an orthotopic GBM model.

The aim of this study was to use the F98 orthotopic rat glioma model to optimize a targeted RT strategy for GBM in a manner which is similar to clinical practice. Development of a RT beam protocol that maximally spared the radiation dose to healthy tissues then allowed for accurate determination of the efficacy of SOC therapy in this model for the first time.

2. Results

2.1. Orthotopic F98 GBM Tumors Can Be Monitored Non-Invasively by BLI and CE-CT

In order to monitor tumor growth and treatment efficacy non-invasively, F98 glioma cells were engineered to overexpress firefly luciferase, permitting bioluminescent imaging (BLI) of tumor cells^[19]. To allow longitudinal treatment monitoring without cumulative radiation dose, we investigated whether BLI-based signal intensity could substitute for CE-CT-based tumor volume assessment. BLI signal was observed and localized to the tumor site and CE-CT confirmed that BLI signal was related to tumor growth (Figure S1A,B). Both increased exponentially over time ($r = 0.88$ and 0.96 respectively, Figure 2.1A,B), and the bioluminescent signal correlated significantly with the tumor volume assessed by CE-CT imaging ($r = 0.80$, $p \leq 0.01$, $n = 12$, Figure 2.1C). This correlation allowed for BLI-based signal intensity to be used as a substitute for CE-CT imaging.

2.2. Radiation Treatment Planning Allows for Precise Tumor Targeting and Maximal Sparing of Healthy Tissues

In order to optimize tumor targeting with maximal sparing of organs at risk (OARs) during radiation treatment for SOC therapy, four different radiation plans were evaluated using a planned dose of 60 Gy as an example. The resulting dose–volume histograms (DVHs) and dose metrics of the tumor and key OARs for each of the in vivo radiation treatment plan options is shown in Figure 2.2 and Table S1, respectively. The dose–volume metrics indicate that there is no significant difference

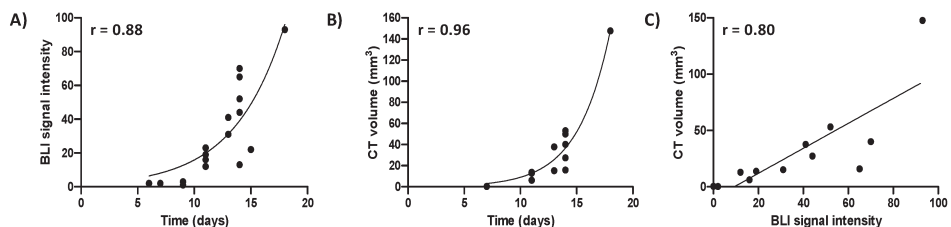


Figure 2.1 - Bioluminescent (BLI) signal intensity and contrast-enhanced (CE)-CT-based tumor volumes are significantly correlated. (A) BLI signal intensity over time of $n = 7$ orthotopic F98 luciferase-expressing glioblastoma (GBM) tumors; (B) CE-CT-derived tumor volume measurements over time of $n = 6$ orthotopic F98 luciferase-expressing GBM tumors; (C) correlation between CE-CT-derived tumor volume and BLI signal intensity for $n = 6$ animals.

in the mean dose delivered to the tumor using each of the plans ($p = 0.54$); all plans deliver $\geq 99\%$ of the expected dose to the tumor area. The uniformity of the dose (as measured by the dose to the hottest 5% (D5) and 95% (D95) of the tumor volume) was also very similar across all four treatment plans, ranging from 102 to 103% and 95 to 98% for average D5 and D95, respectively.

To assess normal tissue sparing, we evaluated the dose delivered to the ipsilateral side of the brain (not including the tumor) and the contralateral side of the brain to the tumor site. On the ipsilateral side, there was no significant difference in mean dose delivered to this area ($p = 0.07$), with all treatment plans sparing this side of the brain $\geq 80\%$ of the planned dose. However, on the contralateral side of the brain, Plan 3 and 4 received a significantly reduced mean dose when compared to Plan 1 and 2 ($p \leq 0.001$), improving normal tissue sparing on this side of the brain from 92 to 97%. For this reason, Plan 1 and 2 were immediately eliminated as possible radiation plan options. Although there was no significant difference in the mean dose received on the contralateral side between Plan 3 and 4 (1.8 and 1.6 Gy, respectively $p = 0.76$), when looking into the uniformity of the delivered dose (minimum dose to the hottest 5% (D5) and 95% (D95) of the area volume), the D5 value for Plan 4 was moderately lower than for Plan 3, suggesting improved tissue sparing. The AP-PA plan (Plan 4) was therefore selected for use in the SOC efficacy experiments.

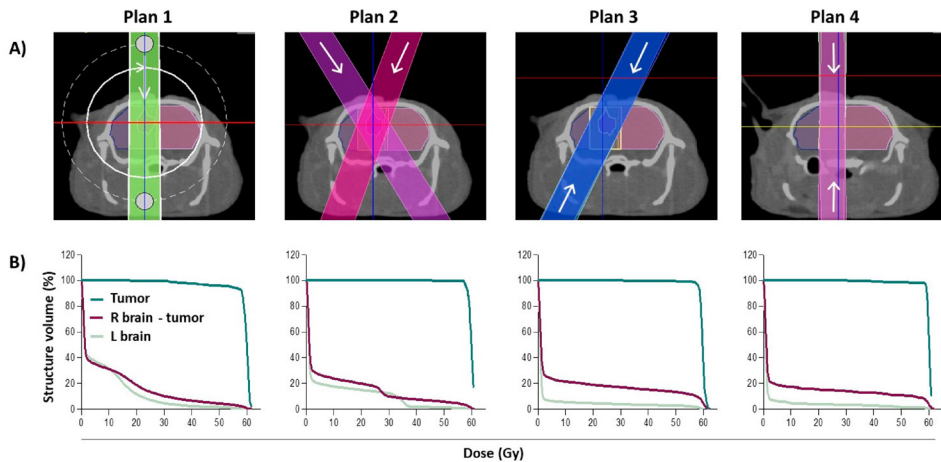


Figure 2.2 - Radiation treatment planning. (A) Representative beam set-up in the axial plane for four radiation treatment plans: Plan 1—360° arc; Plan 2—two angled beams; Plan 3—two angled beams, parallel opposed; Plan 4—anterior/posterior opposed (AP-PA). (B) The corresponding dose-volume histograms for each radiation treatment plan. R brain = right brain; L brain = left brain.

2.2. SOC Treatment Using a Targeted Radiation Strategy Demonstrates Anti-Tumor Efficacy but Is Not Curative

Optimization of the radiation treatment plan allowed for subsequent testing of SOC therapy in this model. A dose response of radiation from 0 to 60 Gy was used in an attempt to determine the dose of radiation that locally controls 50% of the tumors (TCD50). An increase in median survival time was demonstrated for all SOC regimens compared to untreated control animals (on average 5.2 days, $p < 0.05$, log-rank test), but this was not curative for any animals (Figure 2.3A). Surprisingly, there was no relationship between the increase in radiation dose and median survival time. Animals treated with 30 Gy received the largest survival benefit (23.5 days) in comparison to the animals treated with 20 or 60 Gy (19 and 18 days, respectively). In total, 75% of the animals treated with 60 Gy demonstrated $\geq 10\%$ body weight loss, compared to 63% for the 20 and 30 Gy treatment groups (Figure 2.3B). In addition, the body weight loss in the 60 Gy group occurred at an earlier time point on average than in the 30 Gy group (day 16 and 18, respectively), after which there was a steady decline to humane endpoint with no recovery. Radiation dose metrics of the treated animals were analogous to those generated in Plan 4 (AP-PA) during the optimization phase. On average across all treatment groups, the tumor received 96.4% of the expected dose (Table 1). The ipsilateral side of the brain (not including the tumor) was spared on average 84% of the dose. In fact, 95% of this area received ≤ 0.2 Gy, regardless of the administered dose. The remaining 5% of the area was not spared. However, due to the angle of the beams, this was not unexpected. The contralateral side of the brain was even further spared from radiation (by an average of 99% of the dose), thus illustrating our targeted radiation strategy.

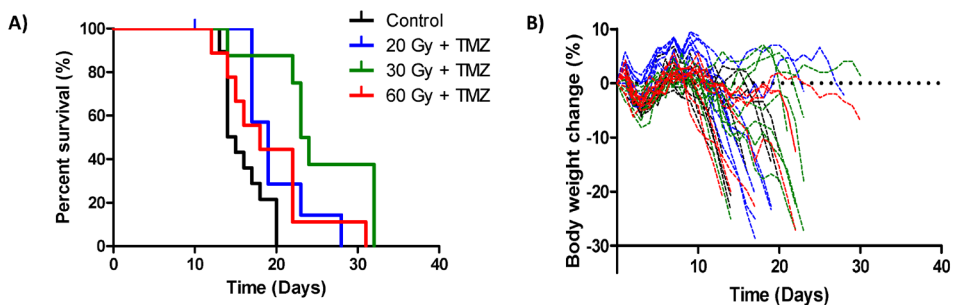


Figure 2.3 - Therapeutic efficacy of standard-of-care (SOC) therapy using a targeted radiation strategy (A) Kaplan–Meier survival curves of animals following orthotopic F98 GBM implantation and a single dose of targeted radiation (as specified) with concomitant temozolomide (TMZ). Survival endpoint was defined as the time an animal left the experiment for humane reasons. $n \geq 8$ animals per treatment group. (B) Body weight loss of the treatment groups over time following surgical implantation of the tumor. Percentage body weight change relative to starting body weight was determined.

Table 2.1 - Dose–volume histogram metrics for different tissue structures (tumor, right brain (R brain) without tumor, and left brain (L brain)) in treated animals (20, 30 or 60 Gy as indicated) using the AP-PA radiation treatment plan (Plan 4). Numbers are the mean and standard deviation of $n \geq 7$ animals per treatment group. D95 = dose to 95% of the target volume; D5 = dose to 5% of the target volume.

Planned Dose (Gy)	Tumor Dose (Gy)			R Brain without Tumor Dose (Gy)			L Brain		
	Mean	D95	D5	Mean	D95	D5	Mean	D95	D5
20 Gy	19.4 ± 0.3	16.8 ± 0.2	22.2 ± 0.3	3.8 ± 0.3	0.00	20.0 ± 0.4	0.11 ± 0.1	0.00	0.09 ± 0.1
30 Gy	28.1 ± 3.0	21.3 ± 1.1	30.4 ± 0.3	4.1 ± 1.5	0.08 ± 0.0	26.1 ± 7.6	0.58 ± 0.4	0.07 ± 0.1	1.1 ± 1.0
60 Gy	59.2 ± 1.5	54.1 ± 9.4	61.0 ± 0.4	9.3 ± 3.8	0.22 ± 0.1	52.9 ± 19	1.2 ± 0.9	0.19 ± 0.1	3.0 ± 4

3. Discussion

Modern techniques have allowed for closer replication of human radiotherapy practice; fractionated therapy is now possible with multiple, conformal beams and sophisticated dose calculation algorithms. However, these methods require high-resolution imaging techniques to allow for precise and accurate beam positioning, particularly when working with orthotopic tumor models such as GBM. CT is the preferred imaging modality for the target delineation and treatment planning of solid tumors using external beam radiation therapy as it most closely mimics clinical practice^[20]. Here, a CT-based treatment planning system (SmART-ATP) allowed for delivery of a highly localized prescribed dose to an isocenter placed at the center of the target (tumor). Dose calculations performed using this set-up result in greater dose homogeneity and minimization of the dose received by the OARs^[4,5,8,9].

The AP-PA beam plan was chosen for the SOC efficacy study as this plan maximized normal tissue sparing. While this plan accurately delivered the proposed radiation dose to the tumor (99% of the planned mean dose was delivered to the experimental tumors), the normal tissue sparing in the experiment was slightly greater than expected, thus exemplifying our targeted irradiation strategy. The ipsilateral side of the brain without the tumor was expected to be spared 82% of the planned dose (49 Gy), but was in fact spared 84% (50 Gy). In addition, the minimum dose for the hottest 5% of this area (D5) was reduced from 59.8 Gy to just 52.9 Gy. It is possible to use other methods for treatment planning, such as MRI, which is generally considered the standard imaging modality for pre-clinical intracranial tumors. Previous reports suggest that MRI and CT-derived GBM tumor volume measurements show a strong correlation in vivo^[21]. However, others have reported that CT was not sufficient to achieve accurate irradiation of the target in a GBM model (although this was performed without contrast)^[22]. MRI was required in the study mentioned to deliver a homogeneous dose using a more complicated arrangement of three non-coplanar arcs. Regardless, in the absence of robust radiation treatment planning software for MRI, additional CT



scans are still required to perform dose calculations, thereby limiting the utility of this approach^[22-24].

Optimization of the radiation treatment plan allowed for subsequent SOC efficacy testing. Although each treatment group individually provided significant additional efficacy when compared to untreated controls, there was no improvement in efficacy with regard to the radiation dose-response tested. Animals in the 30 Gy treatment group received the largest therapeutic benefit and the TCD50 was unable to be determined. This can be explained in part by the body weight loss observed following treatment. Animals in the 60 Gy group suffered from earlier and more severe body weight loss, which had a major impact on overall survival. It is unknown whether this is occurring due to radiation toxicity or tumor progression, although it is likely to be a combination of the two. Others have successfully delivered a single fraction of 60 Gy to rats bearing human GBM, with animals surviving for at least ten weeks after treatment^[25]. However, only a portion of the tumor received 60 Gy in the study mentioned, resulting in severe necrosis in these areas of the tumor^[25]. The clinical symptoms of radiation-induced necrosis include worsening neurologic signs and symptoms and neurocognitive decline^[26], which when extrapolated to whole tumor irradiation could possibly explain the toxicity observed in our study. Standard radiotherapy for patients with GBM is a fractionated schedule of 2 Gy per day, five days per week, for six weeks for a total of 60 Gy^[1]. However, the approximate relative biological effectiveness of this is likely to be closer to 20 Gy^[22]. A hypofractionated schedule might potentially reduce toxicity and improve efficacy in the context of our study (e.g., six fractions of 10 Gy), as hypofractionated radiotherapy schemes have been successfully utilized in patients to improve convenience and tolerance to therapy, particularly in the elderly, where treatment-related toxicities are a main concern^[27,28]. Similar to what is observed in patients, while SOC was therapeutically effective, it was not curative, suggestive again of the clinical relevance of F98 to human GBM. Extensive tumor hypoxia, necrosis, and an infiltrative-like growth pattern of irregular tumor borders and peripheral extension into the surrounding tissue was demonstrated in F98 tumors (Figure S1C,D) and is also frequent in human GBM, being negative prognostic indicators associated with biological and clinical aggressiveness, shorter time to tumor recurrence, and reduced survival^[29,30]. Hypoxic tumor cells are genetically unstable and show increased expression of O6-methylguanine-DNA-methyltransferase (MGMT) expression, a DNA repair enzyme known to negate TMZ-induced DNA alkylation^[31]. Thus, tumor hypoxia is thought to confer resistance to TMZ chemotherapy. Targeting of these hypoxic cells could therefore increase the therapeutic efficacy of TMZ treatment. Hypoxia-activated prodrugs (HAPs) are selectively activated by enzymatic reduction in hypoxic cells, and may provide a means to test this hypothesis. One of the most clinically advanced HAPs, evofosfamide, has successfully demonstrated efficacy

towards glioblastoma in a pre-clinical rodent model^[32] and in human patients^[33] but has yet to be combined with SOC. HAP administration prior to SOC therapy could potentially remove both the TMZ-resistant and radio-resistant hypoxic cells, providing additional benefit to both components of SOC.

Immune suppression also plays an important role in GBM progression through a variety of mechanisms, including recruitment of M2-associated macrophages to the tumor microenvironment^[34] and expression of potent immunosuppressive factors including TGF- β (transforming growth factor beta) and PD-L1 (programmed death-ligand 1)^[35]. In addition, TMZ can induce lymphopenia in malignant glioma patients treated with SOC therapy^[36]. Combining SOC with an immune-stimulating approach could therefore be advantageous. However, recently developed cancer immunotherapies have had disappointing results in this disease setting, likely due to the fact that only a single component of the anti-tumor immune response is targeted^[37]. Tumor-targeting bacteria that can cross the blood-brain barrier such as *Clostridium* could be used to provide an inflammatory payload exquisitely to the tumor microenvironment, potentially combining the innate immune response to infection with effective stimulation of immune memory against the tumor^[38]. Overall, our therapeutic results suggest that a combination of treatment modalities with SOC will be required to improve therapeutic outcome.

In this study, we also demonstrate a significant correlation between bioluminescent signal intensity and tumor volume assessed by CE-CT in the F98 model. Similar correlations ($r > 0.54$) have previously been reported for orthotopic mouse GBM in mice [20,39]. However, these studies were performed using a human primary GBM cell line that lacks key features of clinical GBM^[13]. Importantly, the correlation observed in this study suggests that BLI can be used as a surrogate for CE-CT, reducing the radiation burden of using frequent CE-CT scans for long-term treatment monitoring and providing an integrated platform for GBM evaluation.

4. Materials and Methods

4.1. Generation of the F98 Luciferase-Expressing Cell Line

F98 GBM cells (kindly provided by Prof. C. Vanhove, Ghent University, Belgium) were cultured in DMEM (Dulbecco's modified eagle medium) supplemented with 10% fetal bovine serum (Sigma-Aldrich, Zwijndrecht, Netherlands). Cells were transduced with a lentiviral vector harboring a PGK-driven FLuc+ (pLenti PGK V5-LUC neo (w623-2), a gift from Eric Campeau (Addgene plasmid #21471; <http://n2t.net/addgene:21471>; RRID:Addgene_21471)) [40]. Neomycin selection began 48 h after transduction and after three weeks of continuous selection, cells could be used in experiments. Cells were tested for the presence of mycoplasma prior to injection into animals.

4.2. Orthotopic GBM Tumor Implantation

Implantation of the orthotopic GBM tumors was performed as previously described [22], with some modifications. Briefly, young (8–12 weeks) female F344/IcoCrl rats were ordered from Charles River (s-Hertogenbosch, Netherlands). Then, 30 min prior to surgery, animals were administered analgesia by intraperitoneal injection (buprenorphine, 0.05 mg/kg). Following sedation (first 4% isoflurane in an induction box, then 2.5% for maintenance), each rat was placed in a stereotaxic frame and the top of the skull was shaved and disinfected with isobetadine. A small incision was made through the skin along the length of the middle of the skull and connective tissue was removed using a sterile cotton bud, before the area was treated with lidocaine (1–2%). A burr was used to drill a hole in the skull 2 mm caudal and 2.5 mm right from bregma. In total, 20,000 cells (in 5 μ L of phosphate buffered saline (PBS)) were slowly (2 μ L per minute) injected at a depth of 3 mm. The needle was then left for 5 min to ensure no reflux of cells. The drill hole was closed with bone wax (Aesculap AG®, B.Braun, Melsungen, Germany) and non-absorbable sutures (Ethicon, Johnson & Johnson, Amersfoort, Netherlands) were used to close the incision. Post-operative analgesia was given as required (carprofen, 2–4 mg/kg in the drinking water). All animal experiments were in accordance with local institutional guidelines for animal welfare and approved by the Animal Ethical Committee of the University of Maastricht (Protocol # 2017-012).

4.3. Microscopy

Excised rat brains were fixed in neutral-buffered formalin (4%) before embedding in paraffin wax. Sections (7 μ m) were cut, mounted onto poly-L-lysine-coated slides, and heat-fixed for 30 min at 58 °C. Paraffin was removed and sections were rehydrated using sequential immersions in 100% xylene, 100% ethanol, 80% ethanol, 50% ethanol and 100% distilled water. At this point, hematoxylin and eosin (H&E) staining was performed. Following an additional antigen retrieval step, staining for hypoxia was performed using pimonidazole in accordance with the manufacturer's instructions (Hypoxyprobe™-1 Omni Kit, Hypoxyprobe, Burlington, MA, USA). All images were acquired on a M8 Microscope and Scanner (Precipoint, Freising, Germany).

4.4. Bioluminescence Imaging and Analysis

Under isoflurane anesthesia, whole-body white light and BLI scans from a dorsal position were acquired using an iXon Ultra 897 camera (Andor Technology Ltd., Belfast, United Kingdom) in the X-Rad 225Cx machine (Precision X-ray, Inc, North Branford, CT, USA) using no filters (open modus), ten minutes after intraperitoneal injection of D-luciferin (150 mg/kg, Perkin Elmer, Rotterdam, Netherlands). BLI images were acquired with a gain of 5 and an exposure time of 0.005 s (white light) or 60 s (BLI). Signal intensity parameters were consistent for all images

(either white light or BLI). The cumulative raw BLI intensity signal was corrected with the background signal corresponding to an area on the rat skin distant from the skull.

4.5. Contrast-Enhanced CT (CE-CT) Imaging and Analysis

Under isoflurane anesthesia, CT images of the skull area were acquired using an X-Rad 225Cx small-animal irradiator (Precision X-Ray, Inc) immediately following intravenous injection of contrast-enhancing agent (60 mg/kg Omnipaque, GE Healthcare, Eindhoven, Netherlands). CT acquisition parameters, CT number to density calibration and medium segmentation, were performed as described previously^[41]. The CT imaging dose was 30 cGy. Images were reconstructed using Feldkamp's filtered back-projection (Pilot version 1.14.4, Precision X-Ray, Inc).

4.6. Radiation Treatment Planning and Dose Calculation

Treatment plans based on 1) 360° arc, 2) two angled beams (15°/345°), 3) two angled beams, parallel opposed (15°/195°) and 4) anterior/posterior opposed (AP-PA, 0°/180°) using a 5 mm circular collimator (SmART-ATP version 2.0, Smart Scientific Solutions B.V., Maastricht, Netherlands) were compared for mean dose (D_{mean}), dose to 95% (D₉₅) and dose to 5% (D₅) of the CT-delineated tumor volume. Dose calculations were performed with the Monte Carlo dose engine DOSXYZnrc (National Research Council Canada) using an intrinsic dose uncertainty set to 5% in the target volume. Radiation delivery was performed according to ACROP guidelines as previously described^[42,43]. Briefly, irradiations were performed at 225 kVp and 13 mA, with an inherent 0.8 mm beryllium filter and an additional 0.3 mm copper filter, resulting in a spectrum with a half value layer of 0.98 mm copper. The 5 mm beams had a full-width half maximum of 4.9 mm and a penumbra size of 0.5 mm (20–80% of maximum dose) at the isocenter and a dose rate of approximately 2.5 Gy/min at the source-to-isocenter distance of 303.6 mm. All calculated dose values were scored as dose-to-medium, transport-in-medium.

4.7. Tumor Growth Delay

Tumor-bearing rats were randomized to treatment groups after second positive BLI and first positive CT signal and irradiated with 0, 20, 30 or 60 Gy. Concomitant temozolomide (29 mg/kg, Bioconnect, Huissen, Netherlands) was administered by intraperitoneal injection daily for four days, beginning on the day of irradiation. Tumor growth was monitored 3× per week using BLI and body weight was monitored daily. BLI-based tumor volume was determined by signal intensity and CT-based tumor volume was calculated using a summation of all planes. Animals were sacrificed if body weight loss exceeded 20% of the pretreatment value or if neurological symptoms were observed (humane endpoint). Kaplan–Meier plots were constructed to calculate median time to survival endpoint, defined as the time an animal left the experiment due to

humane endpoint (clinical neurological symptoms and/or body weight loss, indicative of tumor progression). Treatment efficacy was assessed by comparing the median survival time with untreated control animals.

4.8. Statistical Analysis

Statistical analyses (one-way ANOVA, Student's T-test, log-rank test) were performed using GraphPad Prism Software (version 5.03). A p-value < 0.05 was considered statistically significant.

5. Conclusion

In summary, optimization of a targeted RT treatment strategy for GBM resulted in maximum sparing of healthy brain tissue while ensuring accurate delivery of $\geq 99\%$ of the dose to the tumor area. However, it appears that truly effective GBM therapy will require a combination of treatment modalities with SOC to increase therapeutic efficacy and improve clinical outcome. Use of a clinically relevant orthotopic model with multimodal imaging capability such as this will be essential for pre-clinical development in this context.

6. Acknowledgment

This research was funded by the Special Research Fund (BOF) of Hasselt University and Maastricht University Medical Centre+ (BOF17DOCM13) and the Dutch Cancer Society (KWF Unieke Kansen #8025).

References

- [1]. Stupp, R.; Mason, W.P.; van den Bent, M.J.; Weller, M.; Fisher, B.; Taphoorn, M.J.; Belanger, K.; Brandes, A.A.; Marosi, C.; Bogdahn, U.; et al. Radiotherapy plus concomitant and adjuvant temozolomide for glioblastoma. *N. Engl. J. Med.* 2005, 352, 987–996, doi:10.1056/NEJMoa043330.
- [2]. Gilbert, M.R.; Wang, M.; Aldape, K.D.; Stupp, R.; Hegi, M.E.; Jaeckle, K.A.; Armstrong, T.S.; Wefel, J.S.; Won, M.; Blumenthal, D.T.; et al. Dose-dense temozolomide for newly diagnosed glioblastoma: A randomized phase III clinical trial. *J. Clin. Oncol.* 2013, 31, 4085–4091, doi:10.1200/jco.2013.49.6968.
- [3]. Kreisl, T.N.; Kim, L.; Moore, K.; Duic, P.; Royce, C.; Stroud, I.; Garren, N.; Mackey, M.; Butman, J.A.; Camphausen, K.; et al. Phase II Trial of Single-Agent Bevacizumab Followed by Bevacizumab Plus Irinotecan at Tumor Progression in Recurrent Glioblastoma. *J. Clin. Oncol.* 2009, 27, 740–745, doi:10.1200/jco.2008.16.3055.
- [4]. Verhaegen, F.; Granton, P.; Tryggstad, E. Small animal radiotherapy research platforms. *Phys. Med. Biol.* 2011, 56, R55–R83, doi:10.1088/0031-9155/56/12/r01.
- [5]. Verhaegen, F.; van Hoof, S.; Granton, P.V.; Trani, D. A review of treatment planning for precision image-guided photon beam pre-clinical animal radiation studies. *Z. Med. Phys.* 2014, 24, 323–334, doi:https://doi.org/10.1016/j.zemedi.2014.02.004.
- [6]. Lenting, K.; Verhaak, R.; Ter Laan, M.; Wesseling, P.; Leenders, W. Glioma: Experimental models and reality. *Acta neuropathologica* 2017, 133, 263–282, doi:10.1007/s00401-017-1671-4.
- [7]. Killion, J.J.; Radinsky, R.; Fidler, I.J. Orthotopic Models are Necessary to Predict Therapy of Transplantable Tumors in Mice *Cancer Metastasis Rev.* 1998, 17, 279–284, doi:10.1023/A:1006140513233.
- [8]. Yahyanejad, S.; van Hoof, S.J.; Theys, J.; Barbeau, L.M.; Granton, P.V.; Paesmans, K.; Verhaegen, F.; Vooijs, M. An image guided small animal radiation therapy platform (SmART) to monitor glioblastoma progression and therapy response. *Radiother. Oncol.* 2015, 116, 467–472, doi:10.1016/j.radonc.2015.06.020.
- [9]. Sosa Iglesias, V.; van Hoof, S.J.; Vaniqui, A.; Schyns, L.E.; Lieuwes, N.; Yaromina, A.; Spiegelberg, L.; Groot, A.J.; Verhaegen, F.; Theys, J.; et al. An orthotopic non-small cell lung cancer model for image-guided small animal radiotherapy platforms. *Br. J. Radiol.* 2019, 92, 20180476, doi:10.1259/bjr.20180476.
- [10]. D’Alessio, A.; Proietti, G.; Sica, G.; Scicchitano, B.M. Pathological and Molecular Features of Glioblastoma and Its Peritumoral Tissue. *Cancers* 2019, 11, 469, doi:10.3390/cancers11040469.
- [11]. Claes, A.; Idema, A.J.; Wesseling, P. Diffuse glioma growth: A guerilla war. *Acta Neuropathol.* 2007, 114, 443–458, doi:10.1007/s00401-007-0293-7.
- [12]. Barth, R.F.; Kaur, B. Rat brain tumor models in experimental neuro-oncology: The C6, 9L, T9, RG2, F98, BT4C, RT-2 and CNS-1 gliomas. *J. Neuro-oncol.* 2009, 94, 299–312, doi:10.1007/s11060-009-9875-7.
- [13]. Candolfi, M.; Curtin, J.F.; Nichols, W.S.; Muhammad, A.G.; King, G.D.; Pluhar, G.E.; McNeil, E.A.; Ohlfest, J.R.; Freese, A.B.; Moore, P.F.; et

- al. Intracranial glioblastoma models in pre-clinical neuro-oncology: Neuropathological characterization and tumor progression. *J. Neuro-oncol.* 2007, 85, 133–148, doi:10.1007/s11060-007-9400-9.
- [14]. Jacobs, V.L.; Valdes, P.A.; Hickey, W.F.; De Leo, J.A. Current Review of in Vivo GBM Rodent Models: Emphasis on the CNS-1 Tumour Model. *ASN Neuro.* 2011, 3, AN20110014, doi:10.1042/AN20110014.
- [15]. Ko, L.; Koestner, A.; Wechsler, W. Morphological characterization of nitrosourea-induced glioma cell lines and clones. *Acta Neuropathol.* 1980, 51, 23–31, doi:10.1007/bf00688846.
- [16]. Tzeng, J.J.; Barth, R.F.; Orosz, C.G.; James, S.M. Phenotype and functional activity of tumor-infiltrating lymphocytes isolated from immunogenic and nonimmunogenic rat brain tumors. *Cancer Res.* 1991, 51, 2373–2378.
- [17]. Sibenaller, Z.A.; Etame, A.B.; Ali, M.M.; Barua, M.; Braun, T.A.; Casavant, T.L.; Ryken, T.C. Genetic characterization of commonly used glioma cell lines in the rat animal model system. *Neurosurg. Focus* 2005, 19, E1, doi:10.3171/foc.2005.19.4.2.
- [18]. Mathieu, D.; Lecomte, R.; Tsanaclis, A.M.; Larouche, A.; Fortin, D. Standardization and detailed characterization of the syngeneic Fischer/F98 glioma model. *Can. J. Neurol. Sci.* 2007, 34, 296–306, doi:10.1017/s0317167100006715.
- [19]. Bryant, M.J.; Chuah, T.L.; Luff, J.; Lavin, M.F.; Walker, D.G. A novel rat model for glioblastoma multiforme using a bioluminescent F98 cell line. *J. Clin. Neurosci.* 2008, 15, 545–551, doi:10.1016/j.jocn.2007.04.022.
- [20]. Yahyanejad, S.; Granton, P.V.; Lieuwes, N.G.; Gilmour, L.; Dubois, L.; Theys, J.; Chalmers, A.J.; Verhaegen, F.; Vooijs, M. Complementary use of bioluminescence imaging and contrast-enhanced micro-computed tomography in an orthotopic brain tumor model. *Mol. Imaging* 2014, 13, doi:10.2310/7290.2014.00038.
- [21]. Engelhorn, T.; Eyupoglu, I.Y.; Schwarz, M.A.; Karolczak, M.; Bruenner, H.; Struffert, T.; Kalender, W.; Doerfler, A. In vivo micro-CT imaging of rat brain glioma: A comparison with 3T MRI and histology. *Neurosci. Lett.* 2009, 458, 28–31, doi:10.1016/j.neulet.2009.04.033.
- [22]. Bolcaen, J.; Descamps, B.; Deblaere, K.; Boterberg, T.; Hallaert, G.; Van den Broecke, C.; Decrock, E.; Vral, A.; Leybaert, L.; Vanhove, C.; et al. MRI-guided 3D conformal arc micro-irradiation of a F98 glioblastoma rat model using the Small Animal Radiation Research Platform (SARRP). *J. Neuro-oncol.* 2014, 120, 257–266, doi:10.1007/s11060-014-1552-9.
- [23]. Baumann, B.C.; Benci, J.L.; Santoiemma, P.P.; Chandrasekaran, S.; Hollander, A.B.; Kao, G.D.; Dorsey, J.F. An integrated method for reproducible and accurate image-guided stereotactic cranial irradiation of brain tumors using the small animal radiation research platform. *Transl. Oncol.* 2012, 5, 230–237, doi:10.1593/tlo.12136.
- [24]. Gutierrez, S.; Descamps, B.; Vanhove, C. MRI-Only Based Radiotherapy Treatment Planning for the Rat Brain on a Small Animal Radiation Research Platform (SARRP). *PLoS ONE* 2015, 10, e0143821, doi:10.1371/journal.pone.0143821.
- [25]. Kumar, S.; Arbab, A.S.; Jain, R.; Kim, J.; deCarvalho, A.C.; Shankar, A.; Mikkelsen, T.; Brown, S.L. Development of a novel animal model to differentiate radiation necrosis from tumor recurrence. *J. Neurooncol.*

- 2012, 108, 411–420, doi:10.1007/s11060-012-0846-z.
- [26]. Postma, T.J.; Klein, M.; Verstappen, C.C.; Bromberg, J.E.; Swennen, M.; Langendijk, J.A.; Taphoorn, M.J.; Scheltens, P.; Slotman, B.J.; van der Ploeg, H.M.; et al. Radiotherapy-induced cerebral abnormalities in patients with low-grade glioma. *Neurology* 2002, 59, 121–123, doi:10.1212/wnl.59.1.121.
- [27]. Hulshof, M.C.; Schimmel, E.C.; Andries Bosch, D.; Gonzalez Gonzalez, D. Hypofractionation in glioblastoma multiforme. *Radiother. Oncol.* 2000, 54, 143–148, doi:10.1016/s0167-8140(99)00183-8.
- [28]. Ohno, M.; Miyakita, Y.; Takahashi, M.; Igaki, H.; Matsushita, Y.; Ichimura, K.; Narita, Y. Survival benefits of hypofractionated radiotherapy combined with temozolomide or temozolomide plus bevacizumab in elderly patients with glioblastoma aged ≥ 75 years. *Radiat. Oncol.* 2019, 14, 200, doi:10.1186/s13014-019-1389-7.
- [29]. Evans, S.M.; Judy, K.D.; Dunphy, I.; Jenkins, W.T.; Hwang, W.-T.; Nelson, P.T.; Lustig, R.A.; Jenkins, K.; Magarelli, D.P.; Hahn, S.M.; et al. Hypoxia Is Important in the Biology and Aggression of Human Glioblastoma. *Clin. Cancer Res.* 2004, 10, 8177, doi:10.1158/1078-0432.CCR-04-1081.
- [30]. Spence, A.M.; Muzi, M.; Swanson, K.R.; O’Sullivan, F.; Rockhill, J.K.; Rajendran, J.G.; Adamsen, T.C.H.; Link, J.M.; Swanson, P.E.; Yagle, K.J., et al. Regional Hypoxia in Glioblastoma Multiforme Quantified with [18 F]Fluoromisonidazole Positron Emission Tomography before Radiotherapy: Correlation with Time to Progression and Survival. *Clin. Cancer Res.* 2008, 14, 2623–2630, doi:10.1158/1078-0432.Ccr-07-4995.
- [31]. Sørensen, M.D.; Fosmark, S.; Hellwege, S.; Beier, D.; Kristensen, B.W.; Beier, C.P. Chemoresistance and Chemotherapy Targeting Stem-Like Cells in Malignant Glioma. In *Stem Cell Biology in Neoplasms of the Central Nervous System*, Ehtesham, M., Ed. Springer International Publishing: Cham, Switzerland 2015; pp. 111–138.
- [32]. Stokes, A.M.; Hart, C.P.; Quarles, C.C. Hypoxia Imaging With PET Correlates With Antitumor Activity of the Hypoxia-Activated Prodrug Evofosfamide (TH-302) in Rodent Glioma Models. *Tomography* 2016, 2, 229–237, doi:10.18383/j.tom.2016.00259.
- [33]. Brenner, A.; Zuniga, R.; Sun, J.D.; Floyd, J.; Hart, C.P.; Kroll, S.; Fichtel, L.; Cavazos, D.; Cafilisch, L.; Gruslova, A.; et al. Hypoxia-activated evofosfamide for treatment of recurrent bevacizumab-refractory glioblastoma: A phase I surgical study. *Neuro-Oncol.* 2018, 20, 1231–1239, doi:10.1093/neuonc/ny015.
- [34]. Zhou, W.; Ke, S.Q.; Huang, Z.; Flavahan, W.; Fang, X.; Paul, J.; Wu, L.; Sloan, A.E.; McLendon, R.E.; Li, X.; et al. Periostin secreted by glioblastoma stem cells recruits M2 tumour-associated macrophages and promotes malignant growth. *Nat. Cell Biol.* 2015, 17, 170–182, doi:10.1038/ncb3090.
- [35]. Berghoff, A.S.; Kiesel, B.; Widhalm, G.; Rajky, O.; Ricken, G.; Wohrer, A.; Dieckmann, K.; Filipits, M.; Brandstetter, A.; Weller, M.; et al. Programmed death ligand 1 expression and tumor-infiltrating lymphocytes in glioblastoma. *Neuro-Oncol.* 2015, 17, 1064–1075, doi:10.1093/neuonc/nou307.
- [36]. Sengupta, S.; Murrinan, J.; Frishman, C.; Sampath, P. Impact

- of temozolomide on immune response during malignant glioma chemotherapy. *Clin. Dev. Immunol.* 2012, 2012, 831090, doi:10.1155/2012/831090.
- [37]. McGranahan, T.; Therkelsen, K.E.; Ahmad, S.; Nagpal, S. Current State of Immunotherapy for Treatment of Glioblastoma. *Curr. Treat. Options Oncol.* 2019, 20, 24–24, doi:10.1007/s11864-019-0619-4.
- [38]. Staedtke, V.; Bai, R.Y.; Sun, W.; Huang, J.; Kibler, K.K.; Tyler, B.M.; Gallia, G.L.; Kinzler, K.; Vogelstein, B.; Zhou, S.; et al. Clostridium novyi-NT can cause regression of orthotopically implanted glioblastomas in rats. *Oncotarget* 2015, 6, 5536–5546, doi:10.18632/oncotarget.3627.
- [39]. Kirschner, S.; Felix, M.C.; Hartmann, L.; Bierbaum, M.; Maros, M.E.; Kerl, H.U.; Wenz, F.; Glatting, G.; Kramer, M.; Giordano, F.A.; et al. In vivo micro-CT imaging of untreated and irradiated orthotopic glioblastoma xenografts in mice: Capabilities, limitations and a comparison with bioluminescence imaging. *J. Neurooncol.* 2015, 122, 245–254, doi:10.1007/s11060-014-1708-7.
- [40]. Campeau, E.; Ruhl, V.E.; Rodier, F.; Smith, C.L.; Rahmberg, B.L.; Fuss, J.O.; Campisi, J.; Yaswen, P.; Cooper, P.K.; Kaufman, P.D. A Versatile Viral System for Expression and Depletion of Proteins in Mammalian Cells. *PLoS ONE* 2009, 4, e6529, doi:10.1371/journal.pone.0006529.
- [41]. Granton, P.V.; Dubois, L.; van Elmpt, W.; van Hoof, S.J.; Lieuwes, N.G.; De Ruyscher, D.; Verhaegen, F. A Longitudinal Evaluation of Partial Lung Irradiation in Mice by Using a Dedicated Image-Guided Small Animal Irradiator. *Int. J. Radiat. Oncol.* 2014, 90, 696–704, doi:10.1016/j.ijrobp.2014.07.004.
- [42]. Verhaegen, F.; Dubois, L.; Gianolini, S.; Hill, M.A.; Karger, C.P.; Lauber, K.; Prise, K.M.; Sarrut, D.; Thorwarth, D.; Vanhove, C.; et al. ESTRO ACROP: Technology for precision small animal radiotherapy research: Optimal use and challenges. *Radiother. Oncol.* 2018, 126, 471–478, doi:10.1016/j.radonc.2017.11.016.
- [43]. Spiegelberg, L.; van Hoof, S.J.; Biemans, R.; Lieuwes, N.G.; Marcus, D.; Niemans, R.; Theys, J.; Yaromina, A.; Lambin, P.; Verhaegen, F.; et al. Evofosfamide sensitizes esophageal carcinomas to radiation without increasing normal tissue toxicity. *Radiother. Oncol.* 2019, 141, 247–255, doi:10.1016/j.radonc.2019.06.034.

Supplementary Material

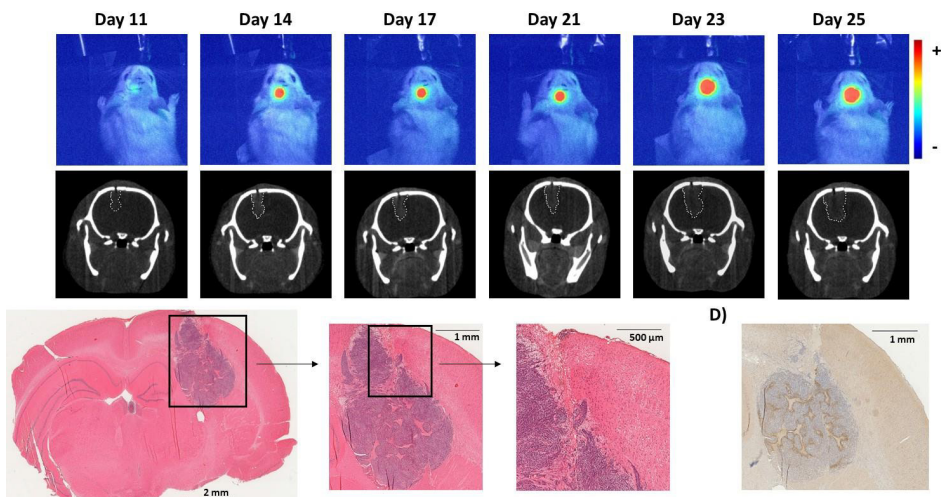


Figure S1 - F98 tumor growth over time as determined by non-invasive BLI and CE-CT imaging. (A) Representative 2D BLI images overlaid over the white light image of the animal and (B) The corresponding CE-CT images of the same animal (tumor delineated in white). Both image sets are at selected time points after surgical implantation of F98 cells in the brain. Representative (C) H&E and (D) Pimonidazole (hypoxia) GBM image.

Table S1 - Dose-volume histogram metrics for different tissue structures (tumour, right brain (R brain) without tumour, left brain (L brain)) using the four different radiation plans described in Figure 3. Prescribed dose was 60 Gy. Numbers are the mean and standard deviation of $n = 4$ individual animals bearing an orthotopic F98 GBM. D95 = dose to 95% of the target volume, D5 = dose to 5% of the target volume.

Plan	Tumor Dose (Gy)			R Brain without Tumor Dose (Gy)			L Brain		
	Mean	D95	D5	Mean	D95	D5	Mean	D95	D5
Plan 1	59.5 ± 0.5	57.1 ± 2.1	61.2 ± 0.2	10.3 ± 0.7	0.30 ± 0.00	52.6 ± 3.5	6.2 ± 0.8	0.25 ± 0.05	24.3 ± 3.0
Plan 2	59.8 ± 0.2	58.2 ± 0.4	61.6 ± 0.7	10.4 ± 1.0	0.25 ± 0.05	56.1 ± 2.1	3.7 ± 1.7	0.23 ± 0.04	24.3 ± 8.9
Plan 3	59.7 ± 0.3	58.6 ± 0.4	60.9 ± 0.2	12.3 ± 0.9	0.30 ± 0.00	60.0 ± 0.3	1.8 ± 0.9	0.23 ± 0.04	5.0 ± 6.3
Plan 4	59.9 ± 0.1	57.1 ± 0.1	61.2 ± 0.3	11.0 ± 1.3	0.25 ± 0.05	59.8 ± 0.4	1.6 ± 0.7	0.23 ± 0.04	3.5 ± 3.2

Chapter 3

A deep learning and Monte Carlo based framework for bioluminescence imaging center of mass-guided glioblastoma targeting

Authors

Behzad Rezaeifar, Cecile J.A. Wolfs, Natasja G. Lieuwes, Rianne Biemans, Brigitte Reniers, Ludwig J. Dubois, Frank Verhaegen.

Adopted From

Phys Med Biol. 2022 Jul 8;67(14). doi: 10.1088/1361-6560/ac79f8

Abstract

Objective: Bioluminescence imaging (BLI) is a valuable tool for non-invasive monitoring of glioblastoma multiforme (GBM) tumor-bearing small animals without incurring x-ray radiation burden. However, the use of this imaging modality is limited due to photon scattering and lack of spatial information. Attempts at reconstructing bioluminescence tomography (BLT) using mathematical models of light propagation show limited progress.

Approach: This paper employed a different approach by using a deep convolutional neural network (CNN) to predict the tumor's center of mass (CoM). Transfer-learning with a sizeable artificial database is employed to facilitate the training process for, the much smaller, target database including Monte Carlo (MC) simulations of real orthotopic glioblastoma models. Predicted CoM was then used to estimate a BLI-based planning target volume (bPTV), by using the CoM as the center of a sphere, encompassing the tumor. The volume of the encompassing target sphere was estimated based on the total number of photons reaching the skin surface.

Main Results: Results show sub-millimeter accuracy for CoM prediction with a median error of 0.59 mm. The proposed method also provides promising performance for BLI-based tumor targeting with on average 94% of the tumor inside the bPTV while keeping the average healthy tissue coverage below 10%.

Significance: This work introduced a framework for developing and using a CNN for targeted radiation studies for GBM based on BLI. The framework will enable biologists to use BLI as their main image-guidance tool to target GBM tumors in rat models, avoiding delivery of high x-ray imaging dose to the animals.

1. Introduction

In recent years, small animal image-guided irradiation platforms have boosted pre-clinical cancer research. These platforms ensure accurate treatment planning and dose delivery to animal models^{[1]-[4]}. They often use integrated cone-beam computed tomography (CBCT) as their primary anatomical image guidance system. Due to limited soft-tissue contrast, often contrast-enhanced CBCT is needed to improve tumor segmentation accuracy. However, in some cases, such as glioblastoma multiforme (GBM), tumor visibility is low even with contrast agents. Furthermore, despite recent advances in precision imaging systems dedicated to small animals, current state-of-the-art systems deliver a substantial imaging radiation dose to achieve the highest resolution required for targeting^[5]. There have been several attempts to reduce the delivered dose by using magnetic resonance (MR) guided treatment planning^{[6]-[8]}. However, since this technology is not yet integrated into modern pre-clinical irradiation platforms, CT-MR registration is required, which causes geometric uncertainties^[4].

Bioluminescence imaging (BLI) can be a compelling option to facilitate image-guided radiotherapy. BLI relies on optical photons emitted by a chemical reaction between an enzyme and a corresponding injected substrate. In most in vivo BLI experiments, tumor cells are genetically modified to express firefly luciferase before implantation. Since these genetically modified cells are the only ones in the animal's body that generate such enzymes, only these cells emit light upon activation. Therefore, hereafter the terms tumor and light source are used interchangeably.

BLI is performed by capturing the emitted photons outside the animal's body. Therefore, it can provide fast in vivo images with minimal background noise and no radiation dose. Currently, BLI is mainly used to acquire 2D projection images, possibly at several angles. Figure 3.1 shows a schematic representation of a small animal irradiation platform (X-Rad 225Cx, Precision X-ray, Inc., North Branford, CT)^[9], an acquired slice of a CBCT volume, the result of Monte Carlo (MC) simulation of optical photons emerging from the skin, and the BLI observations. However, the lack of 3D spatial information, i.e. depth, shape and location, of the photon-emitting volume, as shown in Figure 3.1(d), currently limits BLI use in small-animal preclinical cancer research. Thus, the development of accurate 3D bioluminescence tomography (BLT) reconstruction algorithms can open new doors for pre-clinical image-guided radiotherapy. In addition, BLT allows targeting selective regions inside tumors with ionizing radiation, investigating the tumor response to treatment, and many other research opportunities^{[10], [11]}. However, due to the limitations of the BLI-based targeting, a sub-millimeter targeting accuracy is considered satisfactory but there are no available guidelines or consensus about it.

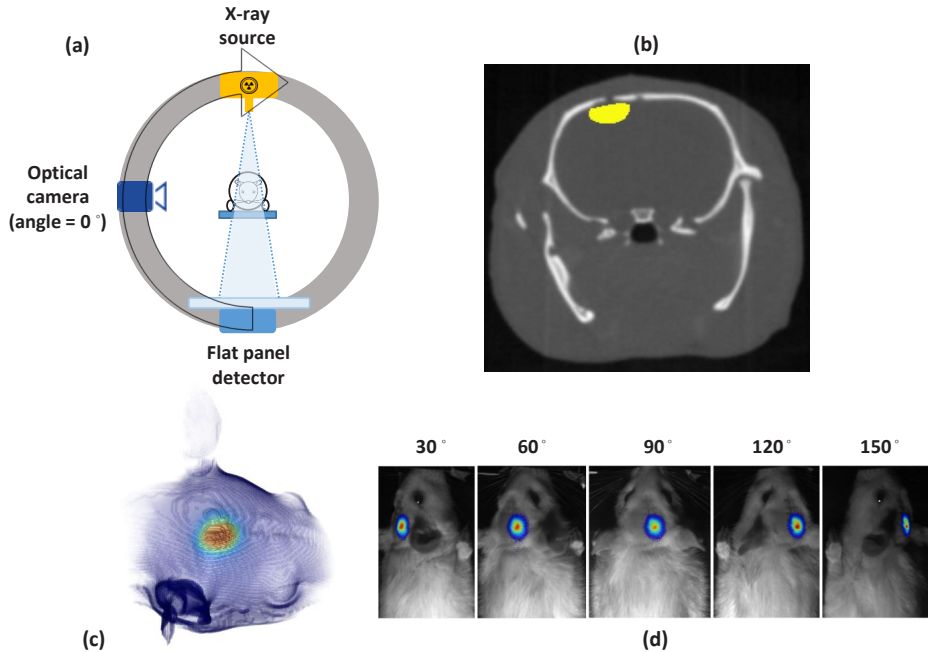


Figure 3.1 - Small animal irradiation platform (X-Rad 225Cx, Precision X-ray, Inc.): (a) design of the integrated irradiation and imaging system (b) acquired micro-CBCT slice in an axial plane with hand-delineated tumor contour overlaid in yellow (c) surface rendering of Monte Carlo simulation of optical photons emerging from the skin (d) measured BLI signal at different angles, with the reference specified in (a), projected onto the optical light image.

Due to its importance in animal studies, much effort has been spent developing BLT reconstruction algorithms^{[12]-[18]}. However, the reconstruction problem remains a challenge, and most of the commercial small-animal image-guided irradiators lack comprehensive BLT capabilities. Therefore, the development of novel methods to tackle this problem continues to be an active research area. We can categorize the current state-of-the-art methods into model-based^{[17], [18]} and deep learning (DL) based algorithms^[15].

Model-based reconstruction methods aim to mathematically model light propagation inside the biological tissue and then solve the derived highly ill-posed inverse problem to reconstruct the 3D source distribution. These conventional methods require several estimations and approximations to solve the mathematical models that introduce errors in the final solution^[15]. DL-based algorithms, on the other hand, utilize artificial intelligence (AI) to find the optimal solution and avoid modeling errors. It has been shown that AI can tackle many complicated inverse problems more efficiently than model-based counterparts^[19]. To the best of our knowledge, the use of AI for BLT reconstruction has been limited to the work of Gao et al^[15]. Gao's method consisted of registering all the possible inputs to a standard mesh, predicting the light source within the standard mesh, and then transferring back to the original space.

However, the registration algorithm embedded within Gao's method can contribute considerably to the geometrical uncertainty. Furthermore, the multi-layer perceptron architecture used by Gao limits the maximum resolution or the depth of the DL algorithm that can be used.

This paper proposes a deep learning-based framework to improve BLT-guided radiation targeting for orthotopic GBM tumors. While Gao's method relies on registration, the proposed solution uses 3D photon counting at the skin boundary to predict the tumor's center of mass (CoM) and provides a unified solution for different geometries. The presented method employs deep convolutional neural networks (CNNs), allowing higher input resolution compared to Gao. In addition, the proposed deep learning framework eliminates the necessity of image registration by employing transfer learning. Initially, a CNN is trained to predict the light source within a unique standard geometry. The acquired knowledge is then transferred to a second CNN to predict the light source in a variety of head geometries.

2. Materials and Methods

The general framework, shown in Figure 3.2, consists of three main steps: (1) Monte Carlo computation of 3D bioluminescence skin fluence (BSF) starting from optical photons emitted from a volume source embedded in the specimen, (2) predicting the center of mass (CoM) of the source volume using a CNN, and (3) defining the targeting volume based on the estimated tumor volume. Here, we consider the BSF as the number of optical photons emerging from the skin boundary. In vivo experiments, BSF can be obtained using backprojection of the 2D BLI images recorded by the BLI camera onto the skin surface of the CBCT image^[9]. Currently, most BLI cameras only record under discrete angles, which results in a discrete sampling of the full BSF under specific angles. However, in this paper a continuous BSF is directly computed using Monte Carlo simulations, bypassing modeling the camera under various angles and the backprojection procedure. In addition, modelling of the optical camera would cause the simulations to be very slow and highly inefficient.

In this study, two sets of MC simulations of BSF are employed to create pre-training and real-case databases. The pre-training database contains a large number of tumor cases inside a reference geometry of one rat, while the real-case database includes the simulation output of several real rat GBM cases. By using the pre-training database, we allow a deep CNN to learn general features from observations inside a unique arbitrary geometry and then use transfer learning to generalize the acquired knowledge to a wide variety of rat head geometries. Subsequently, a regression model is used to estimate the tumor volume based on the input BSF. Then, assuming a spherical target volume, the predicted CoM and CBCT-based tumor volume can determine the target volume. A total number of 57 labeled CBCT images are used in this study. This

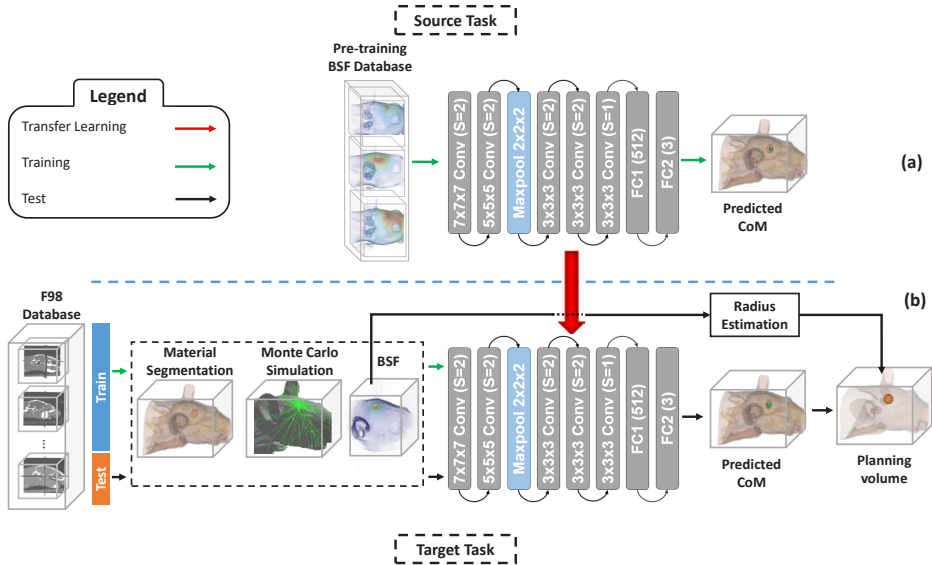


Figure 3.2 – The proposed framework, consisting of: (a) source training on a pre-training database, consisting of the simulated bioluminescence skin fluence (BSF) of different artificial tumors inside a unique standard geometry (b) target training on the real-case database

dataset is augmented to create the pre-training database containing 40,000 samples. The implementation details of the data augmentation algorithm is discussed in the supplementary materials B. The data within each database is split randomly into training, validation and test sets. Furthermore, 12-fold cross-validation is used to assess the deep learning model’s performance on the real-case database. This means that the real-case database is split into twelve parts, and a model is trained on 11 parts and tested on the 12th part. This process is repeated for each of the 12 folds. This method is beneficial in evaluating small databases and allows the model to be trained and tested on all the samples in the database. Eventually, the quantified overlap between the predicted target volume and tumor volume will be considered as objective quality metric.

2.1. Monte Carlo simulations

In order to reconstruct the light source from the physical observations, i.e., 2D BLI images acquired with a camera, an accurate forward photon transport model is first needed. In this study, MC simulations with the GATE framework^[20] were employed as the forward model of light propagation to build the necessary databases. Four major assumptions were made prior to the simulations: (1) tumors are uniformly labeled with the light-emitting agents, (2) emission intensity is constant during the short imaging time, (3) the only materials in the region of interest are bone, brain, air, and water, and (4) light scattering and absorption is governed by constant scattering and absorption coefficients per material. The first two assumptions cause the simulations to have a constant

number of emitted photons per unit volume, i.e., a voxel, while the latter two introduce simplification to the simulation geometry and the model. The starting point of this study was previous in vivo experiments of an F98 rat orthotopic glioma model^[21]. Contrast-enhanced CBCT (CE-CBCT) images, with 0.1 mm resolution in all directions, were acquired at different time points in a tumor-growth study from 35 different animals resulting in 57 images in total. The brain hemispheres and tumor were carefully hand-delineated by trained specialists on each of these images. Hereafter, this database will be referred to as the F98 database.

All the images are padded or cropped into a single grid size of 375x450x375, equal to the most common size in the database, providing a fixed size. Furthermore, the Hounsfield units (HU) are converted to mass density using the corresponding calibration curve, generated using a piecewise bi-linear fit between the mean HU and the mass density of specific materials in the calibration phantom^[22]. Subsequently, the simulation geometry is built by segmenting the mass density images into brain, water, air, and bone. The brain is considered as the hand-delineated contour. Bone and air contours are obtained by thresholding the mass density image with their corresponding thresholds. Everything else in the image is considered as water. Eventually, the geometry of the simulations is configured by assigning optical properties to different tissue segments. Figure 3.3 shows the reduced scattering (μ'_s) and absorption coefficients (μ_a) of brain and bone tissues used in this study^[23],^[24]. In addition, the predefined optical properties in GATE are used for water and air. The optical source is defined based on the tumor contour with a similar emission spectrum as firefly luciferase^[25] and the same

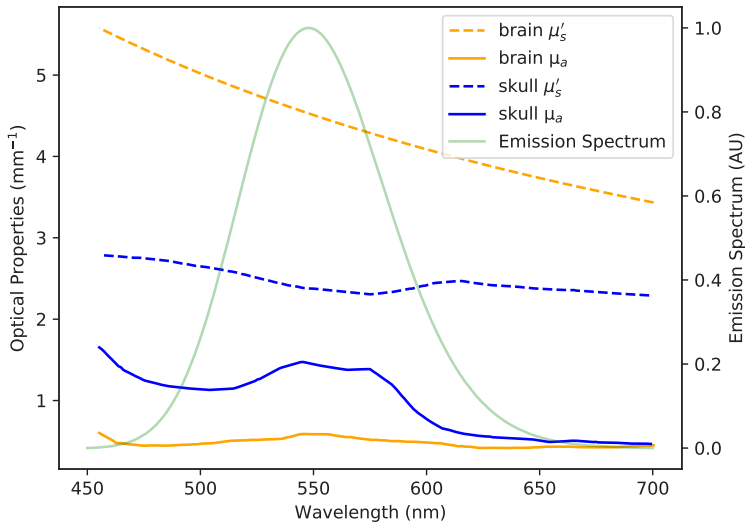


Figure 3.3 - Optical properties spectrum of brain and bone, and photon emission spectrum used in the Monte Carlo simulations [23]–[25]

optical properties as the brain tissue (Figure 3.3). Finally, to decrease memory usage and simulation time, the resulting simulation geometry is downscaled to a 250x300x250 grid with a resolution of 0.1551 mm³.

2.1.1. Pre-training database

The pre-training database is constructed to include a large number of possible tumor variations inside a single reference geometry (i.e., a single rat specimen). Figure 3.4 displays the workflow used to build the pre-training database. Initially, one of the F98 samples, in which the region of interest is located in the center of the 3D volume and there is no bed present in the image, is chosen as the reference geometry. However, instead of directly simulating different tumor shapes and positions, an indirect approach, based on the superposition principle, is used in this study. In other words, the output of the MC simulation for any arbitrary tumor shape is represented by the sum of the outputs of independent simulations of smaller volume units within the tumor.

After obtaining the simulation geometry as described in the previous section, the brain is further partitioned into small voxel-like portions called super-voxels, as shown in Figure 3.4. Each of the super-voxels includes several adjacent voxels grouped to decrease the total number of required simulations. Super-voxels are often cubical, except the super-voxels located at the edge of the brain. Subsequently, a MC simulation is done for every super-voxel inside the brain, assuming that the super-voxel is the light source. Therefore, after repeating this procedure for every super-voxel inside the brain, the simulation output of any arbitrarily shaped tumor can be obtained by superposition of the output of the MC simulations for constituent super-voxels. However, there is always a trade-off between the number of available tumor cases covering all the possible shapes, based on the size of the super-voxels, and the computational cost. In other words, larger super-voxels limit the size

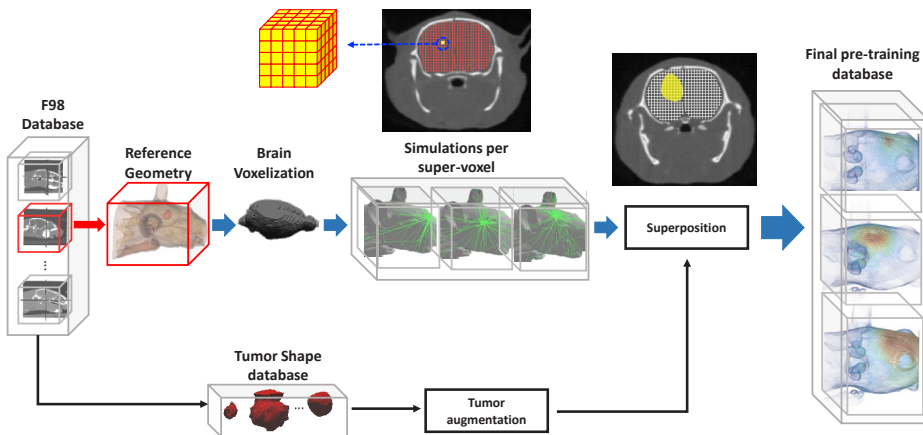


Figure 3.4 – Workflow used to build the pre-training database

and shape variety of the tumors quite drastically while reducing the number of MC simulations needed. In this study, the maximum size of the super-voxels is $5 \times 5 \times 5$ voxels, resulting in a minimum resolution of 0.77 mm^3 compared to the original resolution of 0.1551 mm^3 .

The required simulations and consequently the simulation time for building the pre-training database are substantially reduced with the method described above. Nonetheless, the brain includes several hundred thousand voxels in a micro-resolution CBCT. Therefore, even with the super-voxel scheme, thousands of MC simulations are still needed to build the pre-training database. To decrease the computation time per simulation, we disabled the optical absorption process in the simulations for the pre-training database only, since tracking the many scattering interactions of photons which end up being absorbed before reaching the skin is highly inefficient. However, disabling absorption in the MC simulations causes errors in the BSF since a photon might reach places far away from the source, which it would not be able to reach in reality. Nevertheless, the pre-training database serves to establish a crude relation between the geometry of the light source and the BSF, which will then in subsequent steps be refined.

Once the BSF is known for every super-voxel, a realistic database of tumor cases is needed to build the pre-training database. In this study, the hand-delineated tumor contours of the F98 database are used as the possible tumor shapes. The tumor shape database is further augmented by applying semi-random affine transformations, with zero translation, to the initial shapes. The augmentation algorithm is designed semi-randomly to ensure that all the real shapes, with exact scale and orientation, are present in the final database, as well as a large population of random cases. Then, for each case in the augmented shape database, a vector of all the possible coordinates for the tumor's central placement is calculated, where the entire tumor is encapsulated inside the brain. The final pre-training database consists of the tumor cases that resulted from random sampling of the coordinate vector. This way, we increased the size of the pre-training database drastically to more than 40,000 cases. Finally, the MC-simulated BSF is obtained for each of these cases by combining the simulation output corresponding to super-voxels inside the tumor.

2.1.2. Real case simulations

In the second database, hereafter referred to as real-case database, one MC simulation is performed for each of the samples in the F98 animal experiment. In contrast to the pre-training database, one simulation geometry is constructed for each animal, based on their respective CE-CBCT head volume, as described before. In addition, the light source is considered as the hand-delineated tumor contour. Furthermore, the photon absorption process is modelled in the MC simulations for this database to better fit the actual measurements.

2.2. CNN-based Center of Mass predictor

This study uses a 3D CNN consisting of five convolutional layers, one max-pooling layer, and two fully connected layers to predict the tumor's CoM (Figure 3.2). The network's input consists of the normalized 3D BSF at the skin level, and the output is the set of 3D coordinates of the tumor's CoM. Input normalization is performed by rescaling the values of 3D BSF within the range $[0,1]$. The hyperparameters of the network are optimized by a manual grid search using the pre-training database. Furthermore, an on-the-fly data augmentation algorithm, consisting of rigid-body transformation, is implemented for the real-case training phase to increase model robustness and generalizability. The aforementioned transformation includes small random rotations around the sagittal axis and translation since the prone animal is supported by a bed and an anesthesia nose cone. In addition to data augmentation, we included additive Gaussian noise in the on-the-fly data augmentation algorithm to make the model more robust against realistic measurement noise.

As shown in Figure 3.5, the training process consists of the following steps: (i) collection of pre-processing steps including normalization and on-the-fly augmentation, (ii) applying the current state of the CNN model to the data and predicting the CoM, (iii) comparing the predicted CoM with the ground truth based on a loss function and (iv) adjusting the parameters of the CNN model to minimize to the error. In this paper, we used the mean squared error (MSE) as the loss function determining the error between the predictions and the ground truth. Furthermore, an early stopping criterion based on the best validation loss is implemented to avoid possible overfitting.

The proposed framework utilizes transfer learning to improve the learning procedure. Transfer learning consists of first training a model on a general large database and then fine-tuning that model for a specific task^[26]. As a result, the pre-trained model learns the most important features from a sufficiently meaningful database and fine-tunes the learned knowledge to fit best to the target problem. Romero et al. showed transfer learning is beneficial in cases with small-size training database, only if the pre-training corresponds to the same anatomical site as the target problem. In other words, the similarity between pre-training and the target databases can impact the performance of the deep learning model^[27]. Therefore, in this study, both pre-training and real-case databases are built using MC simulations, thus ensuring the similarity between source and target task. However, there are still two major differences: (1) the pre-training database consists of various tumor shapes inside a unique head geometry while this is not the case for the real-case database, and (2) MC simulation in the pre-training database is done without considering optical photon absorption. Subsequently, any solution on the source domain cannot achieve high performance when directly applied on the target domain. Therefore, weights trained during the pre-training are transferred to a new identical model as the

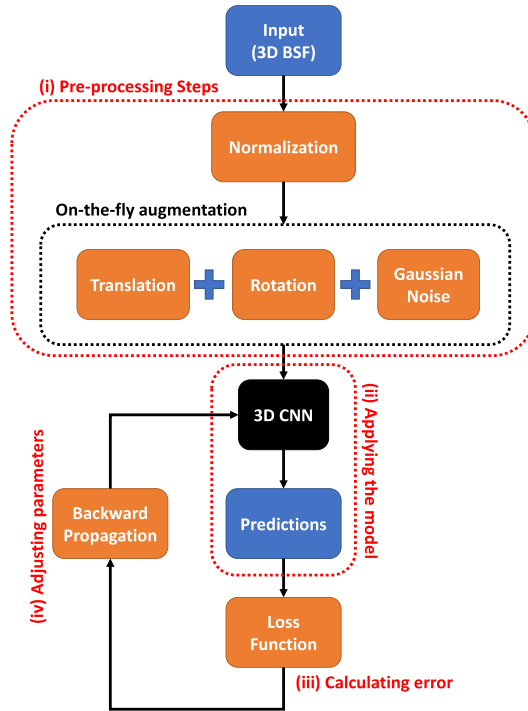


Figure 3.5 – details of the training process: 3D bioluminescence skin fluence (BSF) is used as input for the network after pre-processing steps and the parameters of the network are adjusted based on the loss function, i.e. mean square error.

initial weights. This process is known as transfer learning^[26] and is often used to overcome issues caused by small-sized training database in the target task. As a result, the new model can employ the acquired prior knowledge in the context of the target problem. Consequently, all the transferred weights are re-trained using the real-case database to yield the best result. Further details about the implementation of the transfer learning algorithm used in this paper are provided in the Supplementary Material, section C.

2.3. Targeting planning volume

In this study, the hand-delineated CBCT-based tumor contours are considered the ground truth for the gross tumor volume (GTV). The GTV is further simplified and approximated as the enclosing sphere containing the tumor since almost all commercially available small animal irradiators currently lack the capability to shape complex radiation fields and offer mostly circular or rectangular fields [4]. Furthermore, tumors are typically irradiated with substantial geometric margins to avoid tumor miss and take tumor motion and setup uncertainties into account^[28]. Therefore, we can estimate the BLI-based GTV (bGTV) and build the corresponding planning target volume (PTV) with the predicted tumor's

CoM and volume. Tumor cells are the only bioluminescence light emitter inside the animal resulting in an almost zero background signal. Thus, the total number of detected photons correlates linearly with the tumor volume^{[17], [21]}. Therefore, tumor volume can be estimated by performing logistic regression between the total number of surface photon counts and the tumor volume in the training database.

Once the BLI-based gross tumor volume (bGTV) is obtained, a sphere around the predicted CoM is considered as the bioluminescence-based PTV (bPTV). The radius of the bPTV is calculated based on equation (1)

$$R = \sqrt[3]{\frac{3}{4\pi}bGTV} + m \quad (1)$$

Where bGTV is the bioluminescence-based gross tumor volume and m is a constant margin. Here, the sum of the average CoM and volume prediction uncertainties is considered as the margin (Equation 2).

$$m = u_{CoM} + u_{volume} \quad (2)$$

This study uses two metrics to evaluate the predicted bPTV, namely tumor and healthy tissue coverage. We defined the coverage metric for the tissue of interest as follows:

$$C_{tissue} = \frac{V_{tissue}^{bPTV}}{V_{tissue}^{total}} \quad (3)$$

Where V_{tissue}^{bPTV} and V_{tissue}^{total} correspond to the number of voxels inside the predicted planning volume and the total number of voxels for each specific tissue. In an ideal case, the algorithm should score 0% healthy tissue coverage while targeting all of the tumor. However, this is not feasible due to the spherical approximation of the tumor shape.

In order to underline the inherent uncertainties of the proposed method and their contribution to the targeting accuracy, the coverage metrics are employed in four different scenarios: (a) the ideal case in which both CoM and tumor volume are estimated perfectly with zero error, namely GT1, (b) the situation where the CoM is perfectly captured but the tumor volume is estimated according to the proposed solution, GT2, (c) the case in which the volume is predicted accurately with no error but CoM is predicted using the CNN network, referred as GT3, and (d) both CoM and volume are predicted according to the presented solution. Furthermore, the three ideal cases, namely GT1-3, do not contain any added margin ($m = 0$) to allow a fair investigation of each

uncertainty source in the proposed framework and show the effect of added margin. Consequently, separating the effect of each prediction uncertainty provides a better understanding of the proposed method and its limitations.

Results

The performance of the proposed method is evaluated in two parts: (1) CoM prediction accuracy and (2) planning coverage evaluations. For the former, we investigated the CoM predictions using the ΔCoM metric, which measures the Euclidean distance in millimeter between the CT-based and predicted CoM. For the latter, tumor and healthy tissue coverage metrics are obtained, which quantify which percentage of each tissue falls inside the planning volume (Eqs 2-3). This section describes all the objective measures with the median, interquartile range, and outliers. The proposed method provided excellent performance in ΔCoM . As shown in Figure 3.6, the proposed method can achieve submillimeter accuracy in CoM predictions in both databases. The median ΔCoM in the pre-training database is around 0.1 mm with an interquartile range of 0.12 mm which is of the same order as the image slice thickness in the CT image (0.1 mm). The method's performance decreased when moving to the real-case database with a median and interquartile range

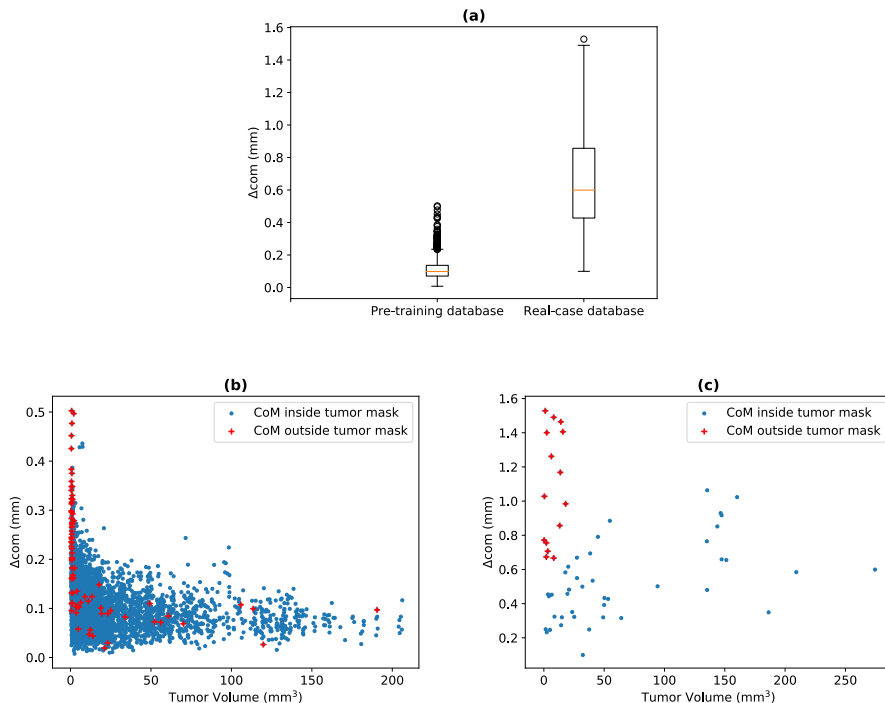


Figure 3.6 - Performance evaluation of the proposed method in CoM prediction: (a) comparison of model performance in pre-training and real-case database (b) scatter plot of ΔCOM vs tumor volume in pre-training database (c) scatter plot of ΔCOM vs tumor volume real-case database

of 0.6 ± 0.43 mm with only one outlier of 1.5 mm, corresponding to a 1 mm³ tumor. Figure 3.6 (b) and (c) show the variation of ΔCoM based on the tumor volume in each database. As shown in Figure 3.6 (b), the proposed method can provide accurate results for various tumor sizes and in most cases the predicted CoM falls within the boundaries of the tumor. However, the model struggles to predict the CoM for very small tumors, with a volume smaller than 10 mm³ (about 2700 image voxels), since the resulting BSF is relatively small and susceptible to noise. In practice, targeting tumors below 10 mm³ is very challenging because it would require beams of approximately 1-3 mm. If we exclude the results of this category of tumors, the model performance improves to 0.5 ± 0.4 mm. In addition to accurate predictions, DL models can provide fast inference. The proposed network's average prediction time is 18.87 ± 0.04 ms on an NVIDIA Quadro RTX 5000 GPU (Santa Clara, CA, USA). Figure 3.7 underlines the importance of transfer learning with the pre-training database in the proposed framework. In this figure, two models have been trained with an identical training database: one is a raw model with randomly initialized weights and the other model is the result of pre-training. These two models are referred to as model without and with transfer learning in Figure 3.6. As shown, the training loss, i.e., the mean squared error between predicted and actual CoM in the training phase, starts at a much lower point and converges better to the end point. Therefore, the model with transfer learning is far more capable in learning and converging towards a better solution. The performance evaluation of the bPTV is shown in Figure 3.8, with a linear fit of CT-based GTV versus the total BSF shown in supplementary materials (Pearson's r value of 0.8). bPTV estimation based on the

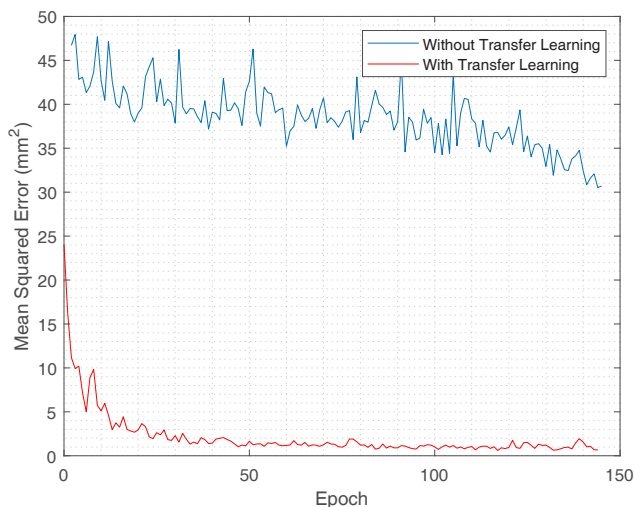


Figure 3.7 – Effect of transfer learning on the training process: Progression of training loss of the first 150 epochs for a network without transfer learning (blue) and the same network with transfer learning (red).

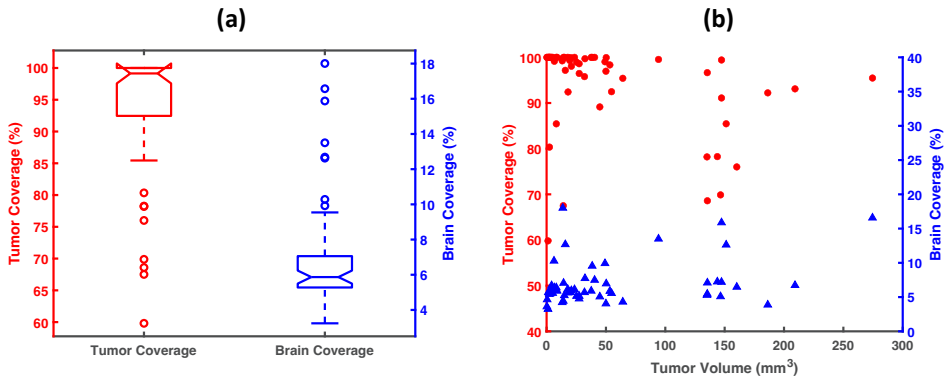


Figure 3.8 – Performance evaluation of tissue coverage: (a) boxplot of coverage of tumors (red) and normal tissue (blue) (b) effect of tumor volume on both tissue coverages

predicted CoM shows promising results. The proposed method averages more than 94 ± 9 % tumor coverage while keeping the mean healthy tissue coverage around 7 ± 3 %.

Finally, Figure 3.9 presents the visualization of the BLI-based tumor targeting as elaborated in this paper. As can be observed, the proposed method provides good overlap of the targeting volume with the tumor while sparing most of the healthy tissue.

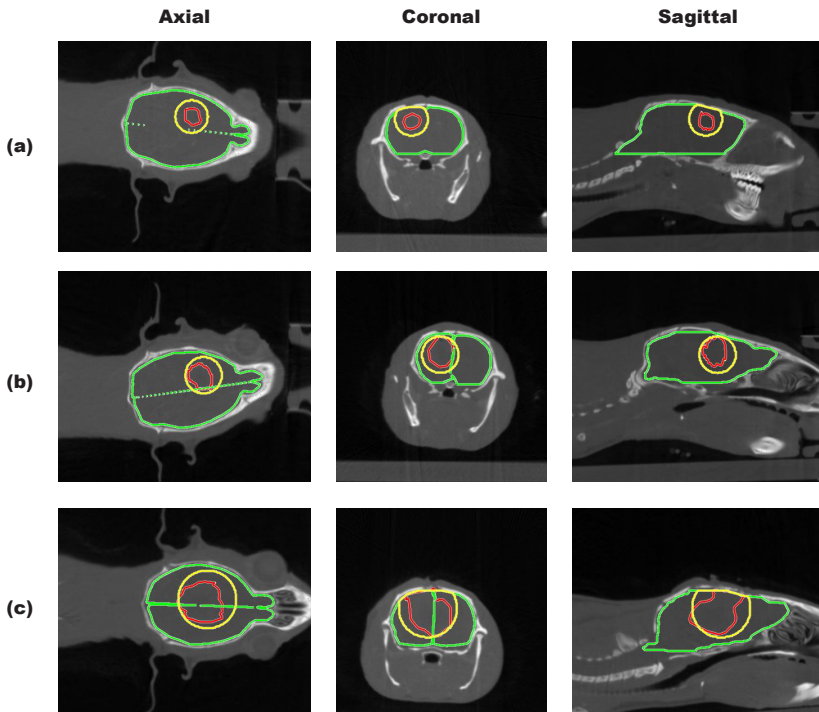


Figure 3.9 – visualizations of the output in three different animals (a-c) shown in different planes. Green, red, and yellow contours represent brain, tumor and predicted BLI-based targeting volume respectively.

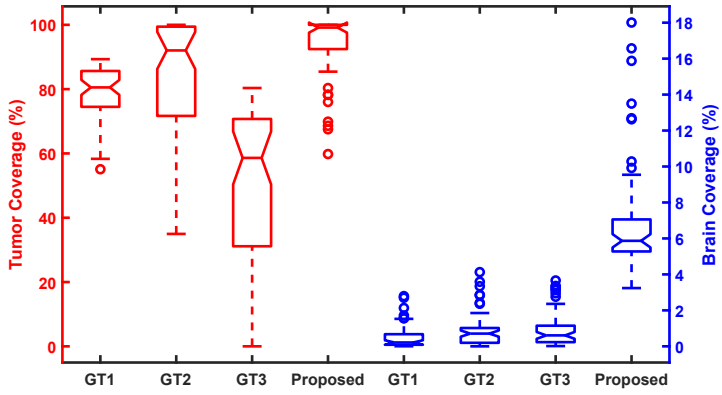


Figure 3.10 – The performance of the proposed method in four different scenarios: (GT1) both CoM and tumor volume are estimated ideally equal to the ground truth, (GT2) CoM is predicted accurately but volume is estimated according to the proposed framework, (GT3) volume estimation is accurate while CoM is predicted using the deep learning model, and the result of the proposed solution as presented in Figure 3.8.

Results of the uncertainty analysis of the proposed solution are presented in Figure 3.10. The first ground-truth case (GT1) targets only 79% of the tumor with maximum healthy tissue conservation, with an average brain coverage of 0.5%. In the second ideal case (GT2), both metrics on average increased to 84% and 0.9%. Finally, the third ideal scenario (GT3) resulted in a substantial decrease in the tumor coverage with an average of 49.3% while further increasing the average brain coverage to 1%.

Discussion

This paper proposed a deep CNN to predict the tumor's CoM based on BLI and estimate the treatment volume accordingly. Nearly all previously published methods rely on very complicated and approximative mathematical physics models of light propagation to predict light distribution within the biological tissue as a surrogate for tumor location. Solving these models needs various approximations and estimations, which can reduce the reconstruction accuracy. In contrast, AI algorithms can learn the best statistical model that can be fitted to the data. Although often slow during the training process, AI solutions can be fast during the inference phase. The proposed method achieves a runtime of milliseconds in the inference phase and it can thus contribute substantially to real-time targeting once translated to real BLI measurements. Furthermore, the proposed solution can predict the location of the tumor with sub-millimeter accuracy and construct a spherical target volume that captures, on average, more than 94% of the tumor while only including 7% of the brain volume, all of which provide an accurate BLI-based GBM targeting for rat models.

In this study, we only investigated the feasibility of using a CNN to improve the reconstruction accuracy of BLI determined volumes. The proposed method can achieve high accuracy in predicting tumor location and encompassing volume in the reference geometry. In the pre-training database, the accuracy of the position prediction is approximately equal to the CBCT imaging resolution used to create the inputs. However, training one model for each unique animal is a cumbersome task. Therefore, we explored transfer learning to solve this issue and extrapolate the learned knowledge to predict CoM in different animals. Figure 3.6 highlights the added value of transfer learning. Although we noticed a slight increase in the ΔCoM in the real-case database compared to the pre-training, the final result still provides sub-millimeter accuracy in most cases.

Since designing complex field shaping devices for small animal irradiation platforms is a very challenging task, all commercial units use static collimators with circular or rectangular shapes to irradiate the planned volume. Therefore, in this study, the BLI-based gross target volume was estimated using a sphere around the predicted CoM. As shown in Figure 3.7, the bPTV covers 94% of the tumor on average and spares most of the normal tissue around it. Therefore, the proposed algorithm can be used to provide bioluminescence-based targeting for a large variety of cases. However, in this paper, only simulated BSF and not camera-acquired BSF of real-case GBM bioluminescence acquisitions are used, as the first step towards developing a CNN-based method for BLI-based targeting. However, approximating the target volume as an enveloping sphere brings inherent error to the proposed solution, which is shown in Figure 3.10. In the best-case scenario, for which both CoM and the volume are known, employing the enveloping sphere approximation will reduce the tumor coverage score substantially. However, this effect can be mitigated by adding a margin to the spherical envelope. Furthermore, it has been confirmed that the volume estimation is overestimating the size of the tumor in most cases. However, the inaccuracy imposed by estimating tumors with their enveloping sphere, even in the best-case scenario, limits the overall accuracy of the model. In the future, more advanced AI models can be employed to enhance the proposed framework and enable full tumor shape prediction. In addition to the inherent limitations of the spherical estimation method used here, the uncertainties incorporated in CoM and volume predictions, as presented in Figure 3.10, contribute to increased brain coverage while reducing tumor coverage. However, the added margin compensates for such errors and provides an acceptable tumor coverage while keeping the brain coverage below 10%.

In reality, BSF cannot be measured directly and it should be reconstructed using a limited set of projections captured by the camera. This, in the best case, can only generate a partial indirect measurement of the actual BSF. In the future, the proposed framework of this paper will be adopted for real measurements and the accuracy of the model will be further

improved by adding more training samples to the database. The presented CNN-based framework can achieve deeper layers in limited memory compared to the fully connected multi-layered perceptron (MLP) counterpart implemented by Gao^[15]. Therefore, CNN-based models can extract and learn more features in the same amount of memory. In addition, Gao's model relies on registration between a standard mesh and the input mesh, which brings additional computational cost and uncertainty. Deng et al.^[17] present a CoM prediction algorithm with comparable accuracy to this paper's CNN-based framework. While both Deng's method and the method presented in this work are based on a combination of CoM and volume predictions to target tumors, Deng's method relies on mathematical models of light propagation and a measured unirradiated tumor growth curve. Comparison of the reported results, between the CNN-based and Deng's method, shows the superior performance of the CNN-based method. While Deng et al. achieved an average of 1 mm Δ CoM, the proposed CNN-based method can result in 0.6 mm Δ CoM on average. However, the observed improvement in the presented CNN-based method can be linked to the use of idealized cases, i.e., MC simulations, in this study. Nonetheless, a drawback of Deng's method is its dependence on the unirradiated tumor growth curve. Considering the purpose of BLI-based targeting, tumors will likely respond to the treatment which slows their growth and puts the reliability of tumor growth curve into question. Consequently, their proposed algorithm cannot be employed in fractionated radiation studies. The presented method, on the other hand, does not rely on the tumor growth curve and can be a useful tool in small animal GBM studies. The proposed CNN architecture imposes a limitation on the general use of the developed method. In other words, the predicted single-coordinate CoM limits the valueability of the proposed framework for metastatic tumors where two or more clusters of tumor cells or formed. However, the studied rat GBM model is not a metastatic tumor model and only forms a single compact tumor upon proper implantation. To address this limitation, in future works image-to-image transformer networks such as U-Net and autoencoders can be utilized. The findings of this paper should be extended and validated in in-phantom and in vivo animal studies. Thus longitudinal BLI imaging can replace longitudinal CE-CBCT imaging, delivering no imaging dose to the animals. Furthermore, the presented framework can be extended using more sophisticated deep learning models, such as generative adversarial networks (GANs), to obtain the BLI-based tumor contour. This would allow for even more accurate targeting and facilitates animal studies even further. In addition, continuous bioluminescence imaging in contrast to imaging at discrete angles might add value to the reconstruction algorithms. However, measurement noise due to hardware limitations might be a bottleneck in such an approach.

Conclusion

In this paper, we developed a framework using deep learning for bioluminescence-based targeting for GBM animal models. The proposed model can predict the tumor's CoM with submillimeter accuracy, except for tumors smaller than 10 mm³. In addition, we showed that the accuracy of the proposed planning scheme with circular encompassing fields is sufficient for targeting with a high average tumor coverage. Our findings can open the door to further investigation of AI-based approaches in the field of bioluminescence tomography. This paper's findings can help biologists investigate GBM using bioluminescence markers. CNN based BLI targeting may also reduce the planning time compared to physics model-based counterparts. However, this paper mainly focused on developing the framework based on Monte Carlo simulations to generate the necessary training database. Further studies are needed to extend the framework for real BLI measurements.

Acknowledgment

The authors would like to thank Dr. Brent van der Heyden for fruitful discussion. This work was partially supported by special research fund for double doctorate degree projects in the framework of the cooperation between Hasselt university and Maastricht UMC+ (Grant No. R-8216).

Ethical statement

μ CBCT images were re-used from previous animal experiments, which were all in accordance with local institutional guidelines for animal welfare and approved by the Animal Ethical Committee of Maastricht University (protocol number 2017-012).

References

- [1] F. Tillner, P. Thute, R. Bütof, M. Krause, and W. Enghardt, "Pre-clinical research in small animals using radiotherapy technology--a bidirectional translational approach," *Z. Med. Phys.*, vol. 24, no. 4, pp. 335–351, Dec. 2014, doi: 10.1016/j.zemedi.2014.07.004.
- [2] K. T. Butterworth, K. M. Prise, and F. Verhaegen, "Small animal image-guided radiotherapy: status, considerations and potential for translational impact," *Br. J. Radiol.*, vol. 88, no. 1045, p. 20140634, Jan. 2015, doi: 10.1259/bjr.20140634.
- [3] B. F. Koontz, F. Verhaegen, and D. De Ruyscher, "Tumour and normal tissue radiobiology in mouse models: how close are mice to mini-humans?," *Br. J. Radiol.*, vol. 90, no. 1069, p. 20160441, Jan. 2017, doi: 10.1259/bjr.20160441.
- [4] F. Verhaegen et al., "ESTRO ACROP: Technology for precision small animal radiotherapy research: Optimal use and challenges," *Radiother. Oncol.*, vol. 126, no. 3, pp. 471–478, Mar. 2018, doi: 10.1016/j.radonc.2017.11.016.
- [5] F. Verhaegen, P. Granton, and E. Tryggestad, "Small animal radiotherapy research platforms," *Phys. Med. Biol.*, vol. 56, no. 12, pp. R55-83, Jun. 2011, doi: 10.1088/0031-9155/56/12/R01.
- [6] S. Gutierrez, B. Descamps, and C. Vanhove, "MRI-Only Based Radiotherapy Treatment Planning for the Rat Brain on a Small Animal Radiation Research Platform (SARRP)," *PloS One*, vol. 10, no. 12, p. e0143821, 2015, doi: 10.1371/journal.pone.0143821.
- [7] T. D. Chiu, T. J. Arai, J. Campbell Iii, S. B. Jiang, R. P. Mason, and S. Stojadinovic, "MR-CBCT image-guided system for radiotherapy of orthotopic rat prostate tumors," *PloS One*, vol. 13, no. 5, p. e0198065, 2018, doi: 10.1371/journal.pone.0198065.
- [8] C. Vanhove and I. Goethals, "Magnetic resonance imaging-guided radiation therapy using animal models of glioblastoma," *Br. J. Radiol.*, vol. 92, no. 1095, p. 20180713, Mar. 2019, doi: 10.1259/bjr.20180713.
- [9] R. A. Weersink et al., "Integration of optical imaging with a small animal irradiator," *Med. Phys.*, vol. 41, no. 10, p. 102701, 2014, doi: 10.1118/1.4894730.
- [10] K. O'Neill, S. K. Lyons, W. M. Gallagher, K. M. Curran, and A. T. Byrne, "Bioluminescent imaging: a critical tool in pre-clinical oncology research," *J. Pathol.*, vol. 220, no. 3, pp. 317–327, Feb. 2010, doi: 10.1002/path.2656.
- [11] Jessica Kalra and Marcel B. Bally, "Bioluminescence Applications in Preclinical Oncology Research," in *Bioluminescence*, David Lapota, Ed., Rijeka: IntechOpen, 2012, p. Ch. 7. doi: 10.5772/36736.
- [12] A. J. Chaudhari et al., "Hyperspectral and multispectral bioluminescence optical tomography for small animal imaging," *Phys. Med. Biol.*, vol. 50, no. 23, pp. 5421–5441, Dec. 2005, doi: 10.1088/0031-9155/50/23/001.
- [13] S. Ahn, A. J. Chaudhari, F. Darvas, C. A. Bouman, and R. M. Leahy, "Fast iterative image reconstruction methods for fully 3D multispectral bioluminescence tomography," *Phys. Med. Biol.*, vol. 53, no. 14, p. 3921, Jul. 2008, doi: 10.1088/0031-9155/53/14/013.
- [14] B. Zhang et al., "Bioluminescence Tomography-Guided Radiation

- Therapy for Preclinical Research," *Int. J. Radiat. Oncol.*, vol. 94, no. 5, pp. 1144–1153, Apr. 2016, doi: 10.1016/j.ijrobp.2015.11.039.
- [15] Y. Gao, K. Wang, Y. An, S. Jiang, H. Meng, and J. Tian, "Nonmodel-based bioluminescence tomography using a machine-learning reconstruction strategy," *Optica*, vol. 5, no. 11, pp. 1451–1454, Nov. 2018, doi: 10.1364/OPTICA.5.001451.
- [16] B. Zhang, W. Yin, H. Liu, X. Cao, and H. Wang, "Bioluminescence tomography with structural information estimated via statistical mouse atlas registration," *Biomed. Opt. Express*, vol. 9, no. 8, pp. 3544–3558, Jul. 2018, doi: 10.1364/BOE.9.003544.
- [17] Z. Deng et al., "In vivo Bioluminescence Tomography Center of Mass-Guided Conformal Irradiation," *Int. J. Radiat. Oncol. Biol. Phys.*, vol. 106, no. 3, pp. 612–620, Mar. 2020, doi: 10.1016/j.ijrobp.2019.11.003.
- [18] S. Ren, L. Wang, Q. Zeng, D. Chen, X. Chen, and J. Liang, "Effective reconstruction of bioluminescence tomography based on GPU-accelerated inverse Monte Carlo method," *AIP Adv.*, vol. 10, no. 10, p. 105329, Oct. 2020, doi: 10.1063/5.0027207.
- [19] L. Vandewinckele et al., "Overview of artificial intelligence-based applications in radiotherapy: Recommendations for implementation and quality assurance," *Radiother. Oncol. J. Eur. Soc. Ther. Radiol. Oncol.*, vol. 153, pp. 55–66, Dec. 2020, doi: 10.1016/j.radonc.2020.09.008.
- [20] V. Cuplov, I. Buvat, F. Pain, and S. Jan, "Extension of the GATE Monte-Carlo simulation package to model bioluminescence and fluorescence imaging," *J. Biomed. Opt.*, vol. 19, no. 2, p. 026004, Feb. 2014, doi: 10.1117/1.JBO.19.2.026004.
- [21] A. M. Mowday et al., "Use of a Luciferase-Expressing Orthotopic Rat Brain Tumor Model to Optimize a Targeted Irradiation Strategy for Efficacy Testing with Temozolomide," *Cancers*, vol. 12, no. 6, Art. no. 6, Jun. 2020, doi: 10.3390/cancers12061585.
- [22] A. Vaniqui, L. E. J. R. Schyns, I. P. Almeida, B. van der Heyden, S. J. van Hoof, and F. Verhaegen, "The impact of dual energy CT imaging on dose calculations for pre-clinical studies," *Radiat. Oncol.*, vol. 12, no. 1, p. 181, Nov. 2017, doi: 10.1186/s13014-017-0922-9.
- [23] M. Mesradi et al., "Experimental and analytical comparative study of optical coefficient of fresh and frozen rat tissues," *J. Biomed. Opt.*, vol. 18, no. 11, p. 117010, Nov. 2013, doi: 10.1117/1.JBO.18.11.117010.
- [24] H. Soleimanzad, H. Gurden, and F. Pain, "Optical properties of mice skull bone in the 455- to 705-nm range," *J. Biomed. Opt.*, vol. 22, no. 1, p. 10503, Jan. 2017, doi: 10.1117/1.JBO.22.1.010503.
- [25] H. Zhao, T. C. Doyle, O. Coquoz, F. Kalish, B. W. Rice, and C. H. Contag, "Emission spectra of bioluminescent reporters and interaction with mammalian tissue determine the sensitivity of detection in vivo," *J. Biomed. Opt.*, vol. 10, no. 4, p. 41210, Aug. 2005, doi: 10.1117/1.2032388.
- [26] S. J. Pan and Q. Yang, "A Survey on Transfer Learning," *IEEE Trans. Knowl. Data Eng.*, vol. 22, no. 10, pp. 1345–1359, Oct. 2010, doi: 10.1109/TKDE.2009.191.
- [27] M. Romero, Y. Interian, T. Solberg, and G. Valdes, "Targeted transfer learning to improve performance in small medical physics datasets," *Med. Phys.*, vol. 47, no. 12, pp. 6246–6256, Dec. 2020, doi: 10.1002/mp.14507.

- [28] A. Vaniqui, B. van der Heyden, I. P. Almeida, L. E. Schyns, S. J. van Hoof, and F. Verhaegen, "On the determination of planning target margins due to motion for mice lung tumours using a four-dimensional MOBY phantom," *Br. J. Radiol.*, vol. 92, no. 1095, p. 20180445, Mar. 2019, doi: 10.1259/bjr.20180445.

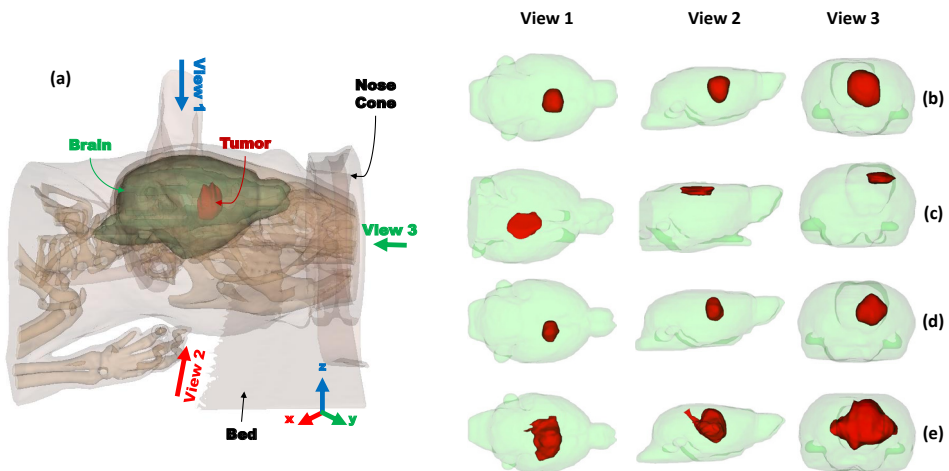
Supplementary Material

A- F98 Database

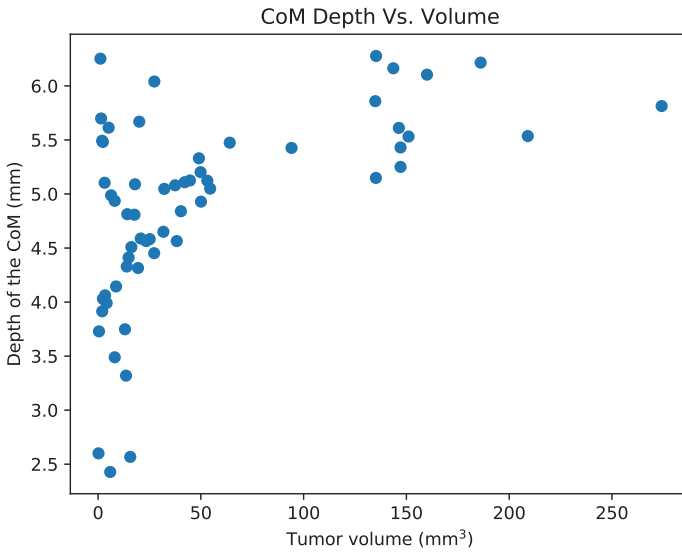
The main data used in this study was obtained from a previous study, namely the F98 database, as described in Mowday et al, Cancers 2020. This database contains a number of glioblastoma (GBM) rat models imaged at different time points, resulting in 57 original cases in total. A total number of 20,000 initial luciferase-enabled GBM cells are implanted at a certain location inside the brain. In this study, we used the CE-CBCT images together with the hand-delineated brain and tumor contours from this database. Supplementary Figure 1 shows some examples from this database showing the range of variation in tumor size, shape and depth. The Euclidian distance between the tumor's center of mass (CoM) and the nearest air voxel is reported as the CoM depth in the Supplementary Figure 2. As can be observed, the tumors can have a range of depths inside the brain which makes the reconstruction task more challenging.

B- Tumor Augmentation for pre-training database

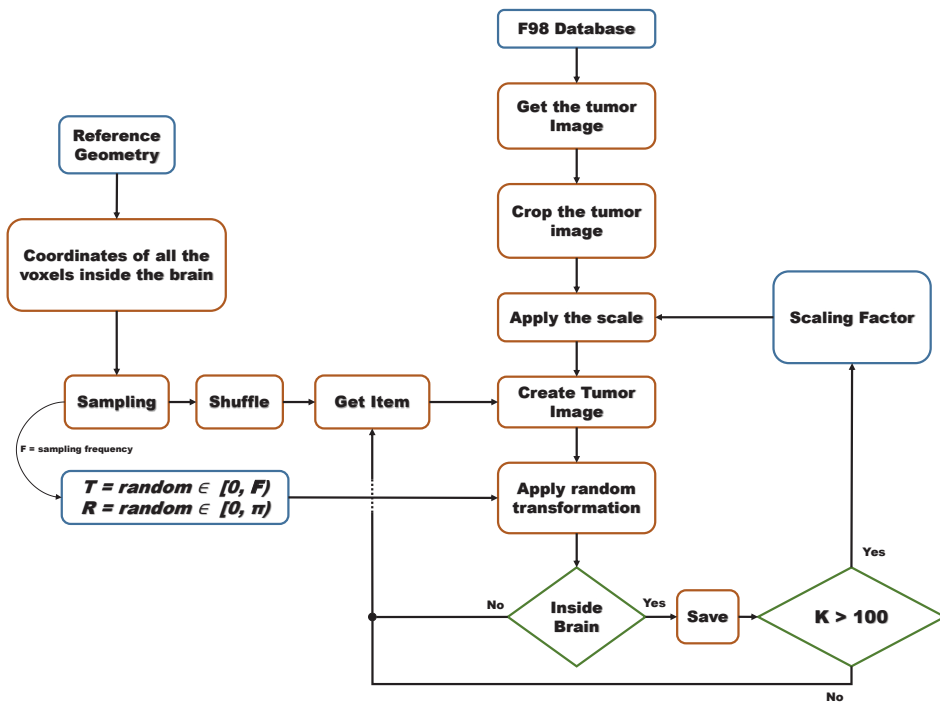
In this paper, a novel algorithm was developed to expand the variations inside the F98 database for building a pre-training database. This algorithm, as shown in Supplementary Figure 3, relies on the F98 database as the starting point. Once the tumor images are extracted from this database, they are cropped to include only the smallest region containing the tumor. The produced 3D masks are then scaled up or down according to a set of 10 randomly generated scaling factors. For each scale in the scaling set, a maximum of 100 random cases of tumor



Supplementary Figure 1 – A sample of tumor shape variations and location in 3D: (a) 3D visualization of a sample image from the F98 database with the tumor shown as red, (b-e) different 3D views of different samples in the database showing the variations in shape, size and location (depth) of the tumor



Supplementary Figure 2 – Tumor depth variations as a function of the tumor volume: CoM depth feature is computed as the Euclidian distance between the tumor’s CoM and the closest air voxel

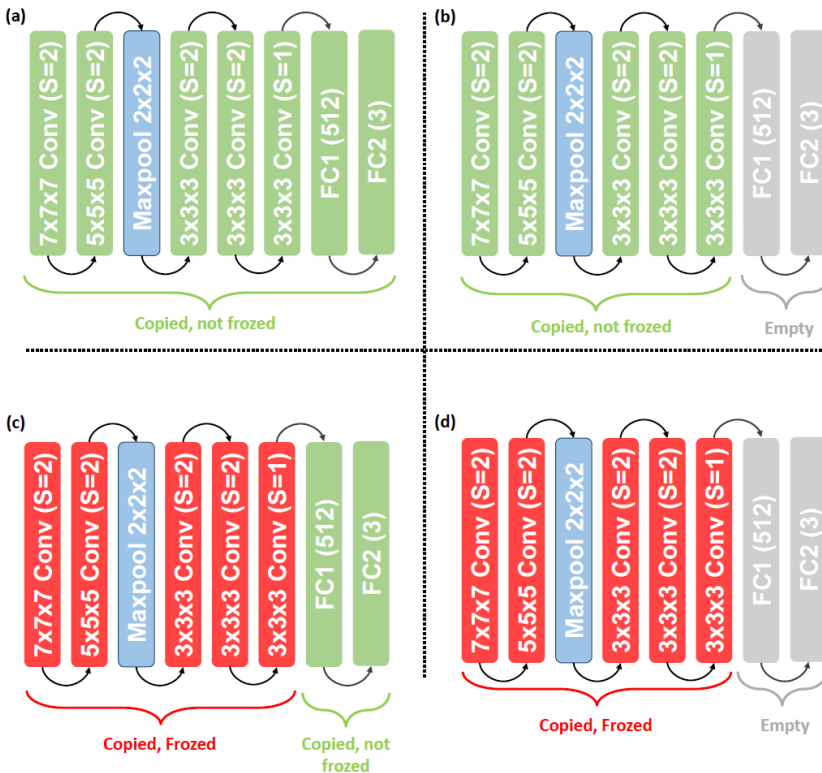


Supplementary Figure 3 – The tumor augmentation algorithm used for building the pre-training database

images are then created with different placement in the brain, resulting in a maximum of 1000 tumor images per initial tumor image obtained from F98 database.

In order to randomly distribute the scaled tumor masks in the brain, voxels inside the brain in the reference geometry are sampled in three dimensions and listed inside a vector. These coordinates are considered as the center of the tumor in a binary mask with the same size as the reference geometry, hence allowing the tumor to be placed in any random position in the brain. Therefore, a random coordinate from this list is selected for each iteration and a tumor mask is created accordingly. Then, a random rigid-body transformation consisting of 3D random translation and rotation is applied to the tumor mask to account for the sampling frequency and to add more variations to the shapes. Finally, the resulted tumor mask is checked to make sure the entire tumor is located inside the brain and, if true, save the output. Once the tumor images are obtained, a simple code is used to find all the super-voxels inside the tumor and summing up the output of the corresponding Monte Carlo simulations.

3

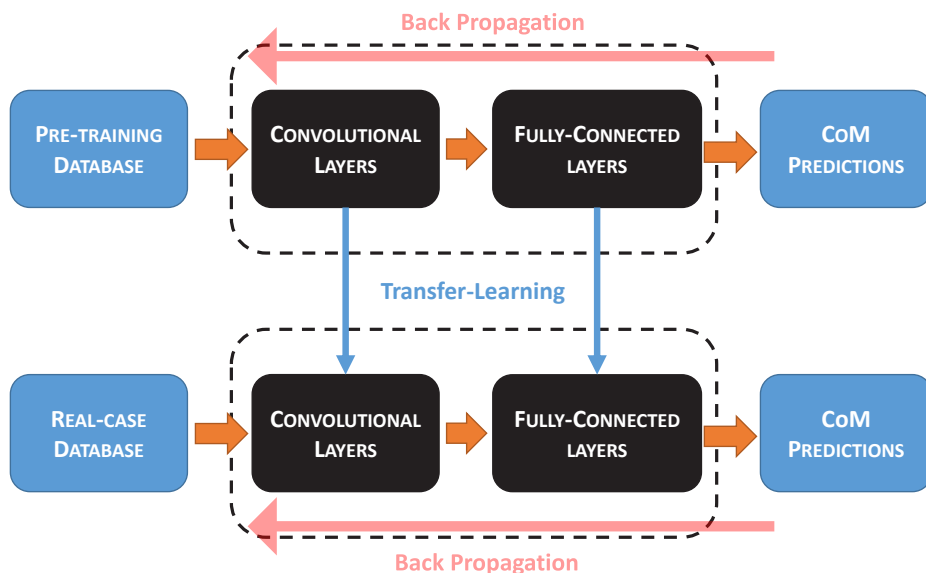


Supplementary Figure 4 – Different schemes to apply transfer-learning: (a) all the layers are copied and trained on the new model (b) Only the first few or all the convolutional layers are copied and trained (c) All the layers are copied but only the fully connected (FC) layers are trained (d) Only the first few or all the convolutional layers copied and not trained on the new model

C- Transfer learning

Bioluminescence tomography (BLT) reconstruction problem is highly ill-posed, and it is very common to use additional a-priori information to solve this problem. In this paper, a-priori information is fed into the convolutional neural network in the format of transfer-learning, meaning that first a network is trained on a large-sized database containing variations of tumors inside a unique rat geometry, namely the source task. Once the model is trained and can predict CoM in the source task, the acquired knowledge is transferred to a new network for the target task. Transferring the knowledge into this new network is performed by copying learned parameters to an identical otherwise empty model. This process, known as transfer-learning, can be done in different schemes, as shown in Supplementary Figure 4.

In this paper, copying all the weights and training all the copied layers, as shown in Supplementary Figure 4 (a), yielded the best results. This can be due to the similarity between the source and target task causing the trained network on the pre-training database to be a good initial point for the real-case database. Supplementary Figure 5 shows the transfer-learning process as used in this paper.

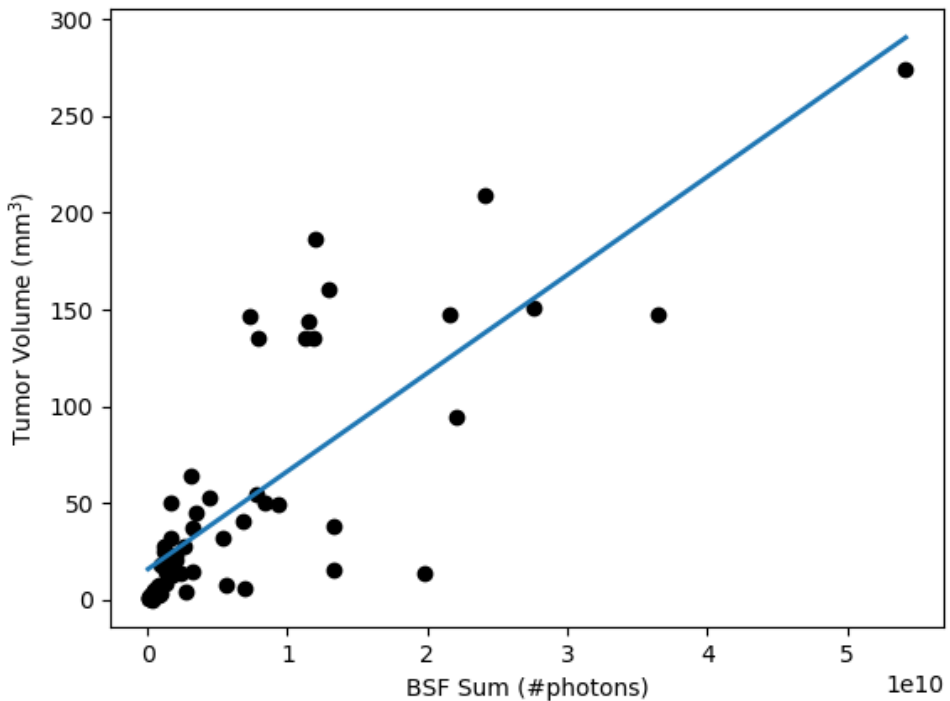


Supplementary Figure 5 – Transfer-learning process used in this paper: first the 3D CNN model is trained on the pre-training database and then all the learned parameters are transferred and fine-tuned in new identical model

D- Bioluminescence-based tumor volume estimation

Tumor volume is estimated using a linear fit between the total number of photons emerging from the skin in the Monte Carlo simulations and the CE-CBCT based gross tumor volume (cGTV), as shown in Supplementary Figure 6. The Monte Carlo simulations used in this figure are extracted from the real-case database, hence include the photon absorption.

3



Supplementary Figure 6 - Linear fit used for bioluminescence-based volume estimation: x-axis is the integral of the BSF (overall detected photons) and the y-axis is the CE-CBCT based tumor volume

Chapter 4

A deep-learning assisted bioluminescence tomography method to enable radiation targeting in rat glioblastoma

Authors

Behzad Rezaeifar, Cecile J.A. Wolfs, Natasja G. Lieuwes, Rianne Biemans, Brigitte Reniers, Ludwig J. Dubois, Frank Verhaegen.

Adopted From

Phys. Med. Biol. (2023) doi:10.1088/1361-6560/ace308.

Abstract

Objective: A novel solution is required for accurate 3D Bioluminescence Tomography (BLT) based glioblastoma (GBM) targeting. The provided solution is computationally efficient to support real-time treatment planning, thus reducing the X-ray imaging dose imposed by high-resolution micro cone-beam CT.

Approach: A novel deep learning approach is developed to enable BLT-based tumor targeting and treatment planning for orthotopic rat GBM models. The proposed framework is trained and validated on a set of realistic Monte Carlo simulations. Finally, the trained deep learning model is tested on a limited set of BLI measurements of real rat GBM models.

Significance: Bioluminescence Imaging (BLI) is a 2D non-invasive optical imaging modality geared toward pre-clinical cancer research. It can be used to monitor tumor growth in small animal tumor models effectively and without radiation burden. However, the current state-of-the-art does not allow accurate radiation treatment planning using BLI, hence limiting BLI's value in pre-clinical radiobiology research.

Results: The proposed solution can achieve sub-millimeter targeting accuracy on the simulated dataset, with a median dice similarity coefficient (DSC) of 61%. The provided BLT-based planning volume achieves a median encapsulation of more than 97% of the tumor while keeping the median geometrical brain coverage below 4.2%. For the real BLI measurements, the proposed solution provided median geometrical tumor coverage of 95% and a median DSC of 42%. Dose planning using a dedicated small animal treatment planning system indicated good BLT-based treatment planning accuracy compared to ground-truth CT-based planning, where dose-volume metrics for the tumor fall within the limit of agreement for more than 95% of cases.

Conclusion: The combination of flexibility, accuracy, and speed of the deep learning solutions make them a viable option for the BLT reconstruction problem and can provide BLT-based tumor targeting for the rat GBM models.

1. Introduction

In the past decades, image-guided small animal precision irradiation systems have found their way into the pre-clinical cancer research^{[1, [2]}. These systems mainly use micro cone-beam computed tomography (μ CBCT) as their primary image guidance and allow clinically relevant conformal irradiation for small animals. However, to visualize small tumors with high spatial resolution, it is often necessary to increase the X-ray imaging dose in these systems. In general, a voxel size of approximately 100 μ m is required to visualize the anatomical structures of rats or mice. Achieving such a high resolution usually imposes high imaging X-ray doses in the range of 10-100 cGy to the animal^{[3, [4]}. Native μ CBCT images, without the use of contrast media, result in poor imaging contrast, especially for pre-clinical glioblastoma (GBM). Hence, contrast-enhanced CBCT (CE-CBCT) is often employed to improve tumor visualization^{[5]-[7]}. The accumulated X-ray imaging radiation dose limits the number of imaging sessions within a longitudinal study and therefore hinders effective pre-clinical research.

Bioluminescence imaging (BLI) has been introduced as an alternative to other functional imaging modalities, such as Positron Emission Tomography (PET). BLI allows functional tumor imaging without any radiation burden for the animal. In addition, it often constitutes a cheaper functional imaging solution without any background noise. Hence, recently BLI has become a very attractive imaging modality for small animal pre-clinical cancer research.

However, at the time of this publication, most commercially available systems do not fully utilize BLI-based targeting and irradiation possibilities^[8]. This is mainly due to the lack of 3D information based on 2D bioluminescence images. Many groups, including ours, have tried various solutions to tackle the bioluminescence tomography (BLT) reconstruction problem^{[9]-[12]}.

In contrast to other mathematically-driven solutions^{[9]-[11], [13]}, our efforts have mainly been focused on deep learning (DL) based solutions. Previously, we proposed a 3D Convolutional Neural Network (CNN) to predict the tumor's center of mass (CoM) and to construct a spherical volume around the CoM as the targeting volume^[12]. Although the CoM-based method provides an effective solution to enable DL-assisted BLI-based tumor targeting in pre-clinical practice, it has several shortcomings due to its simplified spherical targeting geometry. In this paper, a novel artificial intelligence (AI) based algorithm is developed to predict the 3D shape and location of the tumor for rat GBM models. The proposed solution relies on a 3D ResNet architecture adopted from the RatLesNet model, originally developed by Valverde et al., 2020 for lesion detection in rodent Magnetic Resonance Images (MRI). Furthermore, the proposed solution employs Monte Carlo simulations (MCS) to provide a realistic training database for the DL model as an alternative to a large set of

acquired images. The performance of the trained model is then evaluated on the MCS database and a smaller set of real measured BLI using a variety of objective quality metrics, such as dice similarity coefficient, geometrical convergence metrics, and dose-volume metrics.

2. Materials and Methods

2.1. Problem Formulation

To solve the BLT reconstruction problem, an accurate model of optical light propagation in the biological tissue is needed. The diffusion approximation (DA) of the radiative transport equation is the most commonly used forward model in the literature. Following the notation used by^[15], the DA is expressed as:

$$-\nabla \cdot (D(\mathbf{r}) \nabla \Phi(\mathbf{r})) + \mu_a(\mathbf{r}) \Phi(\mathbf{r}) = S(\mathbf{r}) \quad (\mathbf{r} \in \Omega) \quad (1)$$

Where D is the optical diffusion coefficient depending on the 3D position $\mathbf{r} \in \mathbb{R}^3$ inside the region of interest Ω , Φ represents the photon density (Watt/mm²) and S denotes the power density of the internally located light source (Watt/mm³). Furthermore, the optical diffusion coefficient is defined as $D(\mathbf{r}) = 1/3(\mu'_s(\mathbf{r}) + \mu_a(\mathbf{r}))$, where μ_a and μ'_s are the absorption and reduced scattering coefficients (mm⁻¹).

The DA equation is solved using the following Robin boundary condition:

$$\Phi(\mathbf{r}) + 2A(\mathbf{r}; n, n') D(\mathbf{r}) (\mathbf{v}(\mathbf{r}) \cdot \nabla \Phi(\mathbf{r})) = 0 \quad (\mathbf{r} \in \partial\Omega). \quad (2)$$

Where $A(\mathbf{r}; n, n')$ represent the boundary mismatch resulting from the two different refractive indexes at the boundary, and \mathbf{v} is the unit outer normal at the boundary ∂ .

$$\mathbf{M}\Phi = \mathbf{F}S \quad (3)$$

Where \mathbf{M} and \mathbf{F} are positive system matrices resulting from FEM. Equation (3) can be rewritten as:

$$\Phi = \mathbf{M}^{-1} \mathbf{F}S = \mathbf{A}S \quad (4)$$

Most mathematically derived approaches then define a cost function with a specific regularization term and attempt to locate the optimal light source by minimizing this cost function. In this paper, however, following the same notation, the BLT reconstruction inverse problem can be expressed as:

$$\mathbf{S} = \mathcal{F}^{-1}(\Phi) \quad (5)$$

In equation (5), \mathcal{F}^{-1} is a non-linear function that links the measured photon flux to the corresponding source, resulting from the solution to the inverse problem.

It has been proven that the BLT reconstruction problem is highly ill-posed^[16]. Often various prior information or regularization methods are utilized to decrease the ill-posedness of the problem. In this paper, a DL model is used to directly learn a novel solution for S based on the best fit to the observations.

Following the notation of E et al., 2020, the output of a multi-layered DL model can be expressed as:

$$Y = \mathcal{G}(x) = \sum_{i_L=0}^{m_L} w_{i_L}^L \mathcal{H} \left(\sum_{i_{L-1}=0}^{m_{L-1}} w_{i_{L-1}}^{L-1} \mathcal{H} \left(\dots \mathcal{H} \left(\sum_{i_1=0}^{m_1} w_{i_1}^1 \mathcal{H} \left(\sum_{i_0=0}^{m_0} w_{i_0}^0 x_{i_0} \right) \right) \right) \right) \quad (6)$$

Where $w_{i_{k+1}i_k}^k$ with $k \in [0, L]$ are the weights of the network in different layers. Furthermore, x_{i_0} indicates the input of the DL model, i.e. bioluminescence surface photon count. The activation function \mathcal{H} is an arbitrary non-linear function that gives the DL model further degrees of freedom in modeling non-linear phenomena. In this notation, the bias term in each layer is generalized as a weight.

DL models can be considered as universal function approximators and thus if the DL model is designed and trained properly, it can learn a mathematical model \mathcal{G} , in equation (6), that best fits the provided data and, in theory, can be an estimation for \mathcal{F}^{-1} in equation (5). Figure 4.1 depicts the overview of the DL-based proposed framework in this paper to solve the BLT inverse problem.

2.2. Monte Carlo Simulations

MCS is considered the gold standard for photon transport simulations and can provide more accurate ground-truth data for the AI model than other analytical model counterparts. Therefore, due to the lack of a considerable amount of ground-truth labeled BLI measurements (which is a common problem in biological experiments), a larger database of MCS is generated and utilized to train and validate the AI model.

To build the MC database representative of the real GBM BLI measurements, a database of CE-CBCT images of real GBM is employed. This database, hereinafter called the F98 database, consists of 57 cases with CE-CBCT images of an orthotopic F98 rat GBM animal model, imaged at several time points in our previous work^[5]. Each of the cases within the F98 database further includes hand-delineated contours for normal brain and tumor tissue by a trained biologist. In addition to these contours, two separate thresholds are applied to the mass density image, obtained from the original CE-CBCT, to generate bone and air masks. The resulting contours are combined to create the MCS geometry, as shown in Figure 4.2 and explained in our previous publication^[12] in more detail. The hand-delineated tumor contour is then used to constitute a uniformly and

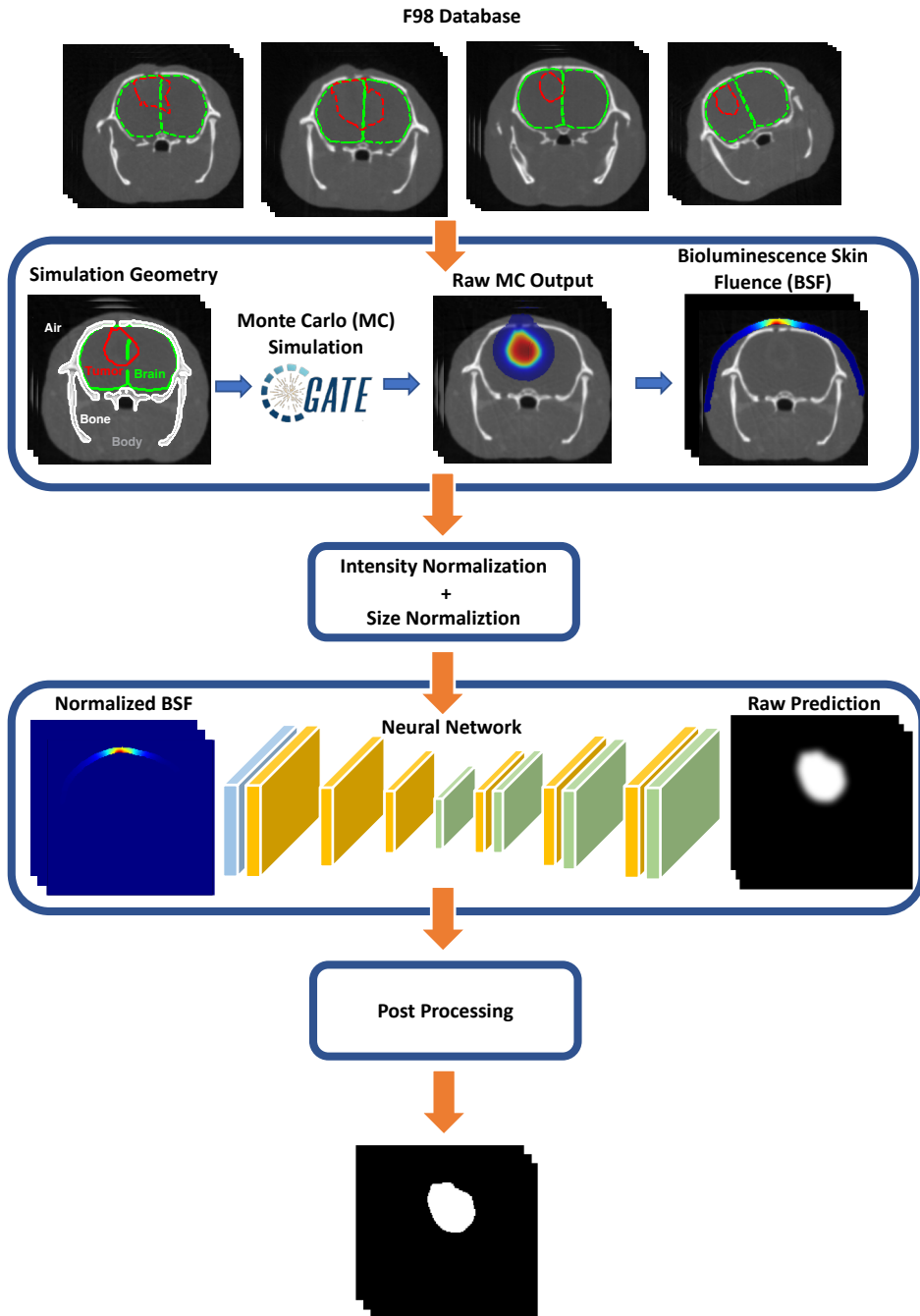


Figure 4.1 – Overview of the proposed DL-based framework for the BLT reconstruction problem: the raw Monte Carlo (MC) output and bioluminescence skin fluence (BSF) overlaid on top of the CT scan in the second box just for visualization.

isotropically-emitting light source with a similar light emission spectrum to the firefly luciferase light emerging from the tumor. In other words, in this study, substructures within the tumor, such as necrotic and hypoxic regions, are ignored. Therefore, the uniformly emitting tumor approximates the real emission of the bioluminescence-enabled tumor. The simulation geometry and the light-emitting source are presented to the MCS engine, namely the Geant4 Application for Tomographic Emission (GATE)^[18]. In this study, various wavelength-dependent optical properties are assigned to each tissue in the MCS geometry. These properties included a tissue-dependent absorption and scattering coefficient, presented in Figure 3 of our previous work^[12], which was obtained from previous work^{[19]–[21]}. Furthermore, two simplifications are included in the MCS: (a) tumor tissue has the same optical properties as the brain tissue, and (b) everything other than the brain, air, skull, and the tumor is considered water since its contribution to the simulation output is negligible. The water regions account for the small regions in the medial longitudinal fissure, the space between the brain and the skull, and the rest of the soft tissue in the head and neck region. As shown in Figure 4.2, the aforementioned water-equivalent region is either filled with cerebrospinal fluid, which has similar optical properties to water or located far from the relevant scoring region of interest, which causes its optical properties to be insignificant.

The MCS output is scored using the GATE fluence actor which tracks photons entering or exiting a specified geometry. In a voxelized geometry, such as the one used in this study, the fluence actor registers the photons passing through each individual voxel and saves them as a raw 3D image volume. Furthermore, the constant number of emitted photons per unit volume, i.e. voxels inside the tumor volume, is set to

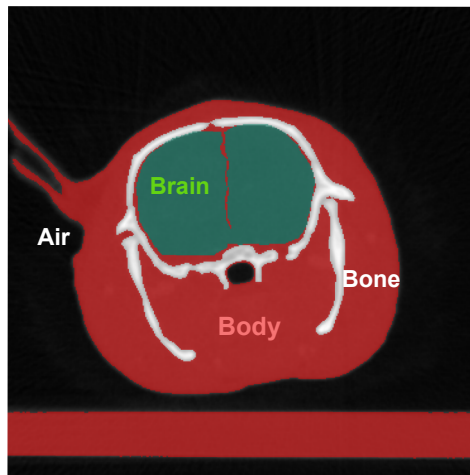


Figure 4.2 – Different Materials in the MCS: the brain optical properties are extracted from^[19], The skull optical properties from^[20]. Everything other than that, i.e. body and air, are assigned to water and air.

provide an average statistical simulation uncertainty below 0.2% for an average-sized tumor.

2.3. Deep Learning Solution

2.3.1. Pre-Processing of the MCS Output

Two main pre-processing steps are considered to create the training database from the MCS output: (a) converting the raw 3D MCS output to the 3D bioluminescence skin fluence (BSF) by applying the corresponding skin mask and (b) normalizing the BSF data.

As mentioned previously, raw MCS output includes the resulting photon count at every voxel in the voxelized geometry. To consider only the MCS output for voxels visible to the camera, and thus creating the subsequent BSF, a skin mask is constituted based on the original CT scan and the location of a hypothetical camera. This is done by a three-step process: (a) obtaining an air mask from the original CT image by using a constant HU threshold, (b) computing an approximate skin contour by applying morphological operators to the air mask and (c) removing any unwanted voxels that are not visible to the camera such as voxels located in the inner part of ears using a simplified ray-tracing algorithm. The location of a hypothetical rotating camera used in this study corresponds to the commercially available small animal irradiating platform (X-RAD 225Cx, Precision X-ray Inc., North Branford, CT, USA). Furthermore, a set of five camera viewing angles is considered, based on real animal experiments, to obtain the visible skin voxels. Details of the algorithm used for computing the skin mask can be found in supplementary materials, sub-section S1.

Once the BSF is obtained for every case in the MCS database, the volumetric images are normalized in both intensity and size. Intensity normalization is performed by normalizing the volumetric images to have a median of zero and a standard deviation of one. In addition to the intensity normalizers, all the volumetric images in the database are moved to a fixed input grid of 375 x 450 x 375 voxels, by padding or cropping the original input, to have equal image dimensions required by the DL algorithm. Thereafter, all the samples in the database are down-scaled to a smaller 250 x 300 x 250 volume to minimize the GPU memory needed for training.

2.3.2. Training and Validation of the AI Model

In this study, a previously developed fully convolutional neural network architecture, namely RatLesNet^[14], is employed to solve the BLT reconstruction problem. The RatLesNet model was originally developed to segment small brain lesions in rodent magnetic resonance images (MRI). Therefore, it is a suitable candidate for the BLT reconstruction problem since the final aim of the current study is also the segmentation of small tumors from 3D BSF images. Furthermore, an automatic hyperparameter optimization algorithm (Optuna)^[22] is used to obtain

the best set of hyperparameters by solving an optimization problem that samples hyperparameters from a pre-defined search space using the tree-structured Parzen estimator algorithm^[23]. The hyperparameters included in the search space consist of the number of filters in convolutional layers, loss function, and the optimization algorithm. Hence, the original architecture of the RatLesNet is kept intact. More details on the hyperparameter optimization and the search space for each hyperparameter are shown in supplementary materials, supplementary table 1.

An exclusion criterion based on the tumor volume is defined removing tumors smaller than 10 mm³, reducing the total number of MCS samples to 42 cases. This is due to the fact that such a small tumor: (a) requires collimated beams smaller than 3 mm for targeting, which will increase the dose delivery uncertainty, (b) emits fewer bioluminescence photons, and (c) cause additional challenges for the DL model due to high level of class imbalance in the prediction image.

Once the exclusion criteria are applied and the optimal set of hyperparameters is obtained, the remaining MCS database is shuffled randomly and divided into different subsets for training, validation, and test. A 9-fold cross-validation algorithm is used to train, validate and test the model on all the cases in the database. In other words, as shown in Figure 4.3, for each fold five cases (12% of total samples) are reserved for testing and five more for validation. The rest of the samples are used to train the model. During the training phase, one DL model is trained for each fold using the training and validation set, keeping the test set

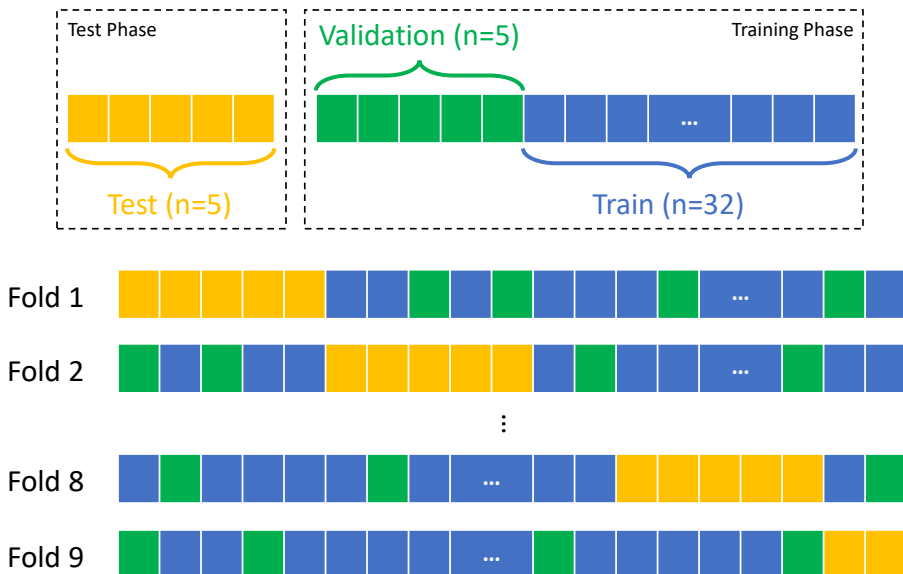


Figure 4.3 – Graphical representation of the 9-fold cross-validation method used in this study: In each fold (other than the last one) five samples are reserved for test and the rest are shuffled into five validation and 32 training samples.

unobserved. This results in nine distinct trained models for each fold and allows the model to be tested on all 42 cases using the corresponding fold in which the specific case is in the test database.

2.4. Robustness Evaluation Using Synthetic Cases

A set of 42 cases is artificially generated to evaluate the robustness of the proposed deep learning solution for cases outside the initial training distribution and quantify the performance gain upon retraining the network with newly added samples. The synthetic case database includes randomly augmented tumor shapes inside randomly selected rat MCS geometry, placed in either (a) a random location in the brain or (b) near the center of mass of the original tumor with respect to the selected MCS geometry. These two categories of synthetic cases are further complemented with cases where the original tumor for the selected MCS geometry is either replaced by (c) the predicted tumor by the proposed deep learning solution for the same case or (d) one of the two flat tumors in the F98 database. Therefore, each of the categories represents a true out-of-distribution (OOD) scenario. For example, category (a) represents cases where differently shaped tumors are implanted in anatomical locations far from the standard implantation site in the F98 database. In contrast, categories (b) and (c) represent cases where new variations of tumor shapes are located around the same implantation site.

Once the MCS geometry for the synthetic cases is obtained, a fast MCS is performed for each case with fewer photons per unit volume of tumors. This also enables the investigation of the model's sensitivity with respect to the statistical noise in the MCS output. Thereafter, the same pre-processing steps, introduced previously, are applied, and a new synthetic case database is generated. The synthetic case database is then utilized in two scenarios: (a) as the test data for the network trained with original F98 cases to establish robustness against new cases, and (b) added to the training data to obtain the performance gain when the model observes such OOD cases. For scenario (a), where the synthetic cases are used as test data without further training, all nine models obtained from the 9-fold cross-validation are utilized, and the final prediction is considered as the result of the majority voting of all models.

2.5. Geometrical Evaluation

To quantify the model's absolute performance, the BLT problem is considered analogous to the auto-contouring problem^[24]. This is possible by converting the raw prediction output of the AI model for the location of the photon source to a binary mask using a pre-defined constant threshold. Hence, segmentation quality evaluation metrics, consisting of ΔCoM , dice similarity coefficient (DSC), and a set of geometrical coverage scores are used to evaluate this aspect of the solution.

DSC is defined as the ratio of the overlapping region between the two contours, the ground-truth tumor and the predicted BLT source, and the overall volume covered by both contours:

$$DSC = \frac{2TP}{2TP + FN + FP}$$

Where TP (True Positive) is the overlap region between the ground-truth tumor contour and the predicted BLT source, FP (False Positive) is the part of the predicted BLT source which is not in the ground truth, and FN (False Negative) is the missing part of the ground truth in the BLT predictions. ΔCoM , on the other hand, quantitatively measures the Euclidean distance between the centers of mass of the predicted BLT source and the ground-truth tumor contour.

The output of the RatLesNet is the binary 3D BLT source prediction and can be considered as the BLI-based gross tumor volume (bGTV). In this paper, a 3D uniform margin is added to the bGTV to construct the BLI-based planning target volume (bPTV). The size of the added margin is optimized using the MCS database. More details are provided in supplementary material, section S3. Furthermore, healthy brain tissue is computed by subtracting the CT-based gross tumor volume (cGTV) from the brain contour used in the MCS.

Thereafter, geometrical coverage scores for corresponding tissues are computed as the percentage of tissue that falls within the bPTV with respect to the total volume of the tissue:

$$C_{\text{tissue}} = \frac{\text{volume} (bPTV \cap \text{tissue})}{\text{volume} (\text{tissue})} \times 100$$

Therefore, the ideal results will be $C_{\text{tumor}} = 100\%$ and $C_{\text{brain}} = 0\%$, meaning that the predicted BLT-based planning volume includes all the tumor tissue while not targeting any normal brain tissue. However, in practice, this is not feasible with external radiation beams traversing the brain and often the added margin will impose normal tissue coverage intentionally to avoid tumor recurrence.

2.6. BLT-based irradiation planning evaluation

Another important aspect of the BLI-based tumor predictions is the evaluation of irradiation planning with photon beams. Therefore, a set of dose metrics are used to evaluate the BLI-based tumor irradiation, including dose-volume metrics (DVM) and dose-volume histograms (DVH) for each tissue. Here, in order to avoid uncertainties in margin selection in small animal radiotherapy, conformal radiation treatment delivery plans are made based on the cGTV or on the bGTV by two independent observers using the small animal radiotherapy treatment planning software (SmART-ATP version 2.0, SmART Scientific Solutions B.V., Maastricht, Netherlands). In other words, no additional margin, other than the imposed margin by choosing a circular collimator, chosen from a real set of available collimators with diameters of 1, 3, 5, 8, and

10 mm, is considered for the treatment plans.

In routine pre-clinical practice, the objectives of the study determine the configuration of the beams in a case-dependent manner. Therefore, biologists have to select proper beam configurations per case. However, to normalize the beam configuration in this study, treatment plans are limited to two anterior/posterior parallel opposed beams with the isocenter located at the center of the target volume. This beam configuration is chosen based on the work of Mowday et al., 2020, proving it to have the highest healthy tissue sparing effect. In each case, as shown in Figure 4.4, the isocenter and width of two parallel-opposed circular-collimated beams are selected based on the ground truth cGTV or on the result of the proposed method, i.e. bGTV.

Photon dose calculations were done using the DOSXYZnrc Monte Carlo transport code (National Research Council Canada) within SmART-ATP with a constant statistical dose uncertainty of 5% to the target volume. The plans used 225 kVp X-rays (0.3mm Cu filter) and were made to deliver 20 Gy to the isocenter located at the center of the target volume in the brain.

Once the treatment planning is completed, a set of DVM is computed for each case. These metrics include: (a) mean dose (D_{mean}), and (b) dose to 95% (D_{95}) of the CT-delineated tumor and dose to 5% (D_5) of the brain tissue. DVM for all the cases in the MCS database are presented in scatter plots, allowing quantitative comparison between the reference CT-based plan and the resulting BLI-based plan. In addition to DVM, for a handful of representative cases, the DVH is also presented.

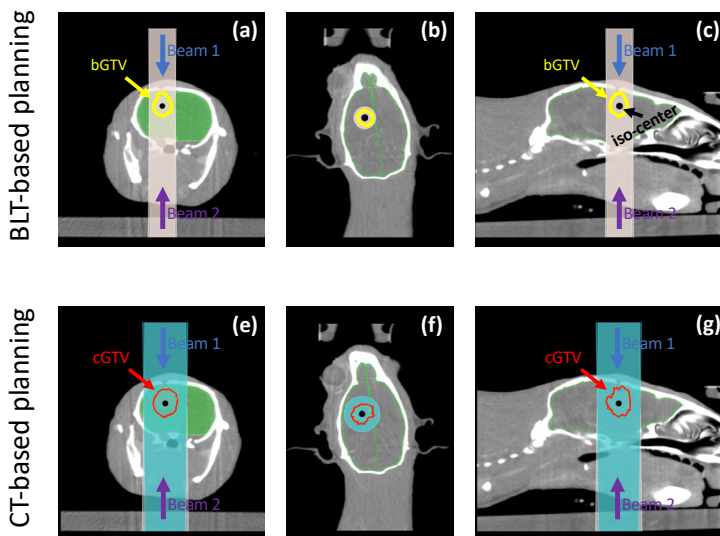


Figure 4.4 – Treatment planning visualization using two anterior/posterior parallel opposed circular beams around specific isocenter: in (a-c) the isocenter is located in the center of the BLI-based tumor prediction (bGTV) while (e-g) depicts the CT-based tumor (cGTV) and its associated planning. In both cases, doses are scored at the brain, cGTV and bGTV.

2.7. Case Study: Real BLI Measurements

To underline the performance of the novel method, developed using MC simulations, on real BLI measurements, a set of 5 real BLI measurements from two animals are used. The 2D BLI readings are obtained using the small animal radiotherapy unit equipped with a highly sensitive optical camera (iXon Ultra 897, Andor Technology Ltd., Belfast, United Kingdom). Although the optical system is fitted with a filter wheel enabling multispectral readings, the measurements used in this study are obtained using the open-filter option capturing the full spectrum of bioluminescence emission. In addition to the tested cases, numerous BLI-CT pairs have been acquired previously. However, the aforementioned data is not included in this study since the animals were taken out of the cabinet in between the two scans and are prone to displacement errors. Following the same implantation procedure explained previously^[5], a total of 20,000 firefly luciferase-positive GBM tumor cells are slowly injected into the brain. At each time point within the study, the animals are injected with both contrast-enhanced agents for CT (60 mg/kg Omnipaque, GE Healthcare, Eindhoven, Netherlands) and D-luciferin for BLI (150 mg/kg, Perkin Elmer, Rotterdam, Netherlands), according to the same protocol. Thereafter, animals are placed under isoflurane anesthesia and consecutive CBCT and BLI scans of the skull are obtained without moving or relocating the animal. 2D BLI projections are acquired at five angles (0° , $\pm 30^\circ$, and $\pm 60^\circ$) with 60 seconds exposure time and an electrical gain of 5. Thereafter, the 2D projections are processed using the provided software (Pilot, version 1.18.5.2, Precision X-Ray, Inc.) to obtain the 3D bioluminescence skin fluence^[25]. The output of the BLI is therefore saved as a 3D surface mesh where the BSF is expressed as an attribute for each node, which then is converted to a 3D volumetric image on the fixed grid, used for DL model training, by triangulation of the mesh. The resulting 3D BSF image is dilated by a $3 \times 3 \times 3$ structure element to increase the thickness of the skin and further resemble the MC simulations.

The 3D BSF image for each of the five real cases is fed into the DL algorithm and the output prediction is compared to the ground truth tumor mask provided by hand-delineating 3D CE-CBCT for the corresponding case. The real BSF images are considered out-of-database samples for all the folds. Hence, allowing all different models trained as part of the k-fold cross-validation method to be used, thus providing 9 different predictions per case. Furthermore, the final output for the real BSF image results from majority voting on all different predictions, enabling a more accurate result.

The prediction accuracy is then evaluated using DSC and ΔCoM , as explained in section 2.4. Furthermore, the BLI-based planning quality is scored both using the DVM and DVH from SmART-ATP.

3. Results

3.1. Prediction evaluation on Monte Carlo simulations

Figure 4.5 includes the two segmentation quality metrics, namely ΔCoM and DSC. As shown in Figure 4.5(a-b) and further visualized in Figure 4.7, the network prediction provides a good agreement with the ground truth with a median ΔCoM and DSC of 0.61 mm and 61%, respectively. Furthermore, the DL algorithm, on average, predicted a contour with ΔCoM of 0.69 ± 0.47 mm and DSC of 59 ± 17 %. Therefore, the proposed DL framework can infer the light source, i.e. tumor segmentation, from the surface photon count with sub-millimeter accuracy.

Figure 4.6 (a-b) represents the effect of the added margin on the geometrical coverage scores. As can be seen, with only 0.8 mm of uniform margin, the median tumor coverage score increases to more than 97% while keeping the geometrical brain coverage below 5%. Therefore, 0.8 mm of uniformly added margin is considered as the optimal margin and the resulting geometrical coverage scores are depicted in detail in Figure 4.6 (c-d). As can be seen, the proposed solution on the median can achieve 97.4% geometrical tumor coverage and 4.2% geometrical brain coverage, considering a 0.8 mm of uniformly added margin.

In this study, two of the samples within the database were extremely flat tumors seated near the edges of the brain along the ventral-dorsal axis, as depicted with blue squares in Figure 4.5 and visualized in Figure 4.7(d,e). Such flat tumors were misclassified as deeper implanted tumors beneath the ground truth volume.

The resulting BLI-based treatment planning for representative MCS cases is presented in Figure 4.7. As shown, the provided BLI-based treatment planning is identical to the CT-based treatment planning in cases with high DSC (Figure 4.7a). For cases with a median DSC, two

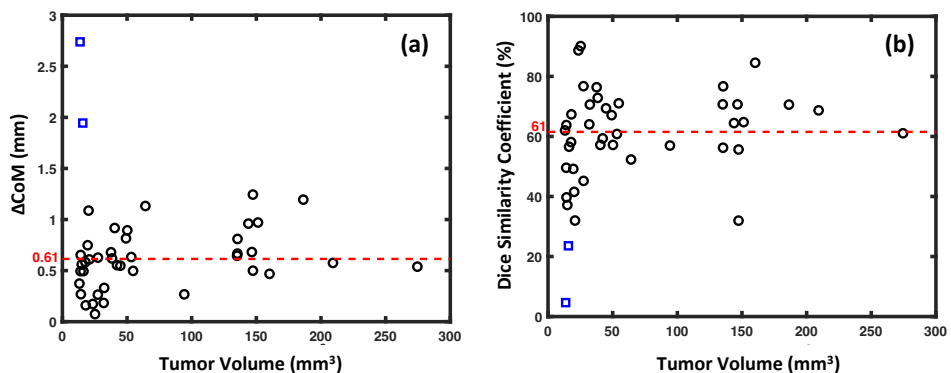


Figure 4.5 – Performance evaluation of the proposed method on Monte Carlo simulated database: (a) the ΔCoM evaluation metric and (b) DSC between the ground truth CT-based tumor and predicted BLI-based contour. The red dashed line shows the median value and two blue squares in each figure represent the two samples with extremely flat tumors which have been confused by the network for a deeper, more spherical tumor, displayed in Figure 4.7

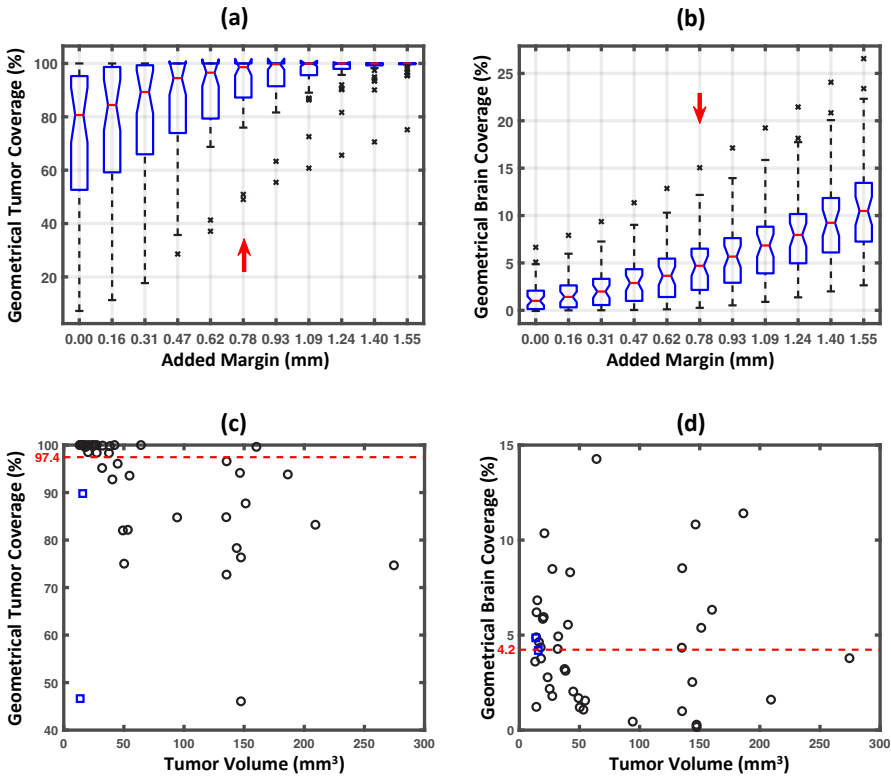


Figure 4.6 – Geometrical coverage evaluation of the proposed solution: (a-b) depicts the optimization of the geometrical uniform margin, and (c-d) visualizes the resulting geometrical tumor and brain coverage with 0.8 mm added margin. The red arrow in (a-b) presents the selected margin, and the crosses illustrate outliers. The red dashed line in (c-d) shows the median value and two blue squares in each figure represent the two samples with extremely flat tumors.

different scenarios were observed: Figure 4.7b represents cases where the predicted bGTV is slightly bigger than the ground-truth cGTV and Figure 4.7c is a case with median dice where the prediction is slightly smaller than the cGTV. As can be seen in the DVH plot for these cases, both result in good BLI-based planning. Figure 4.7b resulted in full dose coverage for the tumor but a slight increase in the healthy tissue, which is still acceptable. Figure 4.7c, on the other hand, caused a reduced healthy tissue dose with the cost of slightly less tumor coverage. Finally, for the cases with the lowest DSC, i.e. the two flat tumors, the parallel opposed anterior-posterior treatment planning provides an acceptable plan compared to the CT-based planning (Figure 4.7d,e) since the placement of the predicted bGTV is directly beneath the actual tumor in the axial plane.

Figure 4.8 shows the resulting DVM for the tumor and brain tissues. Since there is a considerable variation in tumor sizes within the MCS database, different collimator sizes were needed to target the respective volumes in each planning, ranging from 3mm up to 10 mm circular beams. In most

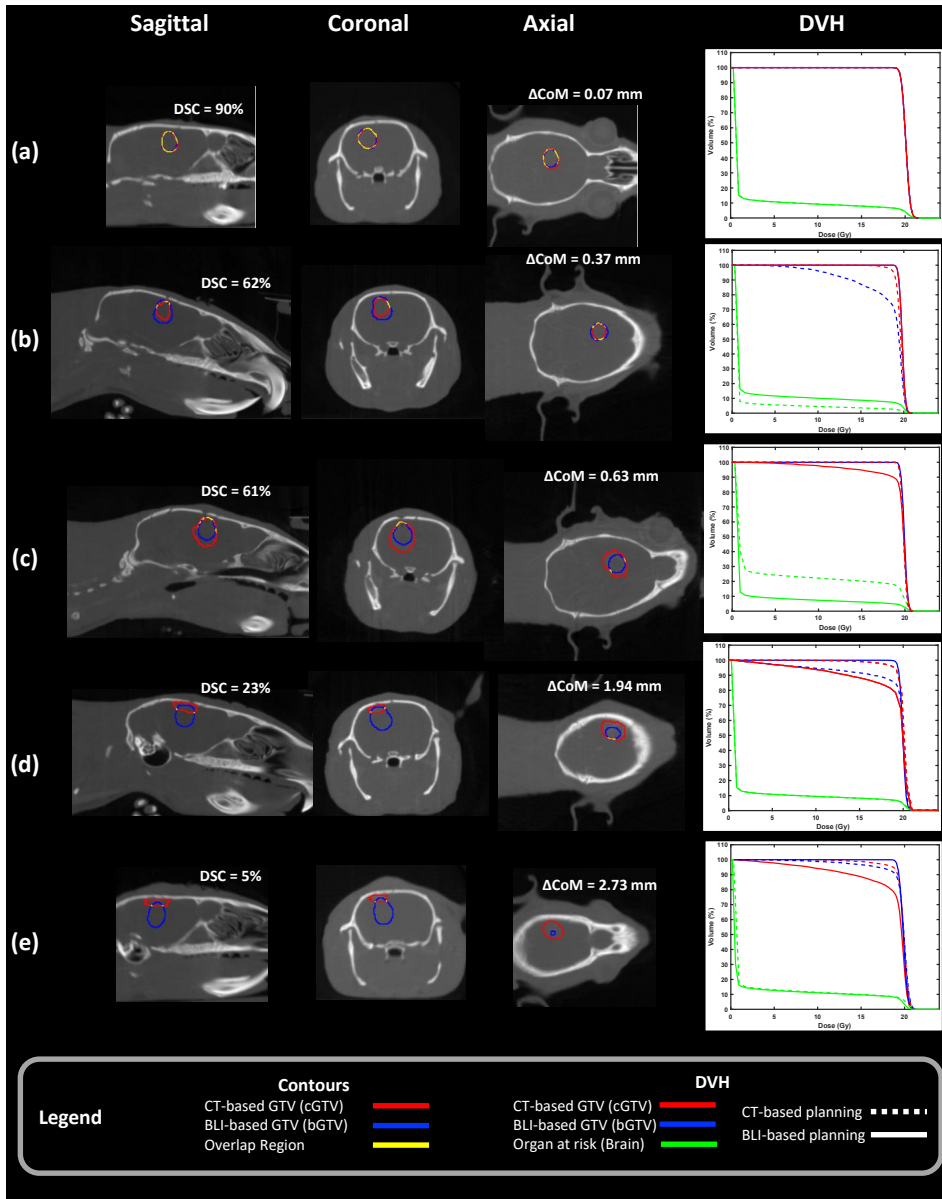


Figure 4.7 – Visualization of the network prediction and the resulting dose planning in selected cases: (a) is the best DSC, (b,c) represent cases with average DSC, and (d,e) depict the worst cases

cases (shown with circles in Figure 4.8), the circular collimator used for BLI-based and CT-based plans are of the same sizes, which underlines the similarity in the volume of cGTV and bGTV. Nevertheless, 25% of the database (shown with triangles in Figure 4.8) resulted in a larger BLI-based collimator than the CT-based collimator, because bGTV was larger than cGTV. There were 22.5% of the total cases for which the bGTV was smaller than the cGTV and resulted in a smaller collimator, shown in Figure 4.8 with squares.

DSC, on the other hand, has a less descriptive role in the treatment planning outcome with regard to the DVM for the tumor and brain. As can be seen in Figure 4.8, some cases with average to high DSC scores did not provide the prescribed mean dose to the tumor, either due to a smaller collimator or a larger ΔCoM error. On the contrary, a number of cases with low DSC provided the prescribed mean dose to the tumor but at the expense of a higher mean dose to the brain tissue.

3.2. Robustness Evaluation

The robustness of the proposed solution is measured against artificially generated samples with additional variations outside the training database. As shown in Figure 4.9, the proposed solution provides less

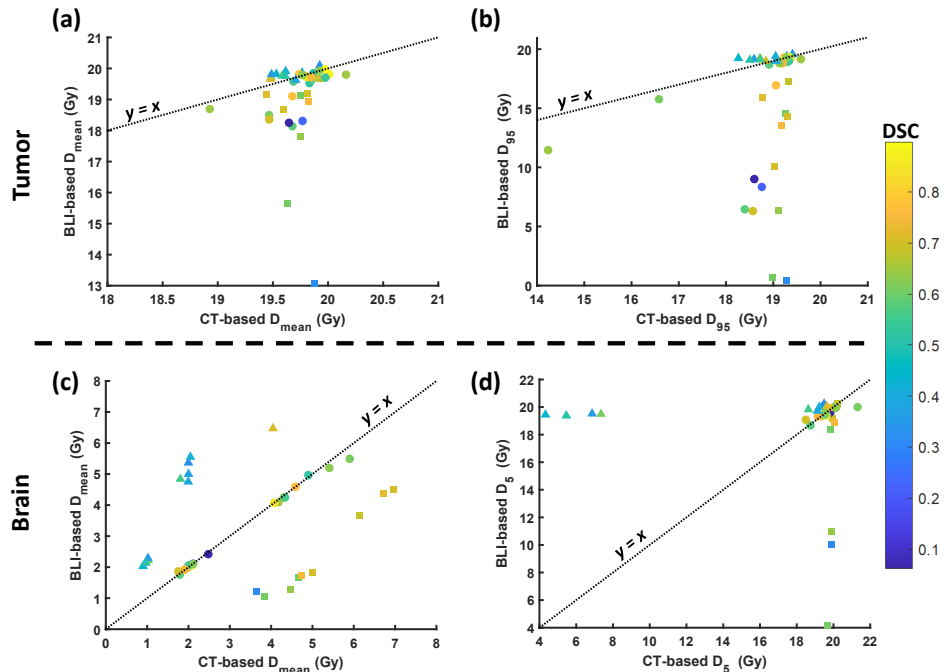


Figure 4.8 – Scatter plot for the DVM of tumor (a,b) and brain (c,d) in the MCS database. The DSC is shown as color for individual cases according to the color bar on the right. The differences in collimator sizes are shown as different markers for each case: circles, triangles, and squares are representative of cases where BLI-based collimator is equal, larger, and smaller than the CT-based collimator. A magnified version of the figure can be found in supplementary materials S4.

accurate predictions for out-of-distribution samples, i.e. samples with additional variations than those inside the training database. Categories (d) and (a), namely flat and randomly located tumors, constitute the worst performance with a median DSC of 24% and 30%, respectively. However, both categories also advantage from the highest performance gain upon training, with a median DSC of 37% and 42%. The Category (b) cases, new tumor shapes in the proximity of the original CoM, yield a median DSC of 46% before training and 53% after training. Furthermore, the performance of Category (c) remained almost constant, with a median DSC of 68% in both scenarios. Finally, the original MCS database, which was utilized in training without the new synthetic cases and provided a median DSC of 61%, demonstrated a reduction in performance upon the new training and provided a median DSC of 55%.

3.3. Case study: real BLI measurement

The performance evaluation of the proposed method on five different real BLI measurements is summarized in Figure 4.10(a-b). As shown in this figure, the overall performance of the proposed method is slightly reduced when applying it to the real BLI measurements, with a median DSC of 42.4 ± 14.8 percent and ΔCoM of 1.6 ± 0.4 mm. Furthermore, the coverage metrics for the real BLI measurements are visualized in Figure 4.10(c-d), underlining the agreement between the predicted BLT source and the ground truth tumor mask, with a median geometrical tumor coverage of 95.1 ± 11.2 % and geometrical brain coverage of 7.5 ± 2.0 %.

The visualizations of the predictions are shown in Figure 4.11 for the real BLI acquisitions underlining the agreement between the predictions and the ground-truth tumor mask. As can be seen, in three of the total

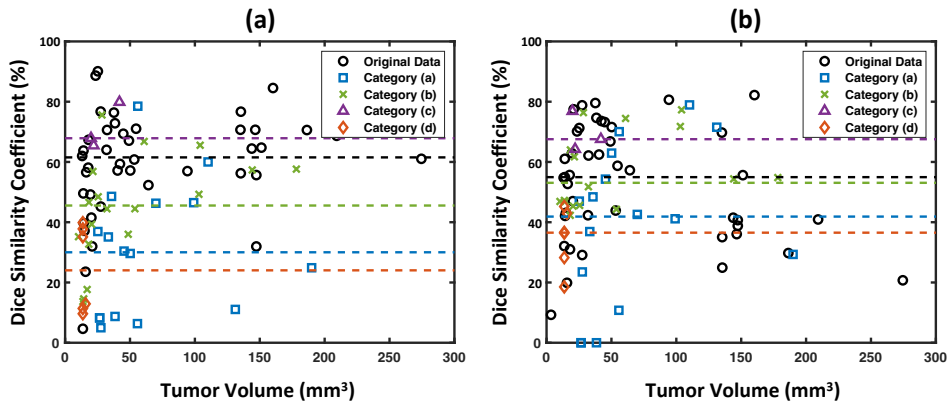


Figure 4.9 – Robustness analysis of the proposed solution with respect to out-of-distribution samples: (a) performance without additional training (b) improvements after training with new data. Different markers are used for various categories within the database: Categories (a) and (b) are respectively augmented tumor shapes at random locations and near the original location. Category (c) is the predicted tumor and category (d) is new flat tumors. Colored dashed lines represent the corresponding median for each category.

five cases, BLI-based treatment planning provides identical results to CT-based planning. For the other two cases, however, the dose to the tumor is slightly decreased when using BLI images, which can be compensated by considering a margin around the BLI-based tumor prediction.

The DVM for the real BLI acquisitions are presented in Figure 4.12. As shown, the proposed DL-based framework provides good planning accuracy compared to ground-truth CT-based planning. Four of the five cases resulted in nearly perfect agreement with the CT-based plans and only one of the cases (shown in Figure 4.11a) predicted a bigger BLI-based volume which necessitated use of a larger collimator.

4. Discussion

In this study, a novel deep learning approach is developed to enable BLI-based irradiation planning for the GBM orthotopic rat models. The proposed framework is a good candidate to facilitate BLI-based planning for other kinds of tumor models, both in rats and mice, providing small-animal image-guided radiotherapy without excess X-ray imaging dose

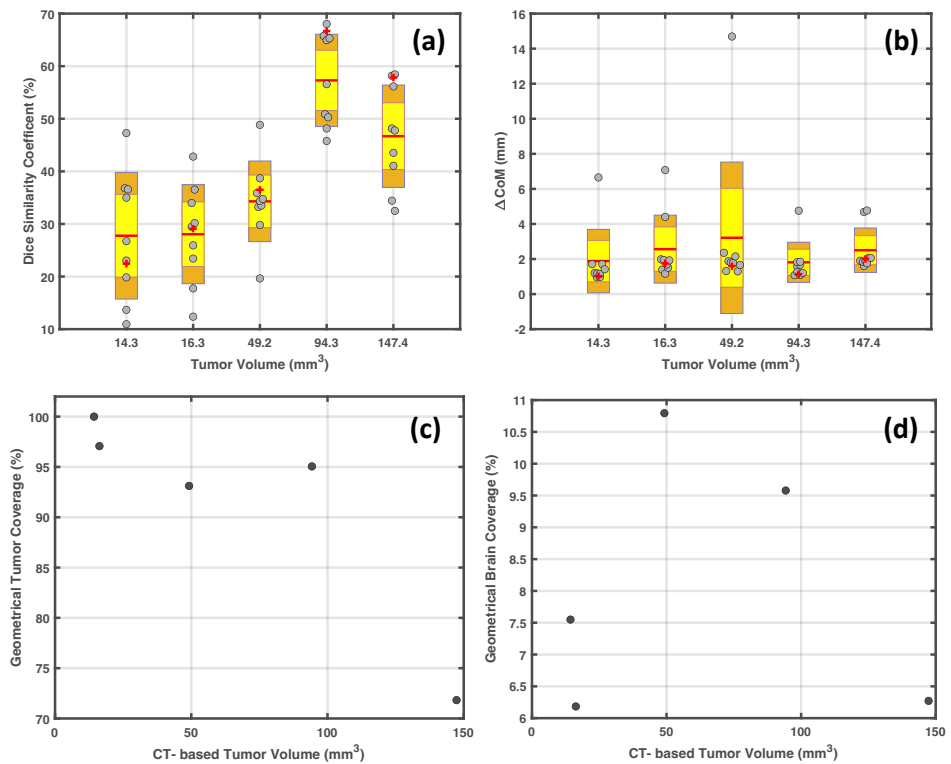


Figure 4.10 – Performance Evaluation on 5 real BLI measurements of Glioblastoma rat models using an X-RAD 225Cx irradiator: (a-b) segmentation quality metrics per sample and k-fold model and the aggregated prediction by majority voting shown as a red “+” marker (c-d) tumor and brain coverage of the aggregated predicted BLT source plus 0.7mm margin.

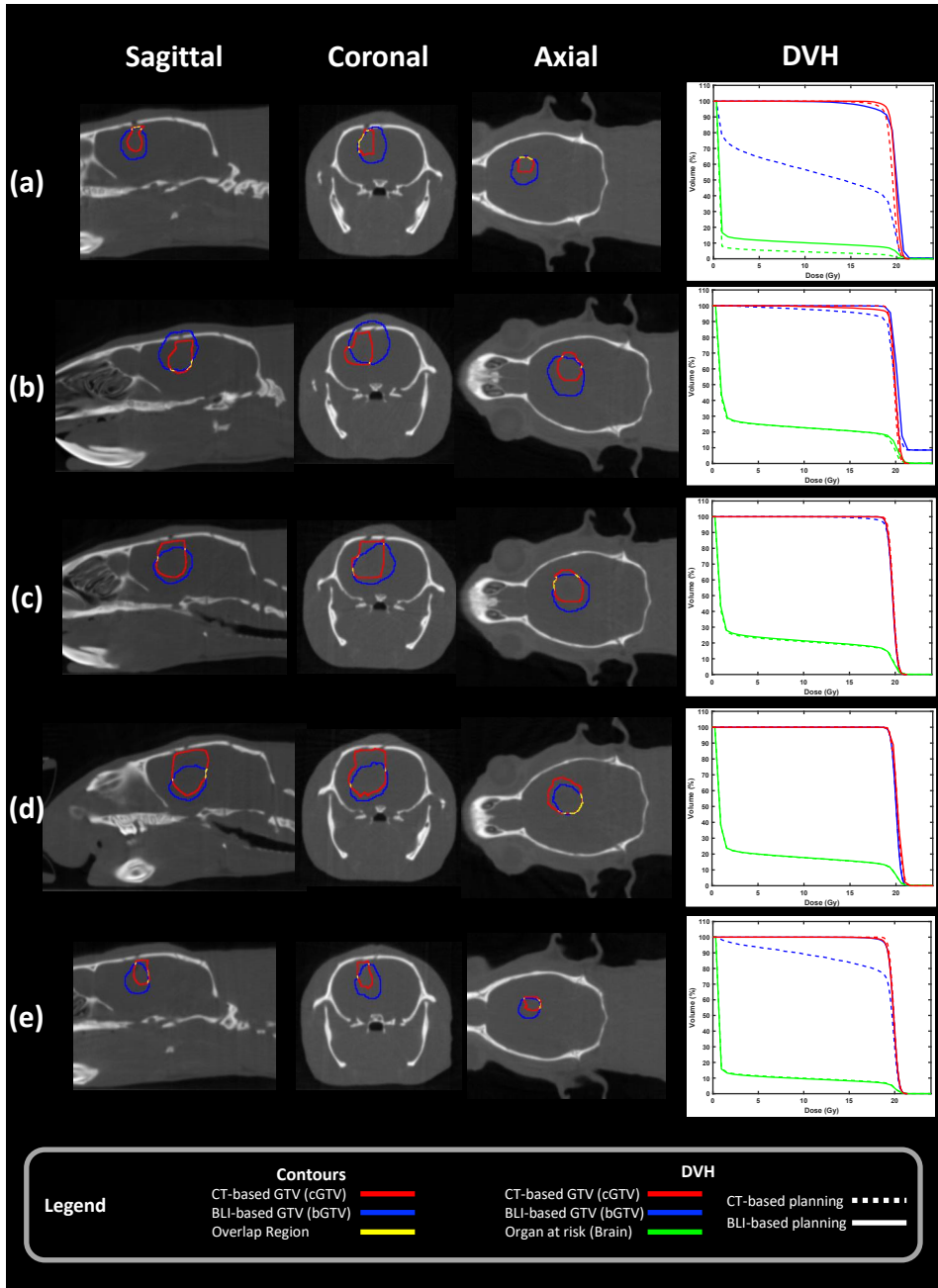


Figure 4.11 – Visualization of the aggregate predicted BLT source using real BLI measurement without added margin: red contour is the ground-truth cGTV, hand-delineated from CE-CBCT, and yellow is the predicted bGTV from the BLI data. DVH plot is the resulting planning for each contour.

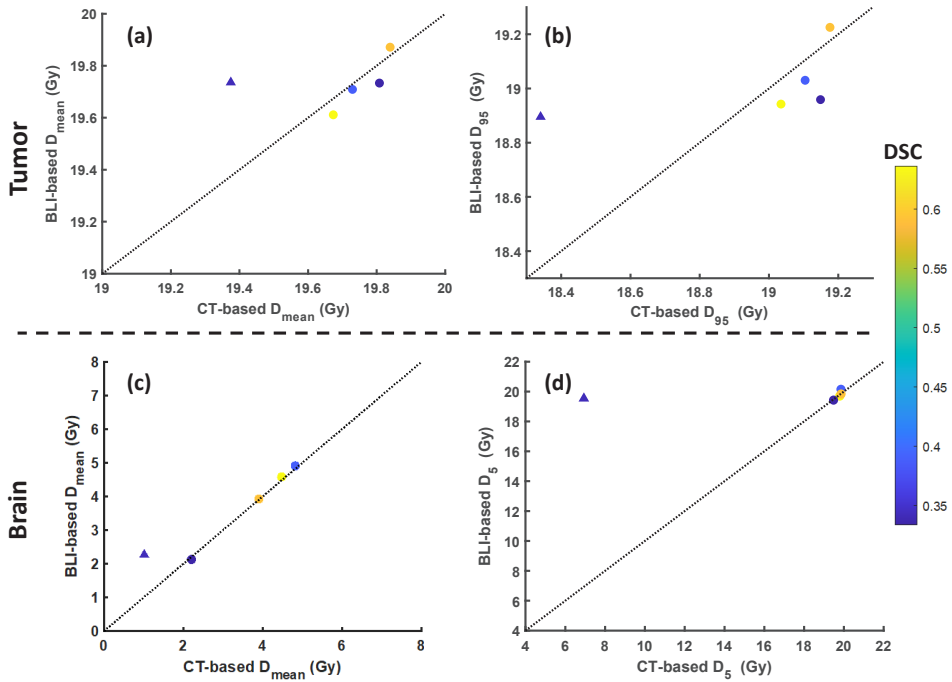


Figure 4.12 – DVM for real BLI acquisitions: (a,b) DVM for tumor, and (c,d) DVM for the brain. DSC is color-coded and differences in collimator size are shown as different markers: circles or triangles are cases where the BLI-based collimator was the same size or larger than the CT-based collimator.

on animals. This can be further studied and developed using the same framework, i.e. by developing a suitable MC-based training database and training a similar deep learning model.

The results of this study show the feasibility of BLI-based precision radiotherapy. The proposed deep learning algorithm works well in a large variety of simulated cases, with tumors ranging from 10-270 mm³ in size. Tumors smaller than 10 mm³ were excluded from this study since they are too small to be targeted accurately using the BLI signal. The performance of the proposed method can be quantified in two distinct tasks: (a) tumor position accuracy, and (b) tumor shape prediction accuracy. The proposed DL-based solution provided excellent submillimeter accuracy for the tumor position. Despite this, the proposed method cannot fully capture the detailed shape characteristics of a tumor and often provides a smoothed-out prediction compared to the ground-truth tumor mask. In addition, the overly smoothed prediction is not necessarily a drawback of the proposed method since it is often needed to add a margin to the ground-truth contours. The effect of the added margin and the trade-off between the coverage and the excess treatment is presented in Figure 4.6(a-b). As shown, a margin of 0.8 mm provides the best trade-off between good tumor coverage and limited healthy tissue exposure in the MCS database. Finally, most

commercially available precision radiotherapy systems for small animals cannot irradiate such small detailed shape variations conformally.

The proposed solution, with median DSC and ΔCoM of 61% and 0.61 mm, exceeds our previous publication^[12], which used an AI solution to predict the tumor's CoM. Specifically, the CoM method provided median DSC and ΔCoM of 56% and 1.01 mm on the same database (excluding tumors below 10 mm³). The proposed solution is also superior to the mathematical solution in a similar GBM mouse model^[26]. Xu et al. reported an average DSC and ΔCoM of 55% and 0.62 mm, which is slightly lower than the performance of the proposed solution. Nonetheless, Xu reported the results using real GBM mouse experiments, while the proposed solution in this study is evaluated using the MCS database of rat experiments, which makes a direct comparison between the two methods challenging.

The DVMs for the MCS database, shown in Figure 4.8, reveal that the proposed DL-based solution can provide acceptable tumor dose coverage for most cases while delivering a limited dose to the organ at risk. However, in this study, no margin scheme is considered for planning. Therefore, both the cGTV and bGTV are considered without added margin and only the imposed margins by the circular collimator of fixed sizes are considered. Nevertheless, the effect of margins is investigated in the geometrical coverage evaluation, and it is likely to assume that adding a treatment margin would control the spread in the tumor dose coverage with the cost of an additional brain dose. In other words, the spread of points in Figure 4.8(a,b) below the identity line can be avoided by including a proper margin. It is shown that a margin of 0.8 mm can increase the median geometrical tumor coverage to 97%. Furthermore, the results suggest that using BLI-based collimators smaller than 8 mm will increase the probability of delivering less dose to the tumor. Additionally, it is important to note that the tested beam configuration might influence the dose coverage greatly. Although the parallel opposed beam configuration is selected based on a previous study without any correlation to the proposed BLI-based solution, the beam configuration seems to compensate for the BLI-based targeting error. This is especially apparent for the real measurement cases where the displacement error in the anterior-posterior direction is mitigated by the proposed beam configuration.

It is worth mentioning that in some of the cases, both in the MCS database and real BLI acquisitions, the predicted bGTV slightly overlaps with the skull, as can be seen in Figure 4.11(b). Such overlap will cause a long flat tail in the DVH due to the high dose in the bone when irradiating with 225 kV x-rays (when calculating dose-to-medium-in-medium in Monte Carlo dose calculations). This can be easily removed in the post-processing steps by automatically removing the skull from the bGTV and only considering overlapping regions with the brain.

The robustness analysis provided valuable insights about the proposed

AI-based solution. The trained model using the initial samples performs mediocre for out-of-distribution cases, especially flat tumors and tumors located at random locations inside the brain. It is speculated that poor performance for randomly located tumors is most likely related to the wrong location of the implantation drill hole with respect to the location of the synthetic tumor. In other words, the trained network has observed an indirect effect of the punctured skull since most MCS observations included such an effect as a hotspot in the BSF directly above the drill hole. Therefore, some of the synthetic cases provided unrealistic and unfamiliar samples for which the tumors were not located directly below the punctured location in the skull. In addition, another important observation from the robustness analysis is the reduced performance on the original cases once the network is trained with the additional synthetic cases, which again can be the result of unrealistic cases.

The performance of the proposed solution decreased slightly for a small set of real BLI measurements compared to the MC simulated data. This is believed to be a direct outcome of the limitations of artificial intelligence methods, such as the proposed algorithm, and their dependence on the quality of the training data. Therefore, the trained model on the MC simulations struggles with the increased level of variations in the real measurements. The provided normalization and preprocessing steps restricted the adverse effect of the measurement noise on the predictions. In spite of this, a larger set of real BLI measurements is required to enhance the model's robustness and reduce uncertainties, especially for unseen samples.

The fully convolutional ResNet architecture enables more efficient use of limited hardware resources, especially the GPU, compared to the fully-connected multi-layer perceptron counterparts. Furthermore, the computational efficiency of the developed method is far superior to analytical models in the inference phase, making the proposed method a viable option for real-time BLI-based treatment planning for small animals. The proposed DL model, on the median, takes 532 ± 6 ms to predict the 3D tumor contour on an NVIDIA RTX A6000 GPU. This is of great importance for the small animal precision radiotherapy workflow since animals are required to remain under anesthesia during the whole imaging, planning, and treatment workflow, which makes rapid BLI reconstruction necessary.

The main drawback and challenge of the proposed deep learning approach is the availability and quality of the training database. Despite our best efforts to address this problem with a high-quality MC-simulated database, the provided training database is considered small in the field of AI and can increase the probability of overfitting. This is frequently an issue for pre-clinical AI imaging applications. Although the proposed solution is optimized to decrease the effect of such a small-sized training database on the predictions, the epistemic uncertainty remains high, which specifies the performance of any machine-learning model in regard

to out-of-database samples.

The proposed solution does not fully exploit the current capabilities of the BLI and only relies on a time and spectral-integrated acquisition. However, we believe that adding spectral information (using the available light filters) in the form of either adding more input channels or an ensemble of AI models per spectrum can yield better performance. In addition to multispectral-enabled AI, physics-informed deep learning models are another potential candidate for improving the outcomes of this study. These models can couple the flexibility of the AI solutions with the explainability of physics models and provide a synergy between the two.

Conclusion

In this paper, a novel real-time DL solution is presented to accelerate the BLI-based treatment planning problem. The proposed method can achieve good quality planning for the majority of the cases presented here, and therefore demonstrates the proof of concept of using AI-based BLI volumetric reconstruction. However, this study is just a starting point for the use of fully convolutional deep learning approaches in this field, and like many other deep learning solutions, the quality of the proposed solution can be improved with more data generated from similar studies, and from using other information derived from the BLI images such as multi-spectral BLI.

Acknowledgment

This work was partially supported by special research fund for double doctorate degree projects in the framework of the cooperation between Hasselt university and Maastricht UMC+ (Grant No. R-8216).

Ethical statement

μ CBCT images were re-used from previous animal experiments, which were all in accordance with local institutional guidelines for animal welfare and approved by the Animal Ethical Committee of Maastricht University (protocol number 2017-012).

References

- [1] K. H. Brown et al., "A scoping review of small animal image-guided radiotherapy research: Advances, impact and future opportunities in translational radiobiology," *Clin. Transl. Radiat. Oncol.*, vol. 34, pp. 112–119, May 2022, doi: 10.1016/j.ctro.2022.04.004.
- [2] F. Verhaegen et al., "Roadmap for precision pre-clinical x-ray radiation studies," *Phys. Med. Biol.*, vol. 68, no. 6, p. 06RM01, Mar. 2023, doi: 10.1088/1361-6560/acaf45.
- [3] A. Vaniqui, L. E. J. R. Schyns, I. P. Almeida, B. van der Heyden, S. J. van Hoof, and F. Verhaegen, "The impact of dual energy CT imaging on dose calculations for pre-clinical studies," *Radiat. Oncol.*, vol. 12, no. 1, p. 181, Nov. 2017, doi: 10.1186/s13014-017-0922-9.
- [4] F. Verhaegen, P. Granton, and E. Tryggestad, "Small animal radiotherapy research platforms," *Phys. Med. Biol.*, vol. 56, no. 12, pp. R55-83, Jun. 2011, doi: 10.1088/0031-9155/56/12/R01.
- [5] A. M. Mowday et al., "Use of a Luciferase-Expressing Orthotopic Rat Brain Tumor Model to Optimize a Targeted Irradiation Strategy for Efficacy Testing with Temozolomide," *Cancers*, vol. 12, no. 6, Art. no. 6, Jun. 2020, doi: 10.3390/cancers12061585.
- [6] B. Stegen et al., "Contrast-enhanced, conebeam CT-based, fractionated radiotherapy and follow-up monitoring of orthotopic mouse glioblastoma: a proof-of-concept study," *Radiat. Oncol.*, vol. 15, no. 1, p. 19, Jan. 2020, doi: 10.1186/s13014-020-1470-2.
- [7] S. Yahyanejad et al., "Complementary use of bioluminescence imaging and contrast-enhanced micro-computed tomography in an orthotopic brain tumor model," *Mol. Imaging*, vol. 13, 2014, doi: 10.2310/7290.2014.00038.
- [8] F. Verhaegen et al., "ESTRO ACROP: Technology for precision small animal radiotherapy research: Optimal use and challenges," *Radiother. Oncol.*, vol. 126, no. 3, pp. 471–478, Mar. 2018, doi: 10.1016/j.radonc.2017.11.016.
- [9] Z. Deng et al., "Quantitative Bioluminescence Tomography for In Vivo Volumetric-Guided Radiotherapy," *Methods Mol. Biol.*, 2022, doi: 10.1007/978-1-0716-1803-5_38.
- [10] Z. Deng et al., "In vivo Bioluminescence Tomography Center of Mass-Guided Conformal Irradiation," *Int. J. Radiat. Oncol. Biol. Phys.*, vol. 106, no. 3, pp. 612–620, Mar. 2020, doi: 10.1016/j.ijrobp.2019.11.003.
- [11] S. Ropic, T. Samuel, P. E. Lindsay, S. Ansell, R. A. Weersink, and R. S. DaCosta, "Assessing the Accuracy of Bioluminescence Image-Guided Stereotactic Body Radiation Therapy of Orthotopic Pancreatic Tumors Using a Small Animal Irradiator," *Radiat. Res.*, Feb. 2022, doi: 10.1667/RADE-21-00161.1.
- [12] B. Rezaeifar et al., "A deep learning and Monte Carlo based framework for bioluminescence imaging center of mass-guided glioblastoma targeting," *Phys. Med. Ampmathsemicolon Biol.*, vol. 67, no. 14, p. 144003, Jul. 2022, doi: 10.1088/1361-6560/ac79f8.
- [13] H. Dehghani, J. Guggenheim, S. L. Taylor, X. Xu, and K. Wang, "Quantitative bioluminescence tomography using spectral derivative data," *Biomed. Opt. Express*, 2018, doi: 10.1364/BOE.9.004163.

- [14] J. M. Valverde, A. Shatillo, R. De Feo, O. Gröhn, A. Sierra, and J. Tohka, "RatLesNetv2: A Fully Convolutional Network for Rodent Brain Lesion Segmentation," *Front. Neurosci.*, vol. 14, p. 610239, Dec. 2020, doi: 10.3389/fnins.2020.610239.
- [15] X. He et al., "Sparse reconstruction for quantitative bioluminescence tomography based on the incomplete variables truncated conjugate gradient method," *Opt. Express*, vol. 18, no. 24, p. 24825, Nov. 2010, doi: 10.1364/OE.18.024825.
- [16] Y. Gao, K. Wang, Y. An, S. Jiang, H. Meng, and J. Tian, "Nonmodel-based bioluminescence tomography using a machine-learning reconstruction strategy," *Optica*, vol. 5, no. 11, pp. 1451–1454, Nov. 2018, doi: 10.1364/OPTICA.5.001451.
- [17] W. E. C. Ma, S. Wojtowysch, and L. Wu, "Towards a Mathematical Understanding of Neural Network-Based Machine Learning: what we know and what we don't," *ArXiv200910713 Cs Math Stat*, Dec. 2020, Accessed: Apr. 14, 2022. [Online]. Available: <http://arxiv.org/abs/2009.10713>
- [18] V. Cuplov, I. Buvat, F. Pain, and S. Jan, "Extension of the GATE Monte-Carlo simulation package to model bioluminescence and fluorescence imaging," *J. Biomed. Opt.*, vol. 19, no. 2, p. 026004, Feb. 2014, doi: 10.1117/1.JBO.19.2.026004.
- [19] M. Mesradi et al., "Experimental and analytical comparative study of optical coefficient of fresh and frozen rat tissues," *J. Biomed. Opt.*, vol. 18, no. 11, p. 117010, Nov. 2013, doi: 10.1117/1.JBO.18.11.117010.
- [20] H. Soleimanzad, H. Gurden, and F. Pain, "Optical properties of mice skull bone in the 455- to 705-nm range," *J. Biomed. Opt.*, vol. 22, no. 1, p. 10503, Jan. 2017, doi: 10.1117/1.JBO.22.1.010503.
- [21] H. Zhao, T. C. Doyle, O. Coquoz, F. Kalish, B. W. Rice, and C. H. Contag, "Emission spectra of bioluminescent reporters and interaction with mammalian tissue determine the sensitivity of detection in vivo," *J. Biomed. Opt.*, vol. 10, no. 4, p. 41210, Aug. 2005, doi: 10.1117/1.2032388.
- [22] T. Akiba, S. Sano, T. Yanase, T. Ohta, and M. Koyama, "Optuna: A Next-generation Hyperparameter Optimization Framework," in *Proceedings of the 25th ACM SIGKDD International Conference on Knowledge Discovery & Data Mining*, in *KDD '19*. New York, NY, USA: Association for Computing Machinery, Jul. 2019, pp. 2623–2631. doi: 10.1145/3292500.3330701.
- [23] J. Bergstra, R. Bardenet, Y. Bengio, and B. Kégl, "Algorithms for Hyper-Parameter Optimization," in *Advances in Neural Information Processing Systems*, Curran Associates, Inc., 2011. Accessed: May 23, 2022. [Online]. Available: <https://papers.nips.cc/paper/2011/hash/86e8f7ab32cfd12577bc2619bc635690-Abstract.html>
- [24] G. Lappas et al., "Automatic contouring of normal tissues with deep learning for pre-clinical radiation studies," *Phys. Med. Biol.*, vol. 67, no. 4, Feb. 2022, doi: 10.1088/1361-6560/ac4da3.
- [25] R. A. Weersink et al., "Integration of optical imaging with a small animal irradiator," *Med. Phys.*, vol. 41, no. 10, p. 102701, 2014, doi: 10.1118/1.4894730.
- [26] X. Xu et al., "Quantitative Bioluminescence Tomography-Guided Conformal Irradiation for Pre-clinical Radiation Research," *Int. J. Radiat.*

Oncol. Biol. Phys., vol. 111, no. 5, pp. 1310–1321, Dec. 2021, doi:
10.1016/j.ijrobp.2021.08.010.

Supplementary Material

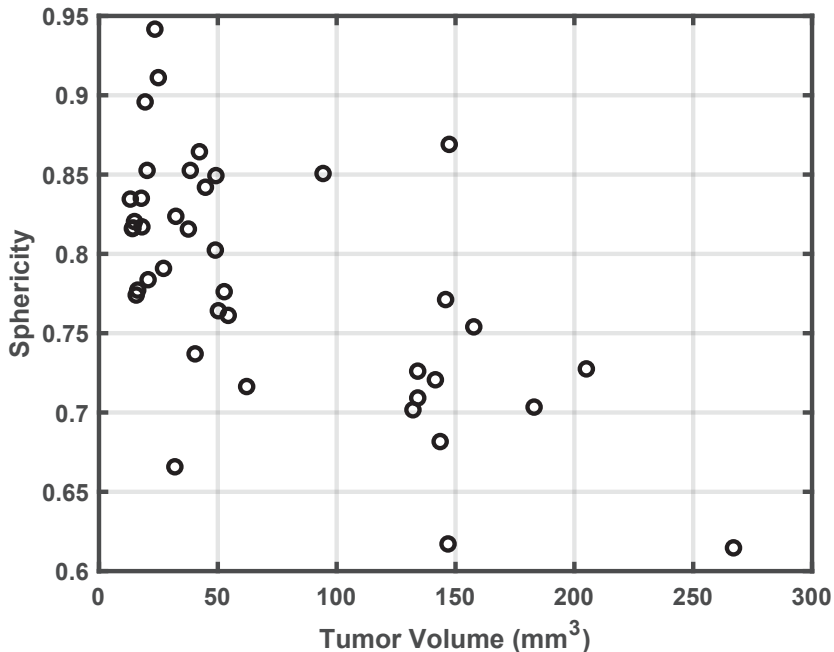
F98 Database

The database used in this study is obtained from the study by Mowday et al., 2020. This database includes Cone-beam CT scans (CBCT) of 34 animals at different time points, resulting in 57 hand-delineated CBCT images. In this study, an exclusion criterion based on the tumor volume is introduced, and therefore, the size of the database is further reduced to 42 cases. The samples within the F98 database include a variety of tumor shapes and sizes. To quantify the variations within the database, the sphericity metric is used, which quantifies the shape similarities to a perfect sphere as follows:

$$S = \frac{\sqrt[3]{36\pi V^2}}{A}$$

Where A is the surface area and V is tumor volume. Based on this definition for a perfect sphere, S will be equal to one.

F1 presents the shape-size variations within the F98 database. As can be seen in this figure, the F98 database includes a variety of tumor sizes (volume between 10-267 mm³) and shapes (sphericity between 0.95 and 0.61).

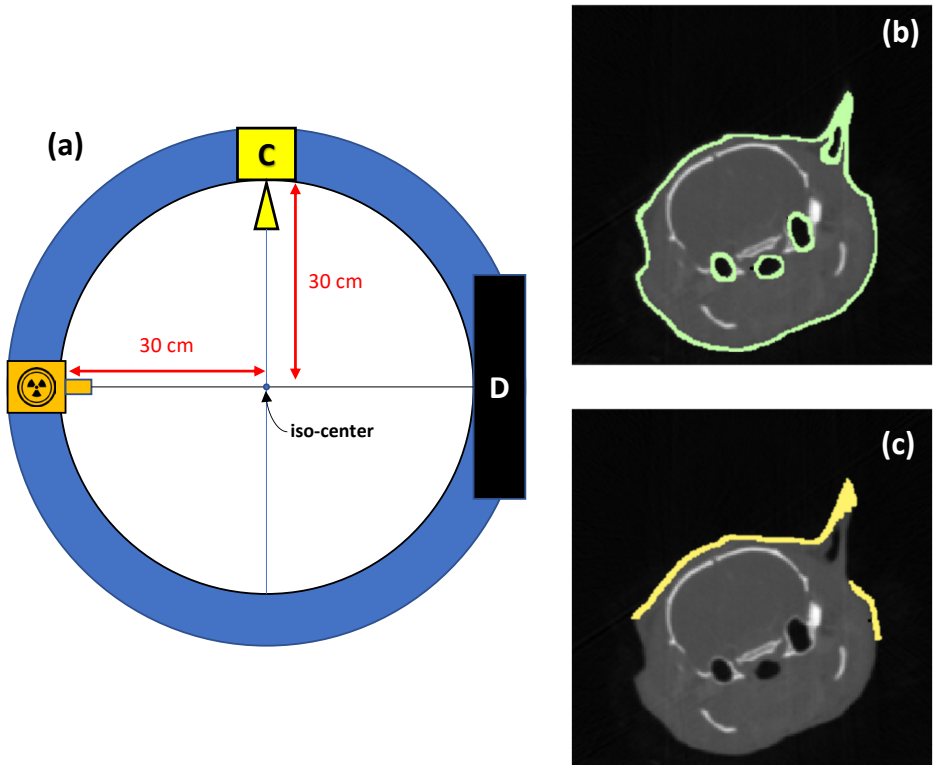


Supplementary Figure 1 – The shape variations within the F98 database: sphericity is a metric of shape similarity to a perfect sphere. The sphericity of 1 is equal to a perfect sphere.

Camera Model

In this study, first, an approximation of the skin mask is created by applying the morphological operators on the air voxels in the CT scan, which can be obtained using a constant threshold. However, since the air voxels are used, the approximated skin mask at this stage will include the inner parts of the ears and the nasal cavity, as it is shown in Supplementary Figure 2. In an extension to our previous study (Rezaeifar et al., 2022), it was realized that such areas could play an important role in the deep learning decision as they are often in the proximity of the tumor and, especially for larger tumors, can result in high photon counts in the Monte Carlo simulations (MCS). Therefore, the deep learning model pays extra attention to these areas. Although in the MCS, these regions are accurately modeled and have acceptable photon counts, in reality, it is not feasible to receive any photon counts from these regions, mostly due to camera occlusion. Therefore an additional step is required to remove the redundant information from the skin mask.

In an ideal case, a ray-tracing algorithm is needed to model the camera occlusion accurately. However, due to the computational costs of such algorithms, a simplified version is employed here. Therefore, instead



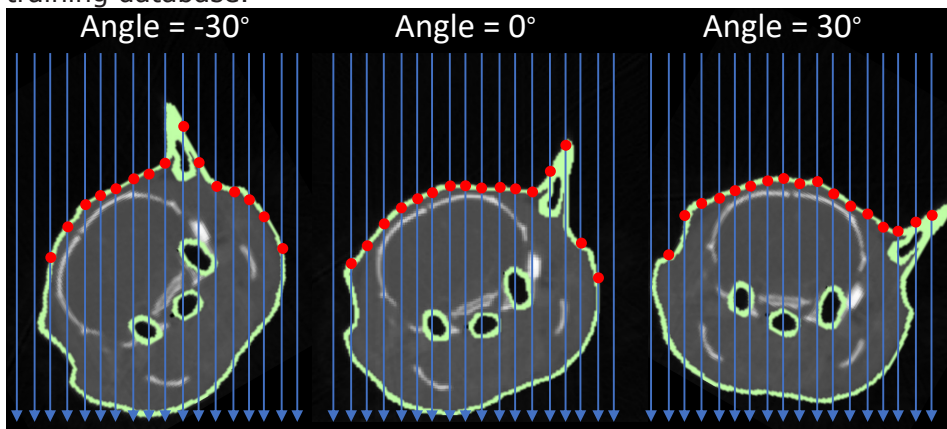
Supplementary Figure 2 – Overview of the imaging system (Xrad 225Cx, Precision X-ray, USA.) shown in (a), the approximated skin mask in (b), and the final modified skin mask with limited camera viewing angle in upper hemisphere (c)

of modeling the camera and its field of view using a ray-tracing model, camera rotation is approximated by the imaging object's rotation. A second assumption is introduced by considering light beams from the camera to the object to be parallel. Although such simplifications can be considered corruptive in many applications since the main aim here is to remove the redundant parts of the skin mask and the distance between the camera and the imaged object is much higher than geometrical variations in the object, it can be considered as an acceptable simplification. Therefore, in the simplified algorithm, parallel rays are considered for each camera viewing angle and only the voxels closest to the camera are included to be located on the visible part of the skin. This is equal to finding the first non-zero value in the rotated version of the approximated skin mask along columns in the 3D volume, as shown in Supplementary Figure 3.

In this study, a set of five camera viewing angles are considered according to the real measurements, including 0 , ± 30 , and ± 60 degrees. The resulting binary mask from each viewing angle is rotated back to the original angle and summed up with the remaining angles. In the resulting volume, every voxel with a value larger than one is visible in at least one camera viewing angle and, therefore, is considered in the skin's binary mask. Finally, a set of morphological operators are applied to the skin mask to remove small islands and also remove any gap between the adjacent voxels.

Synthetic Cases

In order to increase the size of the training database, a set of MCS is performed on artificially-build cases, hereafter called Synthetic cases. The aim of the Synthetic case database is: (a) to evaluate the robustness of the model for cases outside the training database and (b) to investigate the performance gain once these synthetic samples are added to the training database.



Supplementary Figure 3 – visualization of ray-tracing simplification used in this study shown in a representative 2D slice.

The original F98 database, obtained from real glioblastoma orthotopic rat models, is utilized to create a set of Synthetic cases in four distinct categories. In all four categories of the Synthetic cases, the simulation geometry, i.e. animal anatomy with no tumor, is selected randomly from the F98 database. For the tumor, on the other hand, the four categories are different, including: (a) randomly selected tumors located near the center of mass (CoM) of the original tumor for the specified simulation geometry, (b) randomly selected tumors located at a random location within the brain, (c) deterministically selected tumor equal to the deep learning prediction for the specified tumor, and (d) one of the two flat tumors within the F98 database either located at the CoM of the original tumor or manually located at the surface of the brain. Furthermore, the randomly selected tumors, in categories (a) and (b), are restricted to tumors larger than 10 mm³ and also transformed by a random affine transformation to generate more tumor shape variations. The random affine transformation at this stage is specified by its random 360-degree rotation along all axes, a limited random 10-degree shear to avoid very flatten out shapes, and a random scaling factor.

The resulting augmented tumor shape is then placed at an arbitrary location inside the brain. For category (a) cases, a grid of coordinates inside the brain is obtained. At each iteration, one coordinate is selected randomly and checked whether the entire tumor shape falls inside the brain if its center of mass is placed on the selected coordinate.

Deep Learning Hyper-parameter Optimization

In order to optimize the hyper-parameters (HP) of the RatLesNet model (Valverde et al., 2020) used in this study, an automatic HP optimization tool, namely Optuna (Akiba et al., 2019), has been employed. Optuna requires a pre-defined set of HP and a search space for each to function. Once the setup is clear, Optuna will create a pre-defined number of trials on the search space and, with the help of an arbitrary cost function, finds the best set of HP for the model.

In this study, the following HP is selected to be optimized using Optuna: (a) the number of filters in the convolutional layers, (b) the loss function and its parameters, and (c) the optimization algorithm and its parameters. The selection of the optimizable HP is based on the importance of each parameter in the literature and our previous experience. For example, it is well proven that the learning rate (lr) is the most important HP for deep learning algorithms (Smith, 2017) while the size of convolutional kernels in the model architecture might be less important. Supplementary Table 1 presents an overview of the optimized HP and their corresponding ranges.

Supplementary Table 1 – Selection of optimized hyperparameters and their range

HP	Input Type	Range	Sub-parameters	Range
Number Filters	integer	[12 40]	-	-
Loss Function	categorical	MSE	-	-
		Dice	-	-
		Focal	α γ	[0.2 0.8] [0.2 0.8]
Optimizer	categorical	Adam	lr	[10 ⁻⁴ 10 ⁻²]
			wd	[10 ⁻¹⁰ 10 ⁻³]
		SGD	lr wd	[10 ⁻⁵ 10 ⁻¹] [10 ⁻¹⁰ 10 ⁻³]
		RMSProp	-	-

Number of filters determines the number of learnable features inside the deep learning model. In the RatLesNet architecture, the specified number of filters is reached in the first convolutional layer and kept constant throughout the network. Therefore, increasing the number of filters within the convolutional layers will drastically increase the GPU memory needed. For this reason, the maximum number of filters is selected based on the available GPU memory.

Another important HP is the loss function and, in this study, three distinct loss functions are considered: Mean Squared Error (MSE), Dice, and Focal Tversky loss (Abraham and Khan, 2018). MSE simply calculates the error between the prediction and the ground truth (GT) and tries to minimize it. Dice loss, on the other hand, tries to maximize the overlap region between the two contours. Finally, Focal Tversky loss is a generalized version of dice loss that considers different weight factors for false positives and false negatives. The mathematical formulations of these loss functions are as follows:

$$\text{MSE}(V^1, V^2) = \frac{1}{n} \sum_{i,j,k} (V_{i,j,k}^1 - V_{i,j,k}^2)^2$$

$$\text{Dice}(V^1, V^2) = 1 - \frac{2TP}{2TP + FN + FP}$$

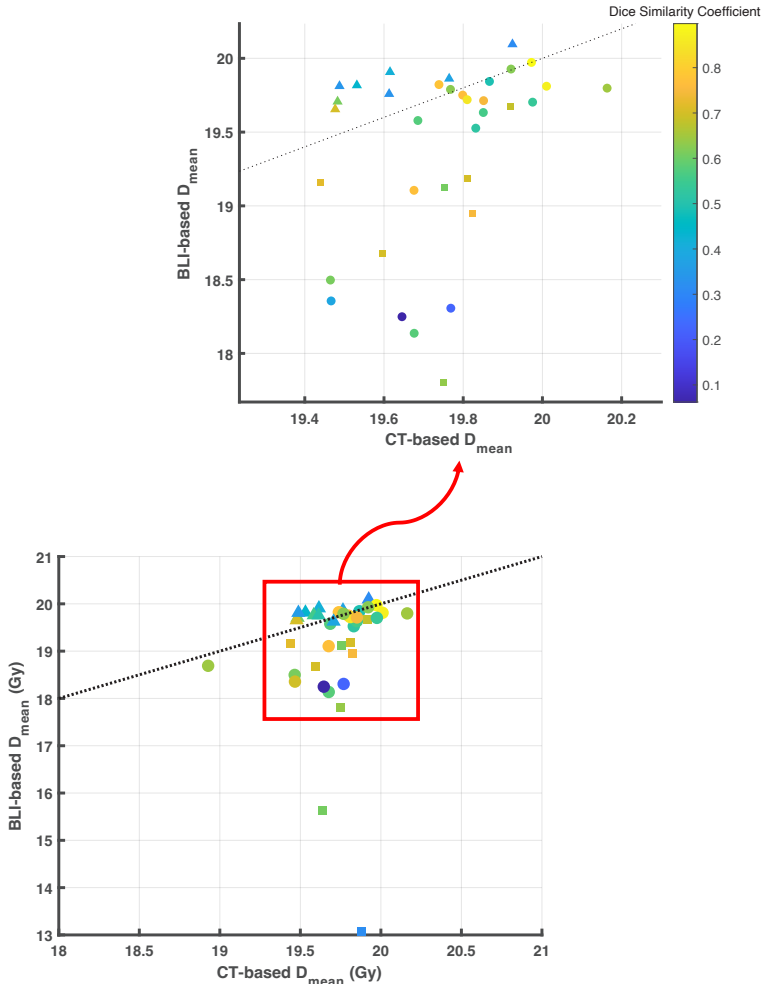
$$\text{Focal}(V^1, V^2) = \left(1 - \frac{TP}{TP + \alpha FN + \beta FP}\right)^\gamma$$

Where true positive (TP) is the agreement region between the GT and predicted contour, false negative (FN) marks the voxels that are in the GT but not included in the prediction and vice versa for the false positive (FP).

Finally, the optimizers used in the HP optimizations are one of the Adam, Stochastic Gradient Descent (SGD), and Root Mean Squared propagation (RMSprop) (Reddi et al., 2019) implemented in the Pytorch deep learning package (Paszke et al., 2019). In this study, the default optional parameters for each of the optimizers are considered and only the learning rate (lr) and the weight decay (wd) are considered as HP.

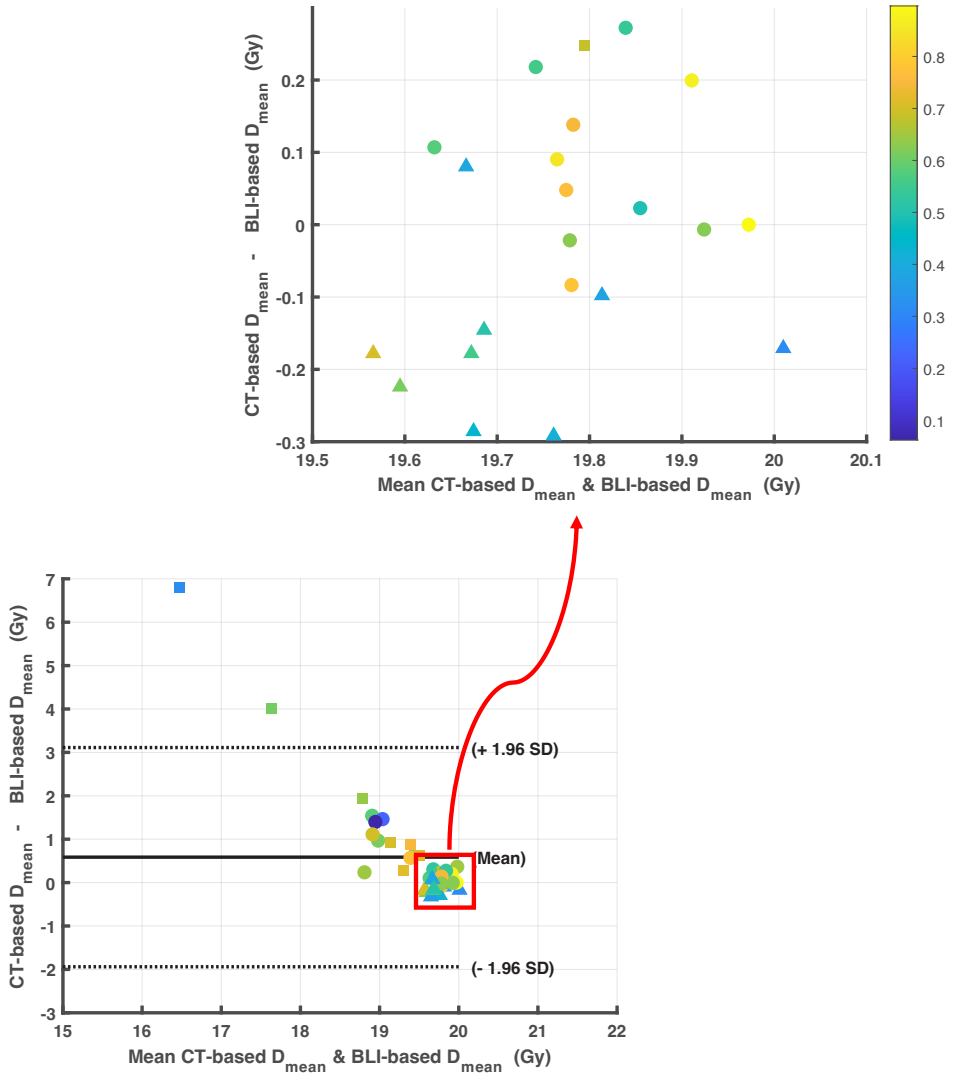
Dose Volume Metrics

In this section, a more detailed version of the dose-volume metric plots is presented, including the magnified version of the plots in the main text.

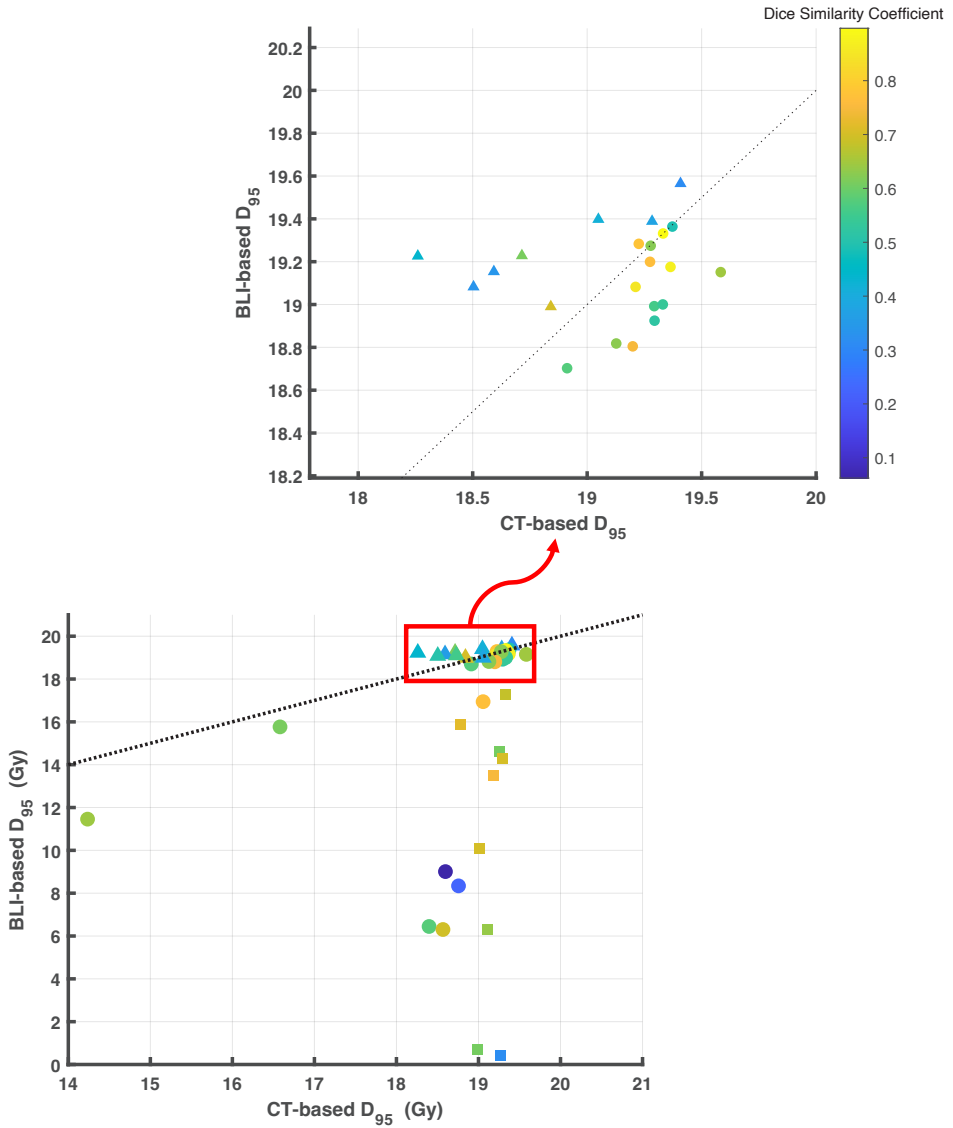


Supplementary Figure 4 – magnified scatter plot for mean dose delivered to the tumor (D_{mean})



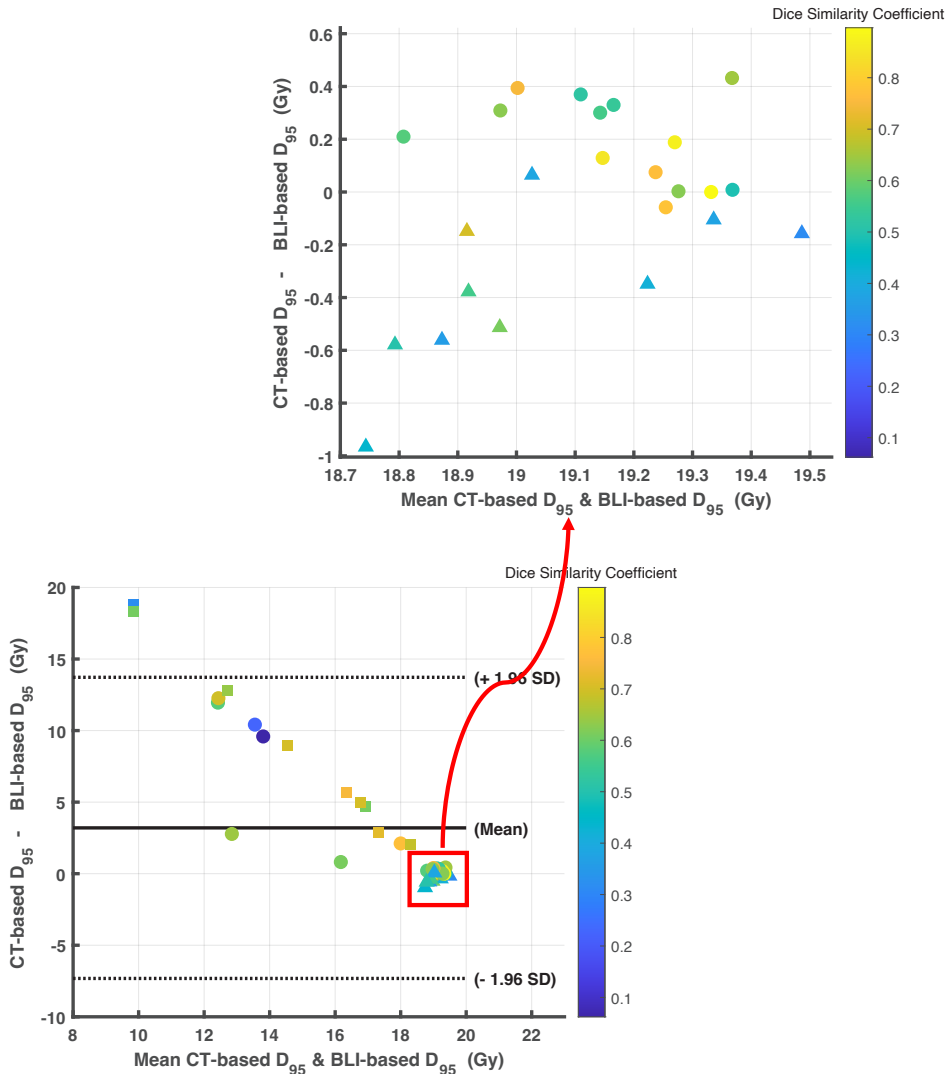


Supplementary Figure 5 – Bland-Altman acceptance plot for the mean dose to the tumor (D_{mean})

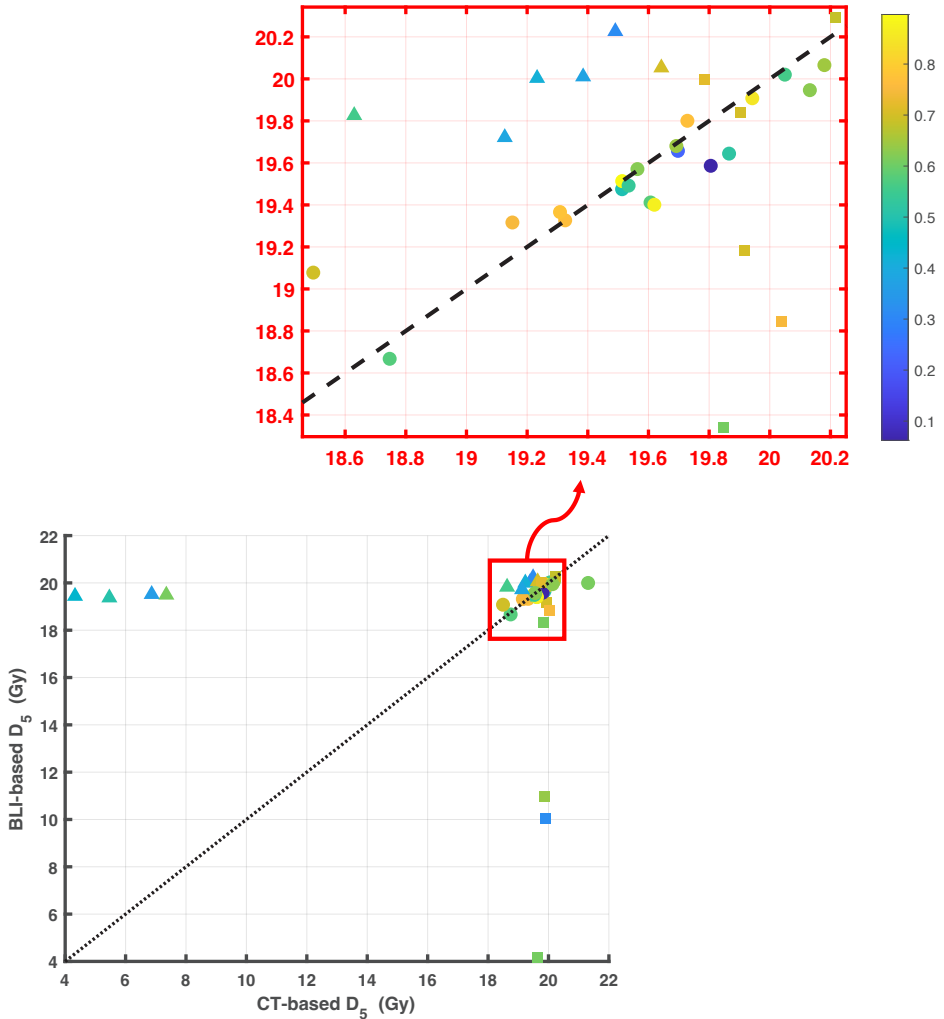


4

Supplementary Figure 6 – magnified scatter plot for the dose to 95% of tumor (D_{95})

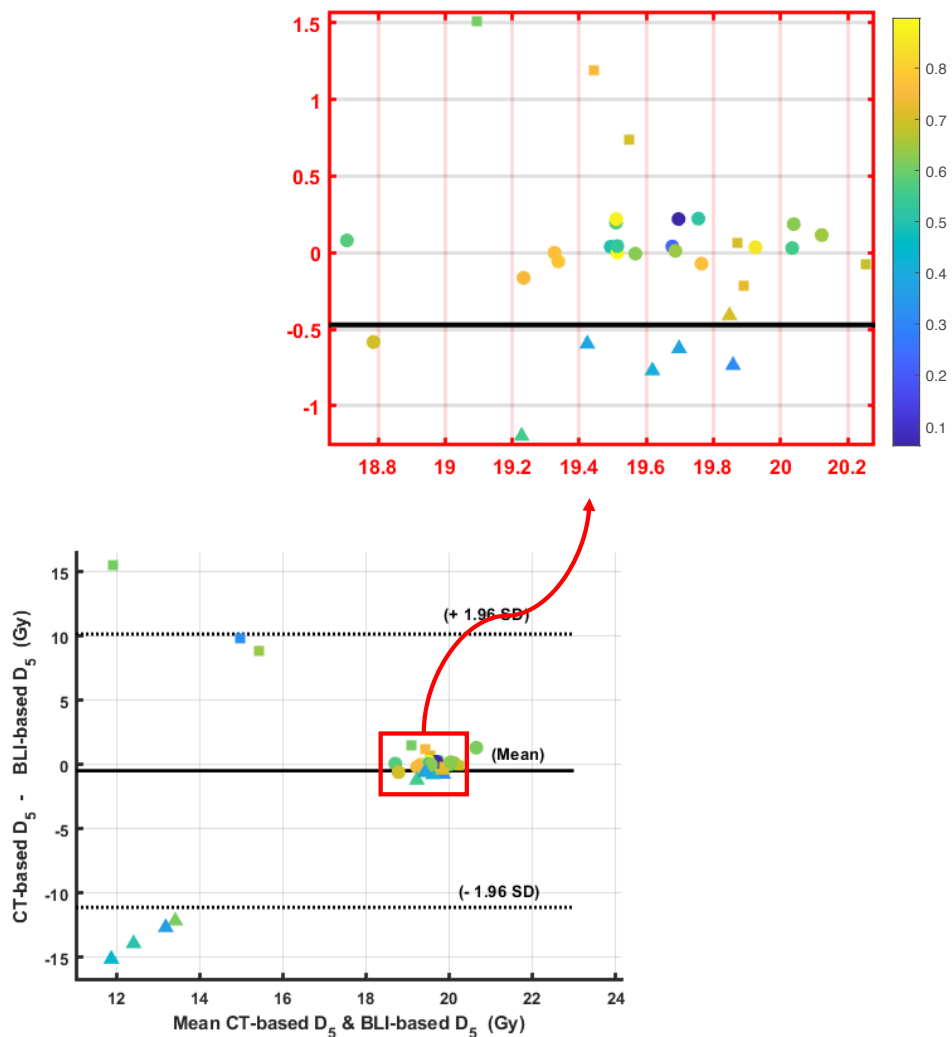


Supplementary Figure 7 – Bland-Altman acceptance plot for the dose to 95% of tumor (D_{95})



4

Supplementary Figure 8 – magnified scatter plot for the dose to 5% of brain (D_5)



Supplementary Figure 9 – Bland-Altman acceptance plot for the dose to 5% brain (D_5)

References

- Abraham, N., Khan, N.M., 2018. A Novel Focal Tversky loss function with improved Attention U-Net for lesion segmentation. <https://doi.org/10.48550/arXiv.1810.07842>
- Akiba, T., Sano, S., Yanase, T., Ohta, T., Koyama, M., 2019. Optuna: A Next-generation Hyperparameter Optimization Framework, in: Proceedings of the 25th ACM SIGKDD International Conference on Knowledge Discovery & Data Mining, KDD '19. Association for Computing Machinery, New York, NY, USA, pp. 2623–2631. <https://doi.org/10.1145/3292500.3330701>
- Mowday, A.M., Lieuwes, N.G., Biemans, R., Marcus, D., Rezaeifar, B., Reniers, B., Verhaegen, F., Theys, J., Dubois, L.J., 2020. Use of a Luciferase-Expressing Orthotopic Rat Brain Tumor Model to Optimize a Targeted Irradiation Strategy for Efficacy Testing with Temozolomide. *Cancers* 12, 1585. <https://doi.org/10.3390/cancers12061585>
- Paszke, A., Gross, S., Massa, F., Lerer, A., Bradbury, J., Chanan, G., Killeen, T., Lin, Z., Gimelshein, N., Antiga, L., Desmaison, A., Köpf, A., Yang, E., DeVito, Z., Raison, M., Tejani, A., Chilamkurthy, S., Steiner, B., Fang, L., Bai, J., Chintala, S., 2019. PyTorch: An Imperative Style, High-Performance Deep Learning Library. <https://doi.org/10.48550/arXiv.1912.01703>
- Reddi, S.J., Kale, S., Kumar, S., 2019. On the Convergence of Adam and Beyond. <https://doi.org/10.48550/arXiv.1904.09237>
- Rezaeifar, B., Wolfs, C.J.A., Lieuwes, N.G., Biemans, R., Reniers, B., Dubois, L.J., Verhaegen, F., 2022. A deep learning and Monte Carlo based framework for bioluminescence imaging center of mass-guided glioblastoma targeting. *Phys. Med. Ampmathsemicolon Biol.* 67, 144003. <https://doi.org/10.1088/1361-6560/ac79f8>
- Smith, L.N., 2017. Cyclical Learning Rates for Training Neural Networks. <https://doi.org/10.48550/arXiv.1506.01186>
- Valverde, J.M., Shatillo, A., De Feo, R., Gröhn, O., Sierra, A., Tohka, J., 2020. RatLesNetv2: A Fully Convolutional Network for Rodent Brain Lesion Segmentation. *Front. Neurosci.* 14, 610239. <https://doi.org/10.3389/fnins.2020.610239>

EMBARGOED

Chapter 5

Evaluating Deep-Learning Assisted Bioluminescence Tomography: A Monte Carlo Study

Authors

Behzad Rezaeifar, Cecile J.A. Wolfs, Natasja G. Lieuwes, Rianne Biemans, Brigitte Reniers, Ludwig J. Dubois, Frank Verhaegen.

In Preparation

EMBARGOED

Chapter 6

Improving AI-assisted tumor segmentation in pre-clinical glioblastoma rat models using complementary information from Contrast-Enhanced CT and Bioluminescence Imaging

Authors

Behzad Rezaeifar, Cecile J.A. Wolfs, Natasja G. Lieuwes, Rianne Biemans, Brigitte Reniers, Ludwig J. Dubois, Frank Verhaegen.

In Preparation

EMBARGOED

Chapter 7

Design and Manufacturing of Tissue-Mimicking Optical Phantoms for Bioluminescence Imaging of the glioblastoma rat models: a Pilot Study

Authors

Behzad Rezaeifar, Cecile J.A. Wolfs, Natasja G. Lieuwes, Rianne Biemans, Brigitte Reniers, Ludwig J. Dubois, Frank Verhaegen.

In Preparation

Chapter 8

Discussion and Future Perspectives

1. Introduction

Bioluminescence Imaging (BLI) constitutes an optical imaging modality geared toward pre-clinical cancer research on small animal tumor models. This imaging modality enables tumor growth monitoring in-vivo without additional X-ray radiation burden on the animals during imaging^[1]. However, BLI's application in routine pre-clinical cancer research remains quite limited to this date, with most centers using 2D BLI information to monitor tumor growth and little to no 3D reconstruction capabilities^[2]. Therefore, this thesis aims to improve the BLI application in routine pre-clinical cancer research by enhancing the accuracy of the difficult Bioluminescence Tomography (BLT) reconstruction problem.

This thesis focuses on the glioblastoma multiforme (GBM) tumor rat models as the primary animal model of interest. GBM is considered the most aggressive primary brain tumor, with the highest incidence among such tumors. Currently, the standard treatment for GBM includes a combination of radiotherapy and chemotherapy with temozolomide. In spite of this, GBM often relapses and has a poor prognosis. Therefore, fundamental pre-clinical research is essential to improve the efficacy of the standard treatment for GBM.

In this chapter, we discuss different aspects of the problem at hand and address future perspectives. This chapter is divided into four different parts. The first part addresses the current BLI applications in state-of-the-art pre-clinical cancer research studies and its limitations. Thereafter, the next section takes this discussion further by introducing the added benefits of the proposed AI-based solutions and their limitations. The third part aims to clarify the role of optical phantoms in enhancing BLI applications through standardization and quality assurance. Finally, future perspectives are discussed in the fourth part.

Part 1: The state-of-the-art 2D BLI

The majority of BLI applications in pre-clinical cancer research studies are limited to tumor growth monitoring using 2D BLI projections. As shown in Chapter 2 of this thesis, the research studies in this field mostly use 2D BLI to monitor tumor growth over time and track tumor response to certain treatments^{[3]-[5]}. In other words, a linear regression model is developed by linking the total number of photons reaching the camera at a certain projection angle to the tumor volume derived from the hand-delineated CT scan, as shown in Figure 2.1. A similar trend has been observed in the Monte Carlo Simulations (MCS) and utilized in Chapter 3 to estimate the volume of the sphere encapsulating the tumor. A direct comparison between the BLI-based growth monitoring fit from GBM rat models provided in Chapter 2, MCS of GBM rat models in Chapter 3, and GBM mouse models provided by Yahyanejad et al.^[4] shows that the quality of the linear fit is very similar in all cases, with a Pearson coefficient of approximately 0.8.

Even though such a high Pearson coefficient signals a strong correlation between the BLI signal and the CT-based tumor volume and allows for tumor growth monitoring, it fails to capture the correct volume for some cases, such as flat tumors seated close to the skull. It is safe to assume that the multispectral measurements can help alleviate this issue since each spectral bandwidth includes a different portion of the absorption coefficient and, in theory, can help distinguish smaller flat tumors close to the skull from larger deep-seated tumors. To clarify this further, assume the two different cases where a flat tumor and a larger tumor result in approximately the same number of photons reaching the skin. Consequently, these two tumors are considered to have similar volumes based on the linear fit. However, the multispectral information hold important details that differentiate the two cases since photons emitted from the larger tumor have to transport in a larger portion of the biological tissue. Therefore such a tumor gains more photon intensity by the reduced absorption coefficient in a different spectral bandwidth, such as a near-infrared spectrum.

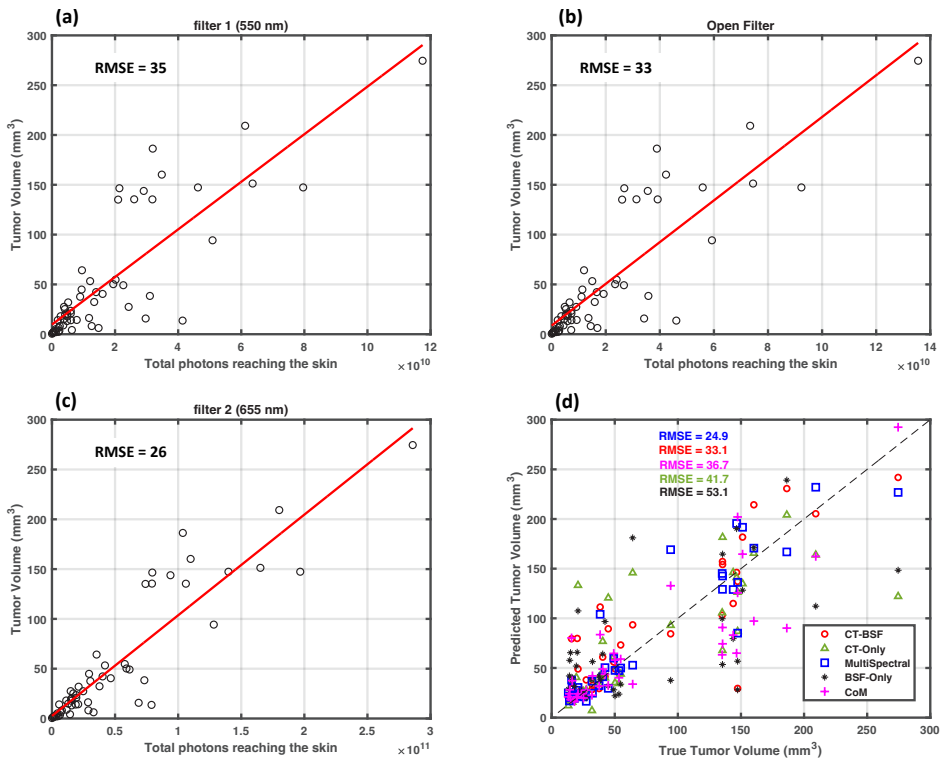


Figure 8.1 – BLI-based tumor volume estimation on Monte Carlo simulation database. (a-c) represent individual BLI-based volume fits for various spectral bandwidths, (d) is the comparison of volume prediction accuracy based on proposed AI solutions in this thesis

As shown in Figure 8.1, the multispectral measurements can result in a slightly different fit which might reduce the volume estimation errors. For example, the second filter used, centered around 655 nm, provides a better volume estimation than both open-filter, i.e. considering the entire photons in the visible range, and the first filter, centered around 550 nm. This might be due to less photon absorption and scattering in the higher wavelengths closer to the near-infrared spectrum, which results in a cleaner BSF signal.

Part 2: The AI-based solutions

This thesis represents one of the first endeavors in utilizing AI-driven approaches for the BLT reconstruction problem. Mathematical approaches, rooted in physics, demand accurate modeling and struggle with the complexity of biological environments. Despite potential interpretability, they may require substantial computational resources. In contrast, AI-based solutions, particularly deep learning models, exhibit greater adaptability to diverse conditions, rendering them more robust in uncertain scenarios. Their efficiency in real-time applications, facilitated by rapid reconstructions and reduced reliance on explicit models, stands out as a notable advantage.

In this thesis, chapters 3 to 6 discuss various AI-based solutions to the BLT reconstruction problem. The first solution revolves around predicting the central location of the tumor accurately and building a spherical target volume that envelops it, hence called the Center of Mass (CoM) model. Although the CoM model provides a satisfactory solution that enables BLI-based tumor targeting due to static and, often, circular beam collimation available in small animal irradiators, it does not include any shape information. Consequently, an elongated tumor shape will not receive an accurate radiation dose since it won't match the simplified spherical target volume unless unnecessarily large margins are employed. Therefore, Chapter 4 introduces a new deep learning approach that can predict the tumor's shape alongside its location, namely the BSF-only model. Chapter 5 not only discusses different aspects of the 3D BLT model but also introduces a novel approach to enhance the BLT reconstruction problem by utilizing the multispectral information from different wavelength bandwidths. Finally, a CT-BLT model is introduced in Chapter 6 with the best performance with respect to the dice similarity coefficient (DSC), mainly due to employing voxel information from the Contrast-Enhanced Cone-Beam CT (CE-CBCT). Chapter 6 also includes a baseline CT-only model that does not utilize the complementary BLI information and contours the tumor purely based on the CT information. Figure 8.2 presents a direct performance comparison between all of the AI-based solutions presented in this thesis. As depicted, the performance of the AI-based solutions increases with the complexity of the proposed AI model and the amount of complementary information presented to it. The CoM model utilizes a 3D convolutional neural network, which consists

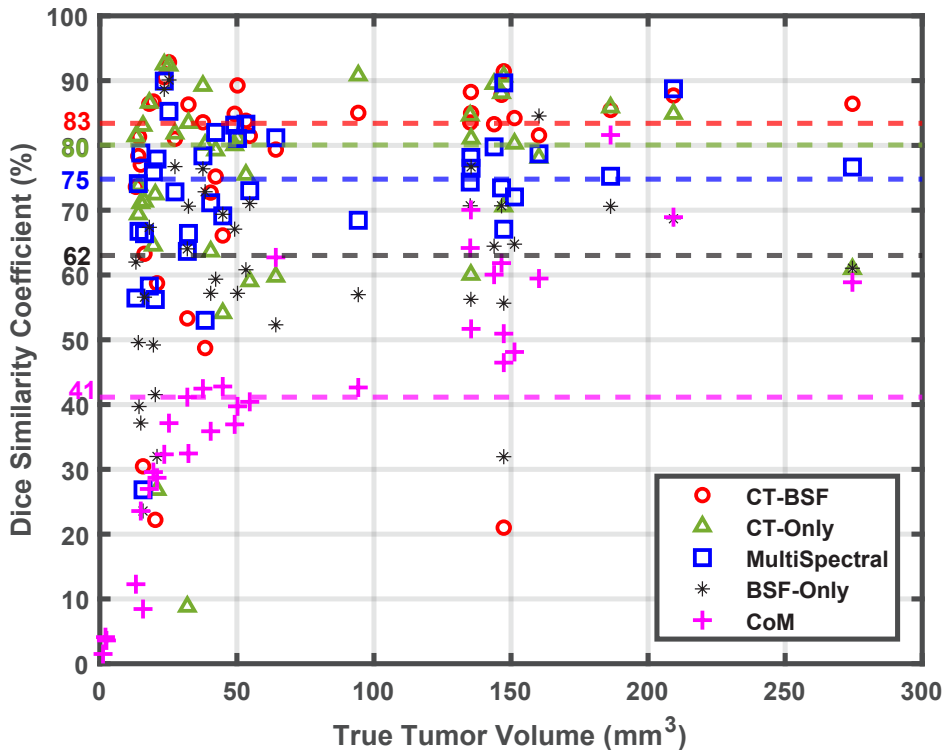


Figure 8.2 – Performance Evaluation comparison between the proposed AI-based solutions in this thesis

of a simpler architecture compared to the other models and, therefore, ranks last in this performance comparison. The CT-BSF model, on the other hand, uses not only a more advanced deep learning architecture but also complementary CT information, thus achieves the best accuracy. However, the application of each model is highly dependent on the availability of data and resources.

Five representative cases are illustrated in Figure 8.3, providing a visual comparison between the five models. The first two animals correspond with cases with average performance across the entire database and different models. Consequently, the provided solutions, on average, can provide accurate tumor targeting. The remaining cases in this figure showcase samples where at least one model struggles with tumor delineation. The CoM model fails to accurately determine tumor location in rat number three. Both CT-based models, CT-BSF and CT-only networks, struggle with the fourth rat, while the purely BLI-based solutions can provide more accurate contouring for the tumor. Conversely, the BLI-based solutions fail to distinguish the flat tumors close to the skull, while the CT-only model perfectly delineates such tumors.

Five representative cases are illustrated in Figure 8.3, providing a visual

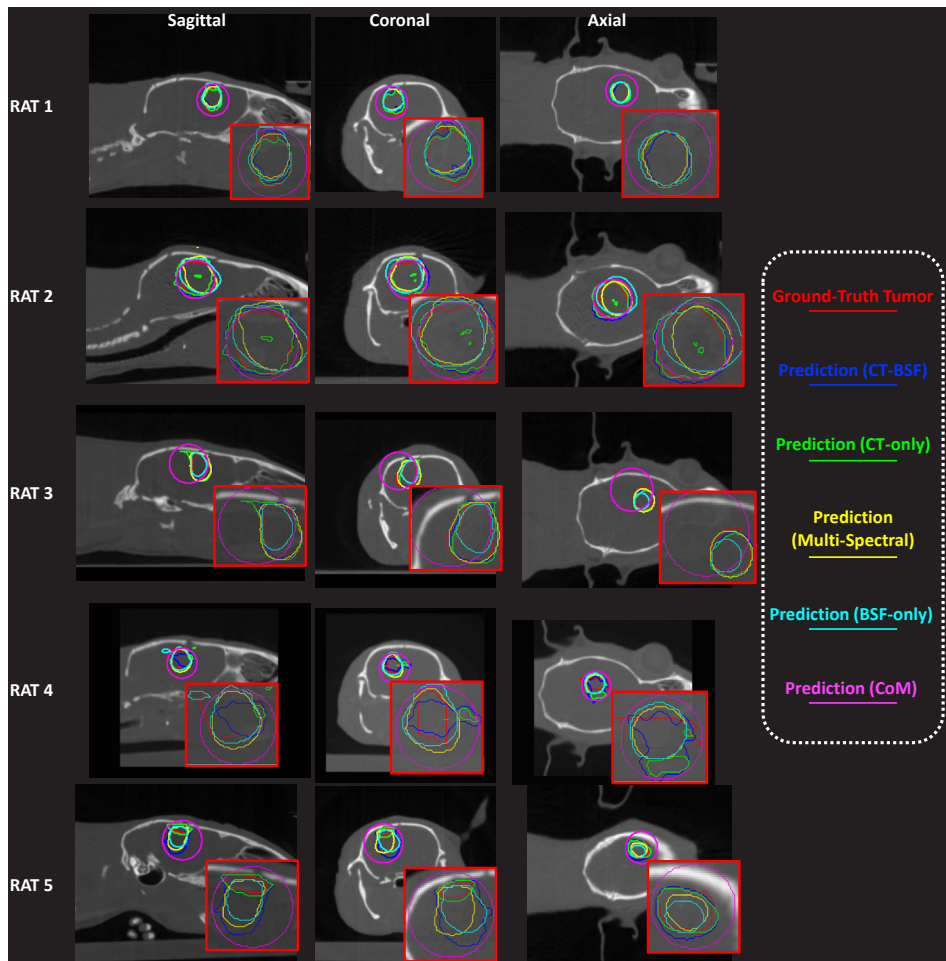


Figure 8.3 – Visualization of the tumor prediction using all the proposed AI-based solutions. Rats (1,2) represent two cases with median DSC across all the models. Rat 3-5 depict cases with failed CoM-based, CT-based, and BSF-based tumor targeting.

comparison between the five models. The first two animals correspond with cases with average performance across the entire database and different models. Consequently, the provided solutions, on average, can provide accurate tumor targeting. The remaining cases in this figure showcase samples where at least one model struggles with tumor delineation. The CoM model fails to accurately determine tumor location in rat number three. Both CT-based models, CT-BSF and CT-only networks, struggle with the fourth rat, while the purely BLI-based solutions can provide more accurate contouring for the tumor. Conversely, the BLI-based solutions fail to distinguish the flat tumors close to the skull, while the CT-only model perfectly delineates such tumors.

The comparison between the four models for the small tumors, i.e. tumors smaller than 10 mm^3 , is presented in Figure 8.4. All the models

except the CoM model are trained using tumors larger than 10 mm^3 ; therefore, such small tumors can test the robustness of each model. The three tumors were selected from 17 small tumors to have three classes: extremely tiny tumors (rat 1), median-sized small tumors (rat 2), and tumors slightly smaller than the exclusion criteria (rat 3). All the models encompass the CT-based tumor contour in their respective predicted volumes, which is important for BLI-based radiation targeting and treatment planning applications. However, in all the cases with such small tumors presented here, the AI-based solutions resulted in over-predicting the tumor contours, which is an expected behavior since the models are trained using larger volumes.

The multispectral model, presented in Chapter 5, provided a better prediction accuracy for the small-sized tumor experiment. This might be due to the increased uncertainty in CT-based tumor delineation for such small tumors, which results in a higher interobserver variability and challenges for the CT-BSF model.

Another important aspect of the AI-driven solution is prediction

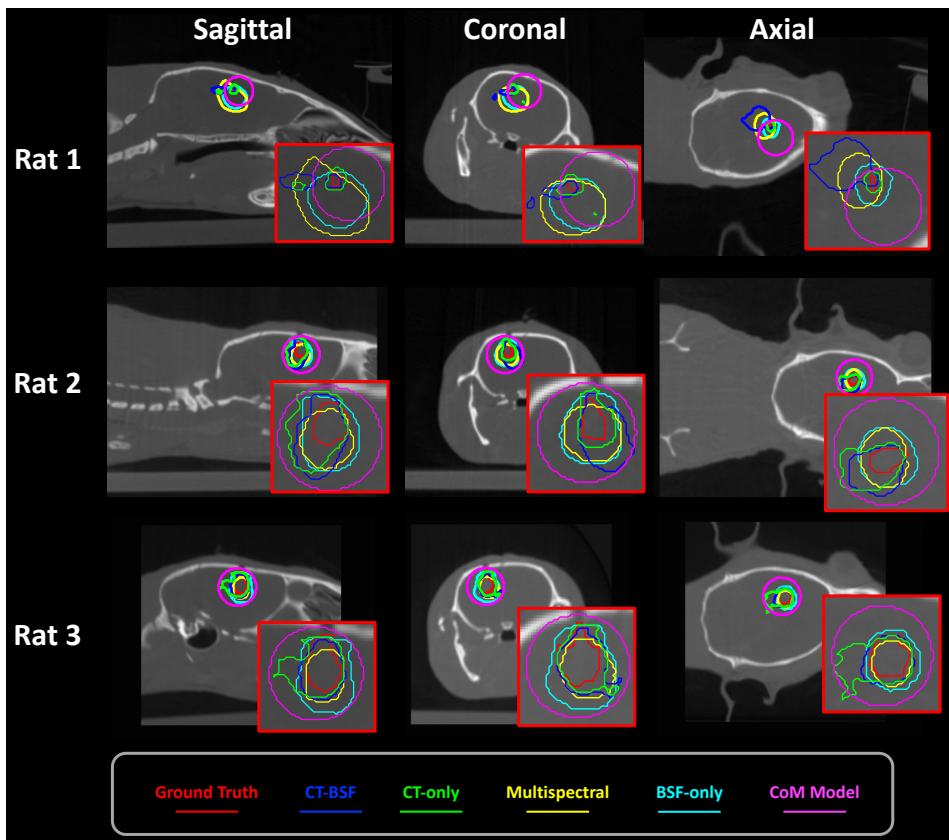
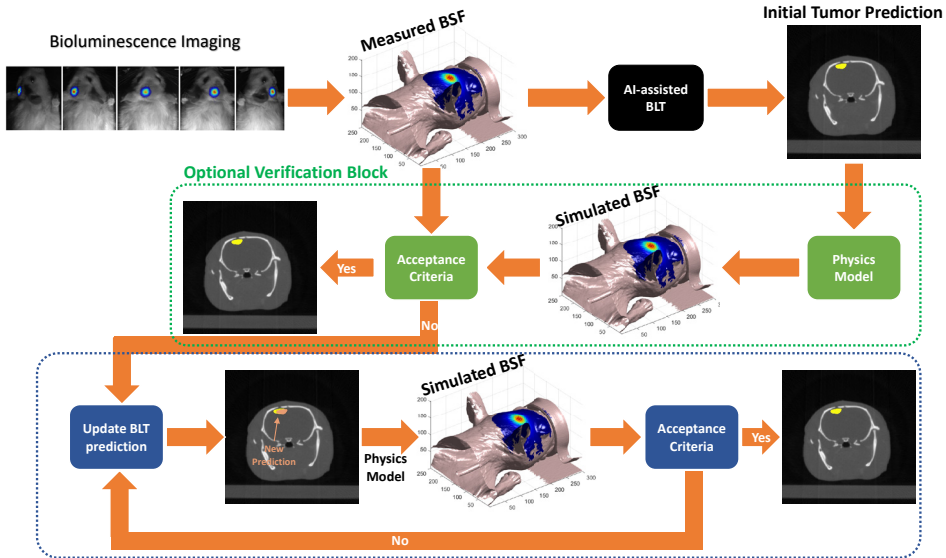


Figure 8.4 – Predicted tumor contour from different models for three different tumors smaller than 10 mm^3 . The red contour is the ground-truth CT-based tumor, and the remaining colors are the prediction from each proposed AI solution



Optional Optimization Block
 Figure 8.5 – Online verification and optimization algorithm for the BLI-based tumor targeting

verification, allowing to know when the AI model is not certain about the corresponding predicted tumor volume. The presented models in this thesis can be tuned to provide prediction verification abilities in different ways. The first approach, presented in Figure 8.5, is to include a physics model of light propagation, such as MCS or a mathematical model, as a control loop to not only verify the predicted tumor volume but also optimize it to provide the least error between measured and simulated BSF. Another approach is to include an uncertainty quantification metric, such as test-time dropout, in the AI model providing the prediction uncertainty for each case during the inference stage. Therefore, this metric can be presented to the user as a quality assurance tool in order to avoid cases with high levels of uncertainty in AI-based predictions. Finally, an ensemble of the different AI models presented in this thesis can also be utilized to alleviate the prediction verification problem. In theory, if various models result in hugely different tumor predictions, one can only conclude that one or more of the predictions are inaccurate. Therefore, a simple DSC metric between the predicted tumors from all the models can be used to distinguish errors in the predictions.

Part 3: Optical Phantoms

Most BLI systems capture the light photons reaching the detector in a qualitative manner. Consequently, the absolute number of photons cannot be derived accurately from these measurements. The system calibration provides the missing link between the qualitative and quantitative BLI. Optical phantoms are an essential tool not only for the BLI system calibration but also for sparing as many animal subjects as possible.

However, currently, there are only a few commercially available optical phantoms in the market, as discussed in the previous chapter. Most of these phantoms consist of accurately measured optical properties in a very simplified (cylindrical or cubical) geometry without any light source. Therefore, there is a need for reproducible and accurate optical phantoms that mimic the complex geometry of the imaging subjects and the light emission from a bioluminescence source.

An ideal bioluminescence phantom (BLP) not only presents optical properties similar to the biological tissue but also mimics the luciferase-enabled emission from the tumor. Therefore, in this thesis, various methods to manufacture such a BLP are investigated. The first approach involved adding scattering micro-spheres inside a fully transparent silicone and obtaining various mixtures with accurately estimated scattering properties. This method provides an ideal solution for the researchers without access to an integrating sphere measurement setup to measure the optical properties. However, due to the high viscosity of the silicone used in this study and the reduced surface-to-air contact inside the mold, the air bubbles created a real challenge. Consequently, despite utilizing a vacuum chamber to apply negative pressure on the bubbles, the majority of the bubbles remained in the phantom, especially in the contact surface between the two separately molded parts. In future studies, the air bubble challenge should be addressed using a combination of a much more powerful vacuum chamber and a modified version of the mold with increased surface-to-air contact. The second challenge regarding the silicone-based phantom was due to the long curing time of the silicone, ranging between 24 to 48 hours at room temperature. Such a long curing time, although a positive feature for releasing air bubbles, acts negatively for the added scattering particles, especially the heavier TiO_2 particles. Consequently, such heavy particles settle at the bottom of the mold over time and create a heterogeneous medium with respect to the optical properties. Alternatively, placing the mixture inside the oven at an increased temperature alleviates this issue but causes further problems with more air bubbles trapped in the surface of the phantom.

The 3D-printed phantoms are a better candidate for optical phantoms that can address all the aforementioned challenges in silicone-based phantoms. However, at the time of this study, the quality of the print and the obtained optical properties greatly depend on the printer setup and parameters such as exposure time and type of resin used. The printer used in this study was capable of printing only a mixture of resin and ink, while printing the mixture of resin and microspheres did not yield satisfactory results partly due to the lower viscosity of the resin compared to the silicone, which allowed the particles to settle down at the bottom of the resin tank. Furthermore, upon further investigation, especially after printing with fully transparent resin without any additives, it has been clear that the surface of the printed object is not as smooth as

desired. This will consequently create further uncertainties and errors in optical property measurements as it will cause random photon deflection by the surface.

Part 4: Future Perspectives

This thesis provides a collection of AI-based solutions for the 3D BLT reconstruction problem to enhance the accuracy of BLI-based tumor targeting and treatment planning in pre-clinical cancer research. To our knowledge, this thesis and publications constitute one of the first AI-based solutions in this field. Consequent to the AI success in other fields, more and more AI-based solutions are finding their way into BLT reconstruction problem. Running at the same time as our study, Gao et al. provided the first AI-based solution, published as a letter, based on a simple multi-layered perceptron (MLP) network using a standard BSF mesh^[6], which is obtained by registering any arbitrary mesh to the standard mesh. Yue et al take this idea further by replacing the MLP network with a slightly more advanced one-dimension convolutional neural network (CNN), which can provide a more efficient learning^[7]. Zheng et al. improved the idea even further by including a self-training strategy on an analytical model of light propagation, still using a mesh-based neural network trained on the standard mesh^[8]. The proposed method by Zheng still requires registration between the arbitrary mesh of the experimental sample to the standard mesh used for the training. However, it constitutes a leap forward compared to the existing AI-based solutions by introducing the first truly physics-informed AI model for this subject. In other words, this solution is the first model that employs the physics models of light propagation inside the internal cost function of the AI, competing with the observation-driven cost function.

The solutions in this thesis advance from one-dimensional or MLP networks to a much more efficient 3D CNN-based deep learning approach, which allows for keeping the spatial relationship between voxels in the image. Therefore, all the proposed methods in this thesis perform the reconstruction task without requiring an additional image registration step to register the input BSF to standard input. However, the 3D CNN networks come at the cost of more trainable parameters, which can cause overfitting issues. Consequently, several measures, such as employing a validation set, automatically optimized hyper-parameters and on-fly data augmentation, are included in the network architecture to avoid such issues. This helped the proposed solution to perform well on the test data and achieve good reconstruction performance, therefore enabling BLI-based tumor targeting. However, the physics-informed AI has the potential to increase the performance of the proposed solutions even further. In other words, employing physics knowledge inside the internal cost function of the deep learning solutions might help the model to learn the solution to the reconstruction problem better and faster using a smaller data size with more generalization ability. Therefore,

such methods can address one of the main drawbacks of the proposed solutions in this thesis: the performance dependency on a high-quality training database. In other words, the physics-informed deep learning solution can be considered a hybrid model/data-based solution that can lean toward either aspect when the other is limited, i.e. the model mostly uses physics laws when data availability is limited and vice versa. Another candidate to improve the accuracy of the BLI-based treatment planning for a wide variety of tumor models is dual-energy BLI. With the development of more advanced luciferase-emitting cell lines that can emit light with two spectral peaks^[9], an extension of the multispectral model proposed in Chapter 5 that is analogous to the idea of dual-energy X-ray CT scans can be achieved. Consequently, such light-emitting cell lines can exploit the differences in tissues' optical properties, i.e. scattering and absorption coefficient, in a wider spectral range that can help identify the tumor location.

References

- [1] J. R. de Wet, K. V. Wood, D. R. Helinski, and M. DeLuca, "Cloning of firefly luciferase cDNA and the expression of active luciferase in *Escherichia coli*," *Proc. Natl. Acad. Sci. U. S. A.*, vol. 82, no. 23, pp. 7870–7873, Dec. 1985, doi: 10.1073/pnas.82.23.7870.
- [2] R. T. Sadikot and T. S. Blackwell, "Bioluminescence Imaging," *Proc. Am. Thorac. Soc.*, vol. 2, no. 6, pp. 537–540, Dec. 2005, doi: 10.1513/pats.200507-067DS.
- [3] A. M. Mowday et al., "Use of a Luciferase-Expressing Orthotopic Rat Brain Tumor Model to Optimize a Targeted Irradiation Strategy for Efficacy Testing with Temozolomide," *Cancers*, vol. 12, no. 6, Art. no. 6, Jun. 2020, doi: 10.3390/cancers12061585.
- [4] S. Yahyanejad et al., "Complementary use of bioluminescence imaging and contrast-enhanced micro-computed tomography in an orthotopic brain tumor model," *Mol. Imaging*, vol. 13, 2014, doi: 10.2310/7290.2014.00038.
- [5] B. Rezaeifar et al., "A deep learning and Monte Carlo based framework for bioluminescence imaging center of mass-guided glioblastoma targeting," *Phys. Med. Ampmathsemicolon Biol.*, vol. 67, no. 14, p. 144003, Jul. 2022, doi: 10.1088/1361-6560/ac79f8.
- [6] Y. Gao, K. Wang, Y. An, S. Jiang, H. Meng, and J. Tian, "Nonmodel-based bioluminescence tomography using a machine-learning reconstruction strategy," *Optica*, vol. 5, no. 11, pp. 1451–1454, Nov. 2018, doi: 10.1364/OPTICA.5.001451.
- [7] J. Yu, C. Dai, X. He, H. Guo, S. Sun, and Y. Liu, "Bioluminescence Tomography Based on One-Dimensional Convolutional Neural Networks," *Front. Oncol.*, vol. 11, 2021, Accessed: Jan. 14, 2022. [Online]. Available: <https://www.frontiersin.org/article/10.3389/fonc.2021.760689>
- [8] X. Zhang et al., "Self-Training Strategy Based on Finite Element Method for Adaptive Bioluminescence Tomography Reconstruction," *IEEE Trans. Med. Imaging*, vol. 41, no. 10, pp. 2629–2643, Oct. 2022, doi: 10.1109/TMI.2022.3167809.
- [9] C. L. Stowe et al., "Near-infrared dual bioluminescence imaging in mouse models of cancer using infraluciferin," *eLife*, vol. 8, p. e45801, Oct. 2019, doi: 10.7554/eLife.45801.

Appendices

Summary

According to the World Health Organization (WHO), nearly one in every six deaths worldwide is due to cancer, making it the number one death cause worldwide. Treating cancer is different for each person, and it depends on the type of cancer and how advanced it is. But for almost half of all cancer patients, a treatment called radiation therapy or radiotherapy is used at least once. This treatment option uses strong ionizing radiation to target tumor cells. Ionizing radiation will damage the targeted body tissue, and with strong enough radiation, i.e. high radiation dose, it can even kill the cells inside the tissue. Therefore, the main goal of every radiation therapy is to target and destroy the tumor cells with high-dose ionizing radiation with minimum effect on the rest of the healthy cells and tissue.

In recent years, technological advances have enabled clinicians to use various techniques to target tumors with radiation more effectively and make radiotherapy an efficient treatment for most tumor types. However, some tumors are more resistant to ionizing radiation or reappear after a short period. Glioblastoma, the most common and aggressive brain tumor, is one of such tumors that do not respond well to the standard treatment, which includes a combination of radiation therapy and chemotherapy. Biologists have identified theoretically various reasons for this, but these hypotheses must be tested completely before translating into a clinical treatment option. Therefore, there is a need for a testing environment, namely preclinical research, that allows for fundamental research investigation and identifying new treatment options to ensure the safety of patients.

Preclinical cancer research tries to improve the quality of the standard treatment options, with otherwise low survival rates, such as glioblastoma, by investigating novel ideas and hypotheses. In this field of research, new ideas are first tested in the lab environments on tumor cells growing in plates, and the treatment efficacy is monitored under the microscope. The next step is to ensure that the tumor cells behave similarly in the vicinity of other body tissues to ensure the same result in the human case. Therefore, the tumor cells are implanted inside small animals such as mice and rats and investigated even further. Since the clinical imaging and radiation therapy systems are too big for such small objects, a new field of research emerged, which resulted in commercially available imaging and radiotherapy systems dedicated to small animals.

Small animal radiotherapy is a field of research that is very analogous to the routine clinical workflow. In other words, the animals are first imaged using a computed tomography (CT) system to identify the location of the tumor and then irradiated using X-ray radiation to destroy them. However, the dimensions of the animals and tumors in small animal radiotherapy are much smaller than the dimensions in humans, hence requiring a much higher precision and resolution. This increased

resolution often causes the CT imaging in the small animal to deliver a higher X-ray radiation dose during the imaging process, namely the imaging radiation dose. Additionally, when it is considered together with the lower tolerance of small animals to ionizing radiation, it underlines the necessity of a novel imaging technology that can identify the location and shape of the tumors without radiation burden on the animals.

Bioluminescence Imaging (BLI) is an imaging technique that uses the same biological process from a firefly to locate the tumor. In other words, the tumor cells are modified in the lab to emit visible light, similar to a firefly. In practice, these modified tumor cells are activated when a substrate is present in their vicinity and will emit light. Once the modified tumor cells are placed inside the animals, after the injection with the corresponding substrate, only the modified tumor cells will light up. Thereafter, the emitted light will travel through the surrounding tissue and leave the animal's body. By this time, the emitted light will be not only diffused but also reduced in intensity due to the surrounding tissue. However, a very sensitive camera can still see this light in a very dark cabinet and create the BLI images, which corresponds well with how big the tumor is. This imaging technology can provide helpful information about the effect of each treatment option, especially radiation therapy, on the tumor cells by looking at the changes in the emitted light over the course of the treatment. However, this technique is not applicable for human subjects since it includes tumor cell modification and injection of a substrate borrowed from firefly.

BLI is used in preclinical cancer research daily to monitor tumors' response to various treatments and determine which treatments are more effective for different tumor types. However, the BLI ability is limited to tumor growth monitoring, and it cannot be used for targeting the tumor cells with X-ray radiation. Therefore, a high-dose CT scan is still needed to obtain the placement of the tumor and obtain a radiotherapy treatment plan, which finds the best arrangement of X-ray radiation beams that deliver the highest radiation dose to the tumor cells and the lowest possible radiation dose to the healthy tissue. In other words, the studies that want to investigate the role of X-ray radiation in cancer treatment cannot employ BLI as their imaging technique and must use a high-dose CT scan with previously mentioned limitations.

This thesis aims to obtain the tumor placement in three dimensions (3D) using the information provided by the BLI and, therefore, enabling the use of the BLI for preclinical cancer research in small animal radiotherapy, specifically for glioblastoma. Here, to obtain the required 3D information from the 2D BLI images, a series of novel Artificial Intelligence (AI) approaches are developed that can accurately predict the tumor's location inside the animal. The developed techniques in this thesis can locate the tumor within a millimeter of its actual location. Furthermore, the Dice similarity coefficient is routinely used to objectively measure the quality of tumor segmentation in medical imaging, which scores the overlap

Appendices

between the actual and the predicted tumor. The developed methods in this thesis can achieve an average Dice score ranging from 62 to 83% depending on the available information and the type of the employed AI model. Therefore allowing the biologists to target the investigated tumor cells using BLI.

SamenVatting

Volgens de Wereldgezondheidsorganisatie (WHO) is bijna één op de zes sterfgevallen wereldwijd te wijten aan kanker, waardoor het de belangrijkste oorzaak van overlijden is. De behandeling van kanker is voor elke persoon anders en hangt af van het type kanker en hoe ver gevorderd het is. Voor bijna de helft van alle kankerpatiënten wordt minstens één keer als behandeling radiotherapie gebruikt. Deze behandeling maakt gebruik van sterke ioniserende straling om tumorcellen aan te vallen. Ioniserende straling zal het beoogde lichaamsweefsel beschadigen, en met voldoende sterke straling, dat wil zeggen een hoge stralingsdosis, kan het zelfs de cellen binnen het weefsel doden. Daarom is het hoofddoel van elke bestralingstherapie om de tumorcellen te vernietigen met een hoge dosis ioniserende straling, maar met zo min mogelijk effect op de rest van de gezonde cellen en weefsels.

In de afgelopen jaren hebben technologische vooruitgangen klinici in staat gesteld om verschillende technieken te gebruiken om tumoren effectiever met straling te behandelen en radiotherapie een efficiënte behandeling te maken voor de meeste soorten tumoren. Sommige tumoren zijn echter meer resistent tegen ioniserende straling of komen na een korte periode terug. Glioblastoma, de meest voorkomende en agressieve hersentumor, is zo'n tumor die niet goed reageert op de standaardbehandeling, die een combinatie van bestralingstherapie en chemotherapie omvat. Biologen hebben theoretisch verschillende redenen voor dit gedrag geïdentificeerd, maar deze hypothesen moeten volledig worden getest voordat ze kunnen worden vertaald naar een klinische behandeloptie. Daarom is er behoefte aan een testomgeving, namelijk preklinisch onderzoek, dat fundamenteel onderzoek mogelijk maakt en nieuwe behandelopties identificeert om de veiligheid van patiënten te waarborgen.

Preklinisch kankeronderzoek probeert de kwaliteit van de standaard behandelopties, met soms lage overlevingspercentages, zoals bij glioblastoma, te verbeteren door nieuwe ideeën en hypothesen te onderzoeken. In dit onderzoeksveld worden nieuwe ideeën eerst getest in laboratoriumomgevingen op tumorcellen die groeien in petrischalen, en de behandelingseffectiviteit wordt gevolgd onder de microscoop. De volgende stap is ervoor zorgen dat de tumorcellen zich op vergelijkbare wijze gedragen in de nabijheid van andere lichaamsweefsels om hetzelfde resultaat in het menselijk geval te waarborgen. Daarom worden de tumorcellen geïmplanteerd in kleine dieren, zoals muizen en ratten, en verder onderzocht.

Aangezien de klinische beeldvormings- en bestralingssystemen te groot zijn voor dergelijke kleine objecten, ontstond er een nieuw onderzoeksgebied, wat resulteerde in commercieel verkrijgbare beeldvormings- en bestralingssystemen die zijn toegewijd aan kleine dieren. Bestralingstherapie bij kleine dieren is een onderzoeksgebied

dat zeer analoog is aan de normale klinische workflow. Met andere woorden, de dieren worden eerst afgebeeld met behulp van een computertomografiesysteem (CT) om de locatie van de tumor te identificeren en vervolgens bestraald met röntgenstraling om de tumorcellen te vernietigen. De afmetingen en tumoren bij bestralingstherapie bij kleine dieren zijn echter veel kleiner dan die bij mensen, waardoor een veel hogere precisie en resolutie nodig is. Deze verhoogde resolutie zorgt er vaak voor dat de CT-beeldvorming bij kleine dieren een hogere dosis röntgenstraling aflevert tijdens het beeldvormingsproces, namelijk de beeldvormingsstralingdosis. Bovendien, wanneer dit samen wordt beschouwd met de lagere tolerantie van kleine dieren voor ioniserende straling, benadrukt dit de noodzaak van een nieuwe beeldvormingstechnologie die de locatie en vorm van tumoren kan identificeren zonder stralingsbelasting voor de dieren.

Bioluminescentiebeeldvorming, Bioluminescence Imaging in het Engels (BLI), is een beeldvormingstechniek die hetzelfde biologische proces gebruikt als een vuurvliegje om de tumor te lokaliseren. Met andere woorden, de tumorcellen worden in het laboratorium aangepast om zichtbaar licht uit te zenden, vergelijkbaar met een vuurvliegje. In de praktijk worden deze gemodificeerde tumorcellen geactiveerd wanneer een substraat aanwezig is in hun omgeving en zullen ze licht uitstralen. Zodra de gemodificeerde tumorcellen in de dieren zijn geplaatst, na injectie met het overeenkomstige substraat, zullen alleen de gemodificeerde tumorcellen oplichten. Vervolgens zal het uitgezonden licht door het omringende weefsel bewegen en het lichaam van het dier verlaten. Tegen die tijd zal het uitgezonden licht niet alleen worden verspreid, maar ook in intensiteit verminderd zijn door het omringende weefsel. Desondanks kan een zeer gevoelige camera dit licht nog steeds zien in een zeer donkere kast en de BLI-beelden creëren, die goed overeenkomen met de grootte van de tumor.

Deze beeldvormingstechnologie kan nuttige informatie verschaffen over het effect van elke behandelingsoptie, met name bestralingstherapie, op de tumorcellen, door naar de veranderingen in het uitgezonden licht gedurende de behandeling te kijken. Deze techniek is echter niet toepasbaar voor menselijke proefpersonen omdat deze tumorcelmodificatie en injectie een substraat geleend van een vuurvliegje omvat. BLI wordt dagelijks gebruikt in preklinisch kankeronderzoek om de respons van tumoren op verschillende behandelingen te monitoren en te bepalen welke behandelingen effectiever zijn voor verschillende tumortypen. De mogelijkheid van BLI is echter beperkt tot het monitoren van tumorgroei en kan niet worden gebruikt voor het richten van röntgenstraling op de tumor. Daarom is nog steeds een CT-scan met hoge dosis nodig om de locatie van de tumor te verkrijgen en een bestralingstherapieplan te maken, dat de beste rangschikking van röntgenstralenbundels vindt die de hoogste stralingsdosis aan de tumorcellen en de laagst mogelijke stralingsdosis aan het gezonde weefsel levert. Met andere

woorden, studies die de rol van röntgenstraling bij kankerbehandeling willen onderzoeken, kunnen geen gebruik maken van BLI als hun beeldvormingstechniek en moeten een CT-scan met hoge dosis gebruiken met eerder genoemde beperkingen. Dit proefschrift heeft als doel de locatie van de tumor in drie dimensies (3D) te verkrijgen met behulp van de informatie die wordt geleverd door de BLI en maakt zo het gebruik van de BLI mogelijk voor preklinisch kankeronderzoek bij bestralingstherapie bij kleine dieren, specifiek voor glioblastoma. Om de vereiste 3D informatie te verkrijgen uit de 2D BLI-beelden, zijn een reeks nieuwe kunstmatige intelligentie, Artificial Intelligence in het Engels (AI), methoden ontwikkeld die de locatie van de tumor in het dier nauwkeurig kunnen voorspellen. De ontwikkelde technieken in deze scriptie kunnen de tumor binnen een millimeter van zijn werkelijke locatie lokaliseren. De Dice-similariteitscoëfficiënt wordt routinematig gebruikt om de kwaliteit van tumorsegmentatie in medische beeldvorming objectief te meten, wat de overlap tussen de werkelijke en voorspelde tumor beoordeelt. De ontwikkelde methoden in deze scriptie kunnen een gemiddelde Dice-score behalen variërend van 62 tot 83%, afhankelijk van de beschikbare informatie en het type gebruikte AI-model. Hierdoor kunnen biologen de onderzochte tumorcellen met behulp van BLI targeten.

A Reflection on Scientific and Social Impacts

Bioluminescence Imaging (BLI) is a technique that's often used in research to examine tumors in small animals. However, the extent of BLI application is limited to tumor growth monitoring, which is an important aspect but does not fully employ the potential of the imaging technology. During the course of this thesis, various advanced computer science methods, known as Artificial Intelligence (AI) models, are developed to enhance the accuracy of the 3D Bioluminescence Tomography (BLT) reconstructed from a set of 2D BLI images. The conducted research in this thesis paves the way for more advanced BLI-based tumor targeting in small animal irradiation platforms, which in turn reduces the ionizing radiation burden on the animals. Therefore, the developed methods within this thesis can be directly employed in the commercially available small animal irradiators, such as the SMART+ (Precision X-ray Inc., Madison, CT, USA) and the SARRP (Xstrahl Life Sciences, Suwanee, GA, USA), to improve the quality of otherwise limited BLI-based tumor targeting with the X-ray radiation beam. Furthermore, the standalone Bioluminescence imaging systems, such as IVIS (PerkinElmer, Shelton, CT, USA) and MILabs' stand-alone optical imaging (MILabs, Houten, Netherlands), can also adapt the developed AI-based methods to enhance the provided BLI-based volumetric tumor monitoring. In addition, the reduced imaging X-ray radiation dose on the animals provided by BLT allows for more imaging checkpoints during a longitudinal study, which is otherwise impossible due to the excessive accumulated X-ray imaging dose. Therefore, the overall quality of the conducted research will increase due to better overall monitoring. Furthermore, the BLI also enables monitoring of substructures within the tumor, such as the hypoxic region, which is deprived of oxygen and directly linked to the poor prognosis.

The findings of this thesis help biologists to employ the full potential of the BLI in their research, especially in order to improve the treatment quality for glioblastoma patients. The developed algorithms in this thesis also allow for more accurate tumor volume monitoring during the course of the treatment in small animals and, therefore, help biologists validate their hypothesis and identify a more efficient treatment option for glioblastoma. Therefore, the outcome of this thesis indirectly contributes to a better treatment option for glioblastoma patients, with currently poor average survival time of only 12 months after the initial diagnosis. However, since the BLI is a dedicated imaging technology for small animal preclinical cancer research and is not applicable for imaging a human subject, the developed methods cannot directly be translated to clinical trials. Nevertheless, the shared fundamentals between BLI and various other types of optical imaging, such as fluorescence imaging, optical coherence tomography, and Cerenkov imaging, allow for fast adaptation of the proposed algorithms in other domains. In more

detail, other researchers can build upon the outcome of this thesis, communicated through scientific journals and conferences, to solve similar 3D reconstruction problems in other optical imaging modalities, some of which with clinical applications.

Even though this thesis focuses on glioblastoma, the developed methods in this thesis can easily be adapted for many other tumor types. In other words, the observation-based AI methods developed in this thesis can be re-trained using a new set of observations for totally different tumor types, such as lung cancer. Therefore, the presented AI-based reconstruction algorithms developed in this thesis can be employed in a variety of different pre-clinical cancer research in order to improve the quality of the conducted pre-clinical investigations, which consequently can play a small role in enhancing the treatment outcome for human patients.

Curriculum Vitae

Behzad Rezaeifar was born on August 2, 1992 in Mashhad, Iran. After finalizing highschool studies at Hashtgerdi highschool in his hometown, he enrolled at Sadjad University of Technology specializing in electrical engineering with a focus on communication engineering, successfully attaining a Bachelor's degree.

During his undergraduate studies, an enduring fascination with medical image processing emerged, sparked by an optional course on Artificial Intelligence. This pivotal discovery led him to pursue advanced studies in Biomedical Engineering at Ferdowsi University of Iran, where a Master's degree was attained with distinction.

For the doctoral phase of his academic journey, in 2018, he embarked on a distinctive double PhD program spanning Belgium and the Netherlands. In the Netherlands, he was based at Maastric Clinic within the Physics Research group, under the mentorship of Prof. Dr. Frank Verhaegen. This interdisciplinary endeavor involved close collaboration with biologists at Maastricht University, with Prof. Dr. L.J. Dubois overseeing this aspect of the research. Simultaneously, in Belgium, he gained admission to Hasselt University within the Nuclear Technology group, closely supervised by Prof. Dr. Brigitte Reniers.

Throughout the course of the double PhD program, he dedicated his efforts to enhancing the applications of Bioluminescence Imaging (BLI) in routine preclinical research, with the primary focus was on advancing treatment efficacy for glioblastoma, a formidable challenge in biomedical research. This multifaceted investigation, conducted in collaboration with esteemed mentors and experts across borders, reflects his commitment to pushing the boundaries of knowledge and contributing to the improvement of medical interventions for critical conditions. He will now continue his work as a postdoctoral researcher at Maastric.

List of publications

Peer-reviewed articles

B. Rezaeifar, C.J.A. Wolfs, N.G. Lieuwes, R. Biemans, B. Reniers, L.J. Dubois, F. Verhaegen, 2023. A deep-learning assisted bioluminescence tomography method to enable radiation targeting in rat glioblastoma. *Phys. Med. Biol.* <https://doi.org/10.1088/1361-6560/ace308>

G.P. Fonseca, **B. Rezaeifar**, N. Lackner, B. Haanen, B. Reniers, F. Verhaegen, 2023. Dual-energy CT evaluation of 3D printed materials for radiotherapy applications. *Phys Med Biol* 68. <https://doi.org/10.1088/1361-6560/acaf4a>

B. Rezaeifar, C.J.A. Wolfs, N.G. Lieuwes, R. Biemans, B. Reniers, L.J. Dubois, F. Verhaegen, 2022. A deep learning and Monte Carlo based framework for bioluminescence imaging center of mass-guided glioblastoma targeting. *Phys. Med. Biol.* 67, 144003. <https://doi.org/10.1088/1361-6560/ac79f8>

A.M. Mowday, N.G. Lieuwes, R. Biemans, D., Marcus, **B. Rezaeifar**, B. Reniers, F. Verhaegen, J. Theys, L.J. Dubois, 2020. Use of a Luciferase-Expressing Orthotopic Rat Brain Tumor Model to Optimize a Targeted Irradiation Strategy for Efficacy Testing with Temozolomide. *Cancers* 12, 1585. <https://doi.org/10.3390/cancers12061585>

Other scientific publications

B. Rezaeifar, M. Saadatmand-Tarzjan, 2017. A new algorithm for multimodal medical image fusion based on the surfacelet transform, in: 2017 7th International Conference on Computer and Knowledge Engineering (ICCKE). Presented at the 2017 7th International Conference on Computer and Knowledge Engineering (ICCKE), pp. 396–400. <https://doi.org/10.1109/ICCKE.2017.8167911>

Conference abstracts, posters and presentations

B. Rezaeifar, C.J.A. Wolfs, N.G. Lieuwes, R. Biemans, B. Reniers, L.J. Dubois, F. Verhaegen. A Deep Learning and Monte Carlo Based Framework for Bioluminescence Imaging Center of Mass-Guided Glioblastoma Targeting. Presented at the Belgian Nuclear Society; Mol, Belgium. December 2022. Awarded the BNS-YG award in Nuclear Medicine and Biology.

B. Rezaeifar, C.J.A. Wolfs, N.G. Lieuwes, R. Biemans, B. Reniers, L.J. Dubois, F. Verhaegen. Harnessing artificial intelligence to improve bioluminescence tomography. Presented at the 5th conference on small animal image-guided radiotherapy; Munich, Germany; March 2022

Appendices

B. Rezaeifar, C.J.A. Wolfs, N.G. Liewes, R. Biemans, B. Reniers, L.J. Dubois, F. Verhaegen. Bioluminescence Source Localization Using Deep Learning to help the outcome of Glioblastoma. Poster presentation at GROW Science Day; Maastricht, The Netherlands; November 2020.

B. Rezaeifar, L. Claesen, L.J. Dubois, B. Reniers, F. Verhaegen, 2019. Novel Preclinical Bioluminescence Imaging as a Tool to Improve the Outcome of Glioblastoma. Poster presentation at GROW Science Day; Maastricht, The Netherlands; November 2019.

B. Rezaeifar, L.J. Dubois, B. Reniers, F. Verhaegen, 2019. Novel Preclinical Bioluminescence Imaging as a Tool to Improve the Outcome of Glioblastoma. Poster presentation at CMK Symposium; Maasmechelen, Belgium; February 2019.

Acknowledgments

I think to my PhD journey as an exceptional and eyeopening experience which was not possible without the help, support, guidance, and collaboration from numerous individuals. Therefore, I would like to thank each and every one of them who made it possible:

Frank, I remember my first days of my PhD when I heard others emphasizing how challenging my PhD will be considering its topic. I can clearly recall feeling stressed and unsure about the future. You helped me navigate through such a challenging PhD journey like a patient father teaching his son how to ride a bike. Like many other PhD students, I experienced my fair share of dead-ends in my PhD. But each time, you helped me navigate my way around it and motivated me when I needed it. I want to thank you for being such a great leader and the most wonderful mentor someone can ask for. I am sure that my PhD wouldn't reached its final chapter without you.

Brigitte, you were my first contact in this PhD. I always could come to you with a question. You always patiently listened and provided great feedbacks and solutions. I appreciate your support and guidance in my PhD journey. I won't forget that you supported me in my most difficult times and reminded me that I can do it.

Ludwig, without you I would have been lost in the complicated world of biology. You guided me through out the project with excellent feedbacks and keen observations that sometimes made me wonder how is it possible. I still remember the day you noticed one of the CT scans in my figure flipped by mistake, which was just a small image in an entire workflow. I learned a lot from our meetings and I hope we can continue collaborating in the future.

Gabriel, I still don't know how you have time to help everyone in their projects. You are truly the pillar of our group at Maastrro and I appreciate you being there to answer my questions.

Cecile, you were not only a great colleague but like a mentor to me. You helped me a lot in my PhD journey with great advise and solutions. Actually, in the moments of uncertainty I always came to you for a second opinion.

Murillo, whenever I wanted to build something, you were there to answer my questions and show me the right way.

Ana, I am happy that you were still at Maastrro when I started my PhD, even though I had to take over your responsibilities on SmART when you finished your PhD. You patiently showed me how things work around the office and helped me get started with my project.

Brent, I used some of your brilliant ideas in the thesis and also in UNO. Teun, thanks for offering me to steal your spot at Maastrro. I enjoyed working there until the very last moment.

My great colleagues and wonderful friends at Maastrro which we shared tons of lunch and coffee break. You made my time at Maastrro wonderful:

Britt, Carolina, David, Didier, Georgios, Hajar, Isable, Joël, Karen, Lars, Laslo, Luca, Mart, Nadine, Nick, Niklas, Raoul, Rosa, Roua, Slava, Stefan, Teun, Tim.

My colleagues at UHasselt who made it easy for me to split my time between the two Universities: Bram, Burak, Dries, Jonathan, Lowie, Mattias, Nathalie, Nazanin, Sonia, Stef, Wouter.

My wonderful friends in Maastricht and Hasselt who made my time here much more pleasant. I appreciate you guys: Ali, Andrea, Angela, Chantalle, Irida, Jonas, Majed, Marco, Nele, Othman, Pouyan, Roberto, Sal, Wesley.

Finally I would like to thank my family who without them and their support none of this would have been possible:

مادر و پدر عزیزم، شیده شیوا و بهناز، شما همواره در تمام طول مدت تحصیلم همراه و پشتیبانم بودید. از اولین قلمی که به دست گرفتم تا مدرک دکتری را مدیون زحمات شما هستم. دور بودن از شما در طول مدت تکمیل پروژه دکتری یکی از سخت ترین چالشهایی بود که با آن مواجه بودم. ولی با این وجود هر زمان که چالش داشتم شما در کنارم بودین تا با انگیزه و اعتماد به نفس پیش برم. باور داشتن شما به من نقطه شروع هر موفقیتی در زندگی من بوده و هست.

ستاره، نوشتن این پاراگراف برای تشکر از تو یکی از سخت ترین قسمت های این کتاب بود. تو یکی از قشنگترین اتفاقهایی بودی که در طول مدت پروژه دکتری برای من پیش آمد. قطعاً بدون تو سختی های راه دکتری چند برابر بود. ممنون از تو که در این راه همراهم بودی و با پشتیبانی ازم در شرایط سخت بهم آرامش لازم برای غلبه بر مشکلات را دادی.